



UNIVERSITY OF LEEDS

Calibration and acceleration of thrombosis modelling in intracranial aneurysms



Qiongyao Liu

University of Leeds

School of Computing

Submitted in accordance with the requirements for the degree of

Doctor of Philosophy

April, 2025

Intellectual Property Statement

The candidate confirms that the work submitted is his own and that appropriate credit has been given where reference has been made to the work of others. I am the main author of all the following publications. I led the design of the study, wrote the codes, implemented the experiments, and drafted the manuscript, including the analysis and discussion of the results. The contribution of other authors was in helping me with designing the study, discussion of the results, and review of the manuscript.

- **Chapter 3:**

Liu Q, et al. “Haemodynamics of Thrombus Formation in Intracranial Aneurysms: An in Silico Observational Study”. *APL Bioengineering*. 2023 Sep 1;7(3) (JCR Q1, IF6.6, Editor’s pick).

- **Chapter 4:**

Liu Q, et al. “Key Influencers in an Aneurysmal Thrombosis Model: A Sensitivity Analysis and Validation Study”. *APL Bioengineering*. 2025 Feb 11;9(1) (JCR Q1, IF6.6, Editor’s pick).

- **Chapter 5:**

Liu Q, et al. “Time Discretisation in the Solution of Advection-Diffusion-Reaction Equations with PINNs”. *Bioengineering & Translational Medicine*. 2025. (under review).

This copy has been supplied on the understanding that it is copyright material and that no quotation from the thesis may be published without proper acknowledgement.

The right of Qiongyao Liu to be identified as Author of this work has been asserted by him in accordance with the Copyright, Designs and Patents Act 1988.

© 2025 The University of Leeds and Qiongyao Liu.

Acknowledgements

I would like to thank my supervisors Professor Alejandro F. Frangi, Dr Ali Sarrami-Foroushani, Dr Toni Lassila, Dr Zeike A. Taylor, Dr Yongxing Wang, and Dr Nishant Ravikumar for providing me with the opportunity to work in a great and ambitious research group and giving me constructive advice and helpful lessons throughout the years.

Thanks to all my colleagues and friends in Leeds, for all the support and good memories. Thanks to Professor Tufail Patankar, Dr Michael MacRaid, Dr Yan Xia, and Dr Shuang Song who collaborated on the APL Bioengineering paper. Thanks to our software engineers Alejandro Daniel Lebrero, Kattia Lisette Hoz de Vila and Christopher Kelly for all the technical support throughout different parts of the project.

I appreciate the School of Computing Full-Time Fees and Maintenance PhD scholarship from University of Leeds.

Thanks to my parents and my sister for all the love and support throughout my life.

Abstract

Approximately 5-8% of the general population harbours an intracranial aneurysm (IA), which is a localised dilation or ballooning of the cerebral blood vessel caused by the weakness of the wall of a cerebral artery or vein. Untreated IAs may eventually rupture and lead to death. Nowadays, the non-invasiveness of endovascular approaches is often used as a first-choice treatment due to its low morbidity and mortality risk. The efficacy of endovascular treatment for IA is influenced by both haemodynamics and thrombosis. Currently, *in vivo* or image-based analysis of thrombosis haemodynamics in realistic anatomies and physiologies is very difficult, if not impossible. Computational modelling has proven to be a powerful tool in predicting thrombosis haemodynamics in IAs before and after endovascular treatment and thus in patient-specific treatment planning or *in silico* trials. However, before being applied in clinical practice, there is a need to demonstrate the credibility of computational thrombosis modelling, defined as trust in the predictive capability of a computational model. According to the American Society of Mechanical Engineers (ASME) V&V 40, the credibility of computational modelling can be assessed using clinical studies, robust model calibration studies, or population-level validation studies. Given the complexity of thrombus formation, involving blood flow and the net results of a series of biochemical reactions, it is important to improve the efficiency of computational thrombosis modelling for using in population-level model credibility assessment studies.

This thesis aims to improve both the credibility and efficiency of patient-specific computational thrombosis modelling. This work contributes to the following aspects: (1) We create a fully automatic multi-scale modelling workflow that enables population-based *in silico* studies to calibrate haemodynamic thresholds of thrombus formation against real population-specific data. (2) We identify the most influential factors of our thrombosis model through a comprehensive global sensitivity analysis and further validate the thrombosis model based on a real patient case using patient-specific parameters for those identified as influential ones and the calibrated trigger thresholds of thrombosis initiation. (3) We investigate the use of a physics-informed deep learning model to accelerate thrombosis modelling

by leveraging the power of neural networks and GPUs.

CONTENTS

1	Introduction: Background, Motivation and Contribution	1
1.1	Intracranial Aneurysms, Endovascular Treatments and Outcome	3
1.1.1	Intracranial Aneurysms	3
1.1.2	Endovascular Treatments	3
1.1.3	Treatment Outcomes	5
1.2	Thrombosis Modelling in IAs	6
1.3	Thesis Contributions and Overview	8
2	Medical Image-Based Patient-Specific CFD Workflow for Thrombus Formation in Intracranial Aneurysms	12
2.1	Vascular Blood Flow Modelling	14
2.1.1	Aneurysm Imaging and Digital Segmentation	14
2.1.2	Blood Flow Modelling	16
2.1.3	Patient-Specific Inlet Flow Waveforms	17
2.2	Virtual Endovascular Treatment	18
2.2.1	Coiling	18
2.2.2	Stenting and Flow Diverter	18
2.3	Aneurysmal Thrombosis Modelling	19
2.3.1	Hemostasis and Thrombosis	19
2.3.2	Literature Thrombosis Models	21
2.3.3	Residence Time	23
2.3.4	The Flow Stasis-Induced Thrombosis Model	25
2.4	Summary of Our CFD Workflow	28
2.5	Improved CFD Workflow (Technical Contributions)	31

2.5.1	Fully Automatic Volume Meshing and Post-Processing	31
2.5.2	Improved Virtual Coiling for Wide-Neck Aneurysms	35
2.5.3	Narrowing the Thrombosis Initiation to Areas Near the Wall . . .	36
3	Haemodynamics of Thrombus Formation in Intracranial Aneurysms: An in Silico Observational Study	38
3.1	Introduction	39
3.2	Materials and Methods	41
3.2.1	Systematic Literature Review	43
3.2.2	In Silico Observational Study	43
3.3	Results	49
3.3.1	Clinical ST prevalence	49
3.3.2	Numerical Results of RT and SR	49
3.3.3	The Effect of Hypertension on the ST Prevalence	56
3.4	Discussion	58
3.4.1	An Example Case Comparison Between Normotension and Hy- pertension	61
3.4.2	Limitations	63
3.4.3	Conclusion	65
4	Key Influencers in an Aneurysmal Thrombosis Model: A Sensitivity Analysis and Validation Study	66
4.1	Introduction	67
4.2	Materials and Methods	70
4.2.1	The thrombosis model parameters	70
4.2.2	0D model and least-squares fitted linear model	74
4.2.3	Elementary effect (EE) method	75
4.2.4	Validation study	76
4.2.5	Narrowing the thrombosis initiation to areas near the wall	78
4.3	Results	80
4.3.1	SA results of the lumped parameter model	80
4.3.2	SA results of the full 3D model using EE method	80
4.3.3	Validation study based on a real patient case with detailed clinical records	83

4.4	Discussion	88
4.4.1	Limitations	92
4.4.2	Conclusion	93
5	Time Discretisation in the Solution of Advection-Diffusion-Reaction Equations with PINNs	94
5.1	Introduction	95
5.2	Materials and Methods	98
5.2.1	Advection-Diffusion-Reaction Equation	98
5.2.2	The Continuous-time PINNs Model	100
5.2.3	The Discrete-time PINNs Model	101
5.2.4	Activation Functions	103
5.2.5	2D Channel Problem	104
5.2.6	2D Idealised Aneurysm Problem	105
5.3	Results	106
5.3.1	PINNs for RT in 2D Channel	106
5.3.2	PINNs for RT in 2D Idealised Aneurysm	109
5.4	Discussion	109
5.4.1	Conclusion	114
6	Conclusions and Outlook	115
6.1	Conclusions	116
6.2	Outlook	116
A	List of Publications	120
A.1	Journal paper	121
A.2	Conference paper	121
A.3	Conference abstract	122
B	Biosketch	123
	References	126

LIST OF FIGURES

1.1	A 16.5 mm saccular aneurysm at the middle cerebral artery (MCA), demonstrated by digital subtraction angiography (DSA).	4
1.2	The Modified Raymond-Roy Classification (MRROC) of angiographic results: Class I: complete occlusion. Class II: residual neck. Class IIIa: residual aneurysm with contrast within coil interstices. Class IIIb: residual aneurysm with contrast along aneurysm wall.	5
1.3	Histology of non-organised red (unstable) and organised white (stable) thrombi [Kulcsár and Szikora, 2012].	7
1.4	A graphical representation of the thesis structure, and the contribution of each chapter.	11
2.1	Medical image-based CFD workflow. (a) Patient’s angiogram and vascular surface model. (b) Virtual treatment: coiling (left) and stenting (right). (c) Volume meshing using ANSYS ICEM CFD v19.3, impose patient-specific inlet flow waveforms, and run simulations in ANSYS CFX v19.3.	13

2.2	Overview of the coagulation cascade. The coagulation cascade is initiated in two different mechanisms: the intrinsic pathway (initiated by factors within the blood) and the extrinsic pathway (triggered by external trauma). Both pathways converge at the production of factor Xa. The common pathway results in the generation of a burst of thrombin, which converts fibrinogen to fibrin and activates platelets. Note: XIa represents the activation of XI. HK, high-molecular-weight kininogen; PK, plasma prekallikrein; TF, tissue factor; TF:VIIa, tissue factor binds factor VIIa; PT, prothrombin; TH, thrombin; FG, fibrinogen; FI, fibrin; RP, resting platelets; AP, activated platelets.	20
2.3	The thrombosis model in our group including four main biochemically-coupled events: Thrombin generation, Fibrin generation, Platelet activation, and Platelet aggregation.	25
2.4	From segmentation, we acquired the patient-specific vascular surface model (a) that can be used to generate unstructured volumetric meshes (b) using ANSYS ICEM CFD v19.3 (Ansys Inc. Canonsburg, PA, USA). During volume meshing, a neck surface was used to separate the computational domain into parent vessel and aneurysm.	32
2.5	The neck surface can sometimes result in poor volume meshing outcomes, leading to incorrect simulation results. (a) If the aneurysm is cut out using a plane and then automatically capped to create a flat neck surface, this surface can sometimes be mistakenly identified as a wall during volume meshing. As a result, no blood flow (zero velocity inside the aneurysm) can be transported to the aneurysm sac. (b) If points along the mesh element edges are manually selected to separate the vessel from the aneurysm, and the neck surface is then semi-automatically generated using ANSYS ICEM, the neck surface is usually treated as an internal wall during volume meshing, allowing blood flow to pass through.	33
2.6	Improved virtual coiling for wide-neck aneurysms. (a) There are apparent gaps between the virtual coils and stent on the left and right side of the stent while the coils already contact with the top of the stent. (b) Improved virtual coiling to reduce gaps between the stent and coils and also avoid intersection.	36

2.7 The aneurysms sac of saccular aneurysms can be approximated with a least square fit (or inscribed) ellipsoid or sphere. 37

3.1 Automatic workflow on MULTI-X. The images were from the @neurIST project [Iavindrasana et al., 2008, Villa-Uriol et al., 2011]. We applied a multi-tasking neural network to automatically segment these images [Lin et al., 2023] and generate the corresponding patient-specific vascular surface models, and then we used ANSYS ICEM CFD v19.3 (Ansys Inc. Canonsburg, PA, USA) to generate unstructured volumetric meshes. The patient-specific inlet flow waveforms were generated from a Multivariate Gaussian Model (MGM) [Sarrami-Foroushani et al., 2016] and a CARS model [Lassila et al., 2020]. Finally, the coupled Navier-Stokes equations and transport equation for RT were solved in ANSYS CFX v19.3 (Ansys Inc., Canonsburg, PA, USA) using a finite volume method [Sarrami-Foroushani et al., 2019]. 42

3.2 Segment the aneurysm sac alone and then extract the RT and SR information inside the aneurysm sac during post-processing. 47

3.3 Patient-specific inlet flow waveforms. 48

3.4 For a given case, thrombus formation in the aneurysm sac is assumed to initiate when the RT exceeds the RT threshold and the SR is below the SR threshold. We systematically explored all possible combinations of RT (ranging from 0 s to 5 s with 0.1 s increments) and SR (ranging from 0 s⁻¹ to 50 s⁻¹ with 1 s⁻¹ increments). Scatter plots were then generated to visualise the RT-SR parameter combinations where the numerical ST prevalence aligned with the clinical ST prevalence (25.5%) observed in large and giant aneurysms, with a 5% tolerance. For three different inflow waveforms (high, mean, and low waveforms), different RT and SR combinations were obtained. The plausible threshold values for thrombus formation are those located within the overlap area, as this region indicates where the thresholds are largely independent of inter-subject flow variability. 53

3.5 Relationships between aneurysm geometry characteristics and RT/SR for the whole simulation cohort. 57

3.6	Comparison between normotension and hypertension for all 42 large and giant IAs in terms of the maximum RT and the minimum SR. In the box and whiskers plot, the horizontal line within the box denotes the median value. The lower and upper edges of the box denote the 25th and 75th percentiles. The ends of the whiskers are drawn to the upper and lower extreme values. p values were computed using the two-tailed t-test. (a) Maximum residence time (RT). (b) Minimum shear rate (SR).	58
3.7	Velocity field and streamline plot of the highest AR case.	62
3.8	Velocity field and streamline plot of the mean AR case.	62
3.9	Velocity field and streamline plot of the lowest AR case.	63
3.10	Comparison of the time-averaged velocity distribution between normotension and hypertension. The mean inlet flow velocity in normotension and hypertension is 13.78 cm/s and 11.29 cm/s, respectively.	64
3.11	Residence Time (RT) and Shear Rate (SR) distribution in normotension and hypertension.	64
4.1	The sensitivity analysis (SA) workflow. There are 31 parameters in our thrombosis model with 12 parameters that can be assessed with a lumped 0D model, 14 that can be investigated with the 3D full model, and 5 others that do not need to be assessed. We first screened 4 influential parameters from the 12 kinetic-associated parameters using the lumped 0D model, then performed SA with the elementary effect (EE) method using the 3D full model for 18 (4 + 14) parameters to identify the most influential model parameter. Finally, we further demonstrated the necessity of SA with a validation case by comparing the simulation results under patient-specific and non-patient-specific settings with the clinical ground truth.	73
4.2	A partially thrombosed clinical case with manual label of the thrombosis region before treatment. (a) The raw image from Leeds General Infirmary. (b) The manually labelled partial thrombosis regions (the green regions), the manually labelled aneurysm sac and parent vessel regions (the red regions).	78

4.3	The 0D model & least-squares fitted linear model results show that 4 kinetic-related parameters: $C_{FI,50}$, K_{FI}^{TH} , K_{TH}^{AP} , and K_{TH}^{AT} have significant effect on the lumped parameter model.	81
4.4	3D vessel & aneurysm geometry used in the sensitivity analysis study. .	81
4.5	Convergence of the sensitivity analysis simulations.	82
4.6	The 3D model & Elementary effect (EE) method results using FiPi as the output metric indicate that the resting platelet concentration is the unique most important parameter that affects the final formed thrombus composition.	82
4.7	The 3D model & Elementary effect (EE) method results using bound platelet concentration as output metric indicate that the resting platelet concentration is the unique most important parameter that affects the final formed thrombus composition.	83
4.8	We manually labeled the partial spontaneous thrombosis region as pre-treatment clinical ground truth. High residence (RT) and low shear rate (SR) are widely used in computational models to characterize the flow stasis that triggers the thrombosis formation process in the aneurysm sac. Using our previously calibrated trigger thresholds[Liu et al., 2023], RT 1.9 s and SR 11 s^{-1} , our flow simulation model successfully predicted the main thrombosis area before treatment.	84
4.9	Comparison between the patient-specific and non-patient-specific simulation results using the clinical record as ground truth. In the clinical ground truth figure, the red part was the manually labelled partial thrombosis region. In the simulation results, the thrombus were assumed to be formed in regions where the fibrin concentration, C_{fi} , is greater than 600 nM.	85
4.10	Virtual deployment of the stent and coils according to the patient-specific treatment information.	87

4.11	Variation of the thrombus volume for the post-treatment simulation. The thrombus grows rapidly at the very beginning (0-5 cycles), and then the growth slows down (5-325 cycles). For this patient-specific case, the thrombus volume at 5 cardiac cycles reaches 86% of the final volume observed at 325 cycles. The thrombus volume at 175 cardiac cycles reaches 95% of the final volume at 325 cycles.	87
4.12	Qualitative comparisons between the immediate post-treatment angiographic result and our simulation result. (a) The clinical immediate post-treatment digital subtraction angiography (DSA) result shows minimal residual flow in the neck of the aneurysm; (b) The post-treatment simulation result also shows residual blood flow in the neck region of the aneurysm; (c) The thrombus formation result predicted by our thrombosis model after virtual patient-specific treatment. The thrombi are assumed to be formed in regions where the fibrin concentration, C_{FI} , is greater than 600 nM. The white patches in the slice shown are caused by the visualisation of the virtual coils.	89
4.13	Resting platelet count distribution obtained from more than 400,000 cases from UK Biobank.	91
5.1	Basic overview of the continuous-time physics-informed neural network (PINNs) used in this chapter, displaying network inputs, output, and the four loss components.	99
5.2	Basic overview of the backward differentiation formulae (BDF) physics-informed neural network (PINNs) used in this chapter, displaying network inputs, output, and the three loss components.	101
5.3	The reference of RT in 2D channel problem solved using the finite difference method (FDM).	105
5.4	The 2D idealised aneurysm.	106
5.5	The continuous-time PINNs model for solving RT in 2D channel performed well with training data (≤ 10 s) but failed to predict the correct solution beyond the training data set (>10 s).	107
5.6	The BDF-1-PINNs model for solving RT in 2D channel showed good long-term stability. It successfully predicted the RT solution at $t = 15$ s while only initialised with the reference data at $t = 5$ s.	108

5.7 The relative errors of the PINNs model for solving RT in 2D channel. The RT reference solution was generated from the finite difference method (FDM). 108

5.8 Comparison between the PINNs results with different activation functions and the ground truth calculated using ANSYS CFX at $t = 8$ s. . . 110

5.9 The relative errors of PINNs by using the CFX results as references in 2 cardiac cycles. The time-step size is 0.01s. 110

5.10 The absolute errors of BDF-1-SIREN by using the CFX results as references in 2 cardiac cycles. 111

6.1 Workflow for investigating the mechanism of delayed rupture. Green labels indicate that they have been completed, yellow labels indicate that they are in progress, and blue labels indicate that they will be completed in the future. My main contributions to this delayed rupture study were as follows: (1) background research and study design; (2) collection of clinical image data and verification of segmentation results; (3) selection of the study cohort and virtual deployment of FD. 119

LIST OF TABLES

3.1	Population Characteristics.	45
3.2	The maximum RT and minimum SR assuming Newtonian and non-Newtonian blood flows.	46
3.3	ST prevalence of large aneurysms (large IAs only).	50
3.4	ST prevalence of giant aneurysms (giant IAs only).	51
3.5	Summary of the literature ST prevalence.	52
3.6	Numerical results of Max RT and Min SR in the aneurysm sac for large and giant IAs.	54
3.7	Comparison between thrombosed and non-thrombosed aneurysms.	55
3.8	Comparison between our CFD calibrated thresholds and the literature thresholds.	60
4.1	5 parameters that no need to be assessed.	70
4.2	12 parameters can be assessed with the 0D model and Sobol' method.	71
4.3	14 parameters can be assessed with the full 3D model and EE method.	72
4.4	Patient-specific flow-diverter model and coils information.	77
4.5	Comparison between patient-specific and non-patient-specific modelling.	85
5.1	Coefficients of the BDF methods.	102

Abbreviations

IA	Intracranial Aneurysm	SAH	Subarachnoid Haemorrhage
FiPi	Flow-Induced Platelet Index	CFD	Computational Fluid Dynamics
SR	Shear Rate	RT	Residence Time
ST	Spontaneous Thrombosis	CTA	CT Angiography
MRA	Magnetic Resonance Angiography	3DRA	3D Rotational Angiography
OSI	Oscillatory Shear Index	MGM	Multivariate Gaussian Mode
TF	Tissue Factor	PINNs	Physics-Informed Neural Networks
ADR	Advection-Diffusion-Reaction	AR	Aspect Ratio
SA	Sensitivity Analysis	MRROC	Modified Raymond-Roy Classification
WSS	Wall Shear Stress	MCA	Middle Cerebral Artery
PComA	Posterior Communicating Artery	ACA	Anterior Cerebral Artery
ICA	Internal Carotid Artery	BA	Basilar Artery
PCA	Posterior Cerebral Artery	SCA	Superior Cerebellar Artery
CARS	Cerebral Autoregulation System	FD-PASS	Flow Diverter Performance Assessment
SBP	Systolic Blood Pressure	DBP	Diastolic Blood Pressure
OAT	One Parameter at a Time	EE	Elementary Effect
OKM	The O’Kelly-Marotta	DSA	Digital Subtraction Angiography
BDF	Backward Differentiation Formulae	PDEs	Partial Differential Equations
DNNs	Deep Neural Networks	FDM	Finite Difference Method

CHAPTER 1

Introduction: Background, Motivation and
Contribution

Any biomedical product intended for commercial sale must undergo a rigorous development and evaluation process to ensure its safety and efficacy before it can be placed on the market [Viceconti et al., 2016]. Currently, the safety and efficacy of a biomedical product are estimated through pre-clinical trials (controlled experiments in vitro or in vivo in animals) and clinical trials (controlled experiments in vivo in humans) [Viceconti et al., 2019]. In vivo experiments are conducted on living tissues, on whole organisms or inside them [Lipatov et al., 2019]. In vitro experiments are conducted on tissues, cells, or other parts of an organism outside of living organisms, typically in test tubes or similar laboratory equipment. However, these traditional trials present several challenges: (1) these trials are usually very expensive and not always successful. Whenever a product fails at a later stage, the company suffers huge losses; (2) clinical trials may tell us that a product is unsafe or ineffective, but they rarely tell us why or suggest how to improve it; (3) both in vivo and in vitro methodologies pose significant economic and ethical challenges, such as limited throughput, high operational costs, and the inhumane treatment of animals during experimental procedures [Lipatov et al., 2019]. To address the inherent limitations of conventional clinical trials, in silico clinical trials were first introduced in approximately 2011 as a computational alternative [Haddad et al., 2017, Pappalardo et al., 2019]. The term “in silico clinical trial” refers to an application of computational modelling and simulation where device performance is evaluated using a “virtual cohort” of simulated patients with realistic anatomical and physiological variability representing the indicated patient population [Viceconti et al., 2021]. Computational modelling and simulation of medical device can streamline development and reduce burdens associated with premarket device evaluation. It can also reveal important information not available from traditional in vivo or in vitro assessments, such as serious and unexpected adverse events that are undetectable within a study sample but occur frequently enough within the intended population to be of concern. However, there is a need to demonstrate the credibility of computational modelling and simulation for any possible clinical use in the future. In the context of evaluation of endovascular medical devices in intracranial aneurysms, both the simulation of aneurysmal haemodynamics and thrombosis after endovascular treatment are computationally expensive now. It is important to improve the efficiency of computational thrombosis haemodynamics modelling for using in population-level model credibility assessment studies. The main aim of this research is to develop an

credible and computationally efficient *in silico* clinical workflow in the context of evaluation of endovascular medical devices in intracranial aneurysms. In this chapter, we will first describe the fundamental knowledge of intracranial aneurysms, endovascular treatments, treatment outcomes, and thrombosis modelling.

1.1 Intracranial Aneurysms, Endovascular Treatments and Outcome

1.1.1 Intracranial Aneurysms

Intracranial aneurysm (IA) is a type of cerebrovascular pathology, which is a localised dilation or ballooning of the cerebral blood vessel caused by the weakness of the wall of a cerebral artery or vein [Withers et al., 2013]. There are four main types of IAs: saccular, fusiform, dissecting, and mycotic [Keedy, 2006]. Among these, saccular aneurysms accounts for 90% of IAs (Fig. 1.1). Therefore, our research primarily focuses on saccular aneurysms. Approximately, 5-8% of the general population harbours an IA [Rinkel et al., 1998]. The prevalence of aneurysms is very low during the first two decades of life but steadily increases after the third decade [Rinkel et al., 1998]. Untreated aneurysms may eventually rupture and then result in aneurysmal subarachnoid haemorrhage (SAH), a subset of stroke that has high case fatality and morbidity rates [Kleinloog et al., 2018]. Aneurysmal SAH accounts for 80% of nontraumatic SAH cases, occurring at a rate about 6 to 10 per 100,000 persons per year. SAH can cause sudden death before the patients receive medical attention. Moreover, 10% to 20% of SAH survivors are functionally dependent, and two-thirds of the functionally independent experience a reduction in quality of life [Hop et al., 1997, Huang and Van Gelder, 2002, van Gijn and Rinkel, 2001]. The goal of treating patients with unruptured IAs is to maximise their duration of high-quality life by optimally balancing the risks of aneurysm rupture with those of treatment-related adverse outcomes [Burns and Brown, 2009].

1.1.2 Endovascular Treatments

There are three main treatment options for patients with IAs: observation, surgical therapy, and endovascular therapy [Keedy, 2006]. The objective of the latter two is to isolate the aneurysm from the circulatory system to prevent haemorrhage. Since

1.1 Intracranial Aneurysms, Endovascular Treatments and Outcome

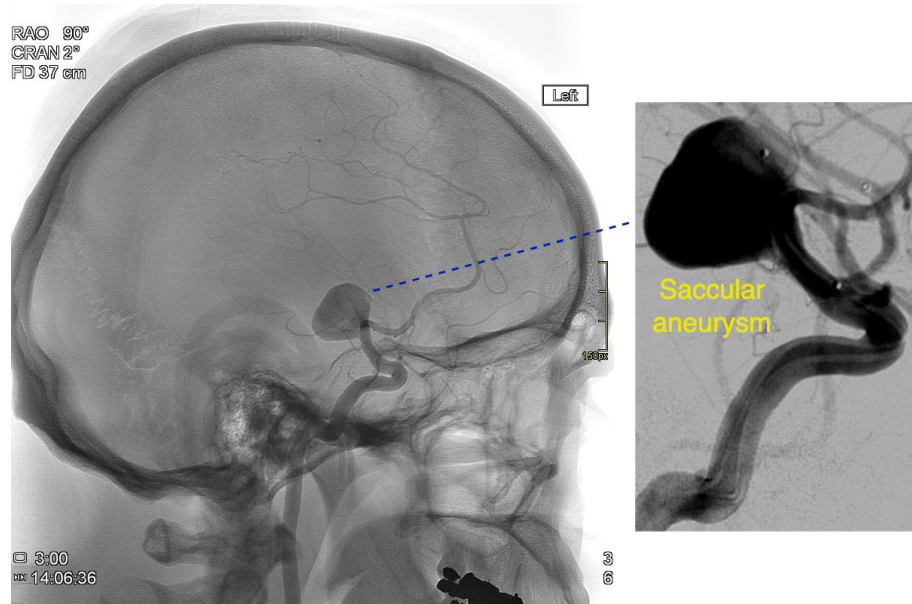


Figure 1.1: A 16.5 mm saccular aneurysm at the middle cerebral artery (MCA), demonstrated by digital subtraction angiography (DSA).

the introduction of endovascular therapy in 1991, its use has substantially increased in treating of aneurysms [Burns and Brown, 2009, Guglielmi et al., 1991]. Endovascular techniques can be categorised into: (1) parent artery reconstruction with coil deposition, which includes primary coiling, balloon-assisted coiling, stent-assisted coiling, and other new techniques such as neck reconstruction devices and intraluminal occlusion devices; (2) reconstruction with flow diversion; and (3) deconstructive techniques, which involve parent artery sacrifice with or without bypass [Diaz and Rangel-Castilla, 2016]. The novelty of endovascular coiling lies in the insertion of a soft, flexible coil via a catheter into the IA cavity, which adapts to aneurysms of varying sizes and shapes to reduce haemodynamic exchange between the aneurysm and the parent vessel [Becske et al., 2013, Sarrami-Foroushani et al., 2017]. The randomised International Subarachnoid Aneurysm Trial (ISAT) study demonstrated the superiority of endovascular treatment of ruptured aneurysms using coil technology over surgical methods [Burns and Brown, 2009, Molyneux et al., 2002, Pierot and Wakhloo, 2013]. However, the limitation of the coiling treatment is evident in wide-neck aneurysms (neck size ≥ 4 mm) due to the difficulty in stabilising the coils inside the aneurysm [Pierot and Biondi, 2016]. This limitation has led to developing other more complex endovascular

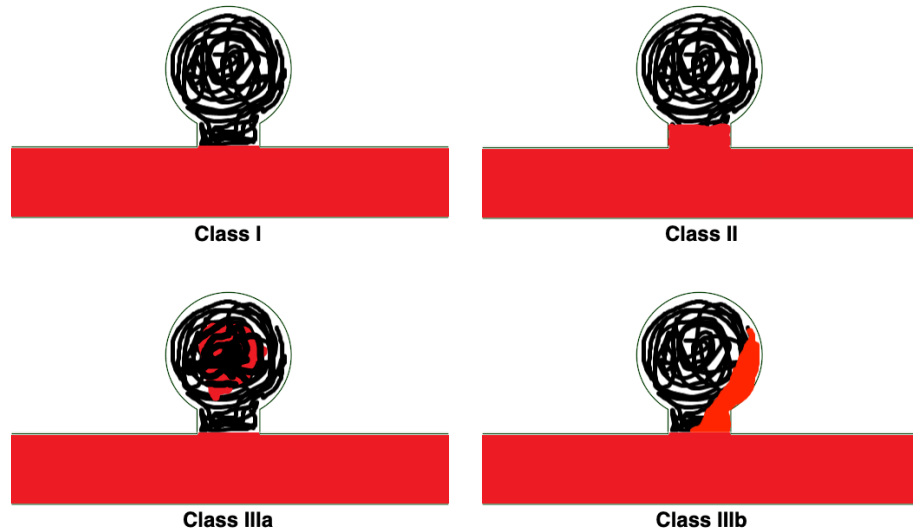


Figure 1.2: The Modified Raymond-Roy Classification (MRROC) of angiographic results: Class I: complete occlusion. Class II: residual neck. Class IIIa: residual aneurysm with contrast within coil interstices. Class IIIb: residual aneurysm with contrast along aneurysm wall.

techniques, such as stent-assisted coiling, balloon-assisted coiling, and flow diversion. Early stents, due to their high porosity, were unable to achieve complete occlusion of the IA through blood flow diversion and had poor safety profiles. Subsequent research led to improvements in the initial stent designs, resulting in flow diversion devices with lower porosity. Currently, wide-neck IAs, which have a larger volume, a higher rupture risk, and are difficult to occlude with coils alone, are typically treated with flow diverter-assisted coil embolisation. The non-invasiveness of endovascular approaches is often used as a first-choice treatment due to its low risk of morbidity and mortality now[Sarrami-Foroushani et al., 2017, Withers et al., 2013].

1.1.3 Treatment Outcomes

After endovascular treatment, angiographic findings are recorded immediately, at six months, and yearly thereafter [Roy et al., 2001]. As illustrated in Fig. 1.2, the modified Raymond-Roy Classification (MRROC) is a widely accepted system for evaluating aneurysm occlusion class [Mascitelli et al., 2015]. In this scheme, Class I is defined as complete occlusion, Class II as residual neck, Class IIIa as residual aneurysm with contrast within coil interstices, and Class IIIb as residual aneurysm with

contract along aneurysm wall. Published aneurysmal complete occlusion rates (refers to the proportion of treated aneurysms in which imaging confirmation demonstrates no residual filling of the aneurysm sac after endovascular treatments) are often variable, ranging anywhere from 55% to 95% [Briganti et al., 2015, Brinjikji et al., 2013, Roy et al., 2001], and the durability of aneurysm coil embolisation was not achieved in all aneurysms [Pierot and Wakhloo, 2013]. According to a systematic review of a large number of studies, aneurysm reopening (refers to the reappearance or reopening of a previously treated aneurysm after an initial intervention) occurred in 20.8%, and retreatment was performed in 10.3% [Ferns et al., 2009, Pierot and Wakhloo, 2013]. In addition, some aneurysms fail to develop a stable clot even with sufficient levels of flow reduction and may end up with post-treatment rupture, leading to high risks of mortality and morbidity [Byrne and Szikora, 2012, Kulcsár and Szikora, 2012, Sarrami-Foroushani et al., 2019]. From autopsy studies of aneurysms, researchers found that there are two different types of thrombi: organised white thrombus, rich in fibrin, and non-organised red thrombus, rich in fibrin and erythrocyte (Fig. 1.3). Organised white thrombus and non-organised red thrombus can be found in stable clots and unstable clots, respectively. Red thrombi are the result of stagnation of blood flow, resulting in a clot containing all elements of normal blood, and they contain more enmeshed erythrocytes among sparse fibrin strands compared to precipitation or white thrombi. The red thrombi are expected to progress to organised white thrombi; otherwise, they may promote an inflammatory reaction, eventually leading to the disintegration of the aneurysm wall with subsequent rupture. Achieving organised white thrombi may reduce the probability of post-treatment rupture, and non-organised red thrombi have also been suggested as a potential predictor for unsatisfactory treatment results [Fischer et al., 2012, Sarrami-Foroushani et al., 2019, Turowski et al., 2011]. Controlled thrombosis is the main aim of endovascular treatments and the generation of stable white thrombi is often regarded as a positive post-treatment response [Ngoepe et al., 2018].

1.2 Thrombosis Modelling in IAs

Thrombosis is a biological response closely linked to IAs and aneurysmal haemodynamics. In unruptured IAs, thrombosis (spontaneous or device-induced) can either stabilise the aneurysm or accelerate the path to rupture [Ngoepe et al., 2018]. Currently,

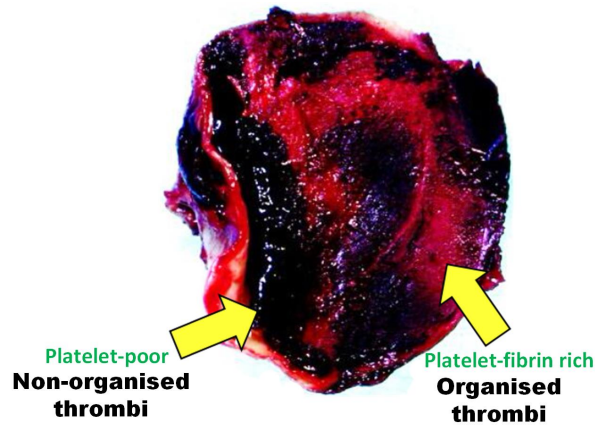


Figure 1.3: Histology of non-organised red (unstable) and organised white (stable) thrombi [Kulcsár and Szikora, 2012].

in vivo or image-based analysis of thrombosis haemodynamics in realistic anatomies and physiologies is very difficult. The existing literature thrombosis models typically consist of different physical subsystems (e.g., biochemical reactions, platelet activity, and haemodynamics) that are coupled together to simulate the thrombus formation process [Ngoepe et al., 2018]. Although there exists different literature thrombosis models that address various aspects of the thrombus formation process, integrated 3D thrombosis models combining haemodynamics and biochemical reactions that have possible clinical use for patient-specific cases are rare. The integrated thrombosis model originally developed by [Sarrami-Foroushani et al., 2019] incorporates biochemical reactions, platelet activity, and haemodynamics (model details will be described in Chapter 2). They defined a flow-induced platelet index (FiPi) as a quantitative measure of thrombus stability. FiPi quantifies the effect of blood flow on the transport of platelets to and from the site of thrombus formation and, thus, on the final platelet content of the formed thrombus. This model is not only capable of predicting both the haemodynamic changes and the thrombus formation after endovascular treatment but is also able to predict the long-term thrombus stability by investigating the thrombus composition. However, this model has never been calibrated or validated based on real patient clinical data, and it is computationally expensive; for example, simulation of thrombosis in a flow-diverted aneurysm can take up to one month using 96 cores on ARC4 (<https://arcdocs.leeds.ac.uk/>, all compute nodes contain Intel Xeon Gold 6138 CPUs). This thesis aims to improve both the credibility and efficiency of patient-specific com-

putational thrombosis modelling based on [Sarrami-Foroushani et al. \[2019\]](#)'s work. The improved thrombosis modelling workflow might be able to determine the best treatment course (e.g., coiling only, stenting only or the combination of coiling and stenting, and different types and sizes of medical devices) for an individual after assessment and validation, and further contribute to in silico clinical trials.

1.3 Thesis Contributions and Overview

This thesis aims to improve both the reliability and efficiency of patient-specific computational thrombosis modelling to reduce the gap between computational thrombosis modelling and possible clinical applications (Fig. 1.4). To do this task, we look at three critical aspects of patient-specific thrombosis modelling: calibrate the trigger thresholds of thrombosis initiation for use in thrombosis models, identify the most influential parameters in thrombosis modelling and validate the thrombosis model based on real clinical IAs, and accelerate patient-specific aneurysmal haemodynamics and thrombosis modelling. The details of the research motivations and thesis contributions are as follows:

- **Calibrate the trigger thresholds for thrombosis initiation against population-level clinical spontaneous thrombosis prevalence.** The most challenging part of a mechanistic model of thrombus formation in aneurysms is how to properly describe thrombosis initiation. Computational fluid dynamics (CFD) models use haemodynamic surrogates in thrombosis initiation, with residence time (RT) and shear rate (SR) being the most widely used parameters in flow stasis-induced thrombosis models. However, there is no consensus on the trigger thresholds, with different values used throughout the literature. Therefore, RT and SR thresholds need to be calibrated for use in thrombosis models. In addition, we also improve our thrombosis model by narrowing the thrombus formation region just near the wall before treatment, as in the real situation, the thrombus cannot be suspended in an aneurysm lumen on its own without any anchors.
- **Perform comprehensive sensitivity analysis to identify the most influential model parameters and then validate our thrombosis model based on real clinical IAs.** To have a robust computational thrombosis model for possible clinical use, it is essential to assess the model's credibility through

comprehensive sensitivity analysis of model parameters and validation studies based on clinical information of real patients. We identify the most influential factors of aneurysmal thrombosis modelling through a comprehensive global sensitivity analysis and further validate the thrombosis model based on a real patient case (partial thrombosis before treatment and residual neck after immediate flow-diverter and coiling treatment) using patient-specific parameters for those identified as influential ones and the previously calibrated trigger thresholds of thrombosis initiation.

- **Accelerate patient-specific aneurysmal haemodynamics and thrombosis modelling.** We create a fully automatic workflow executed on a cloud computing platform, MULTI-X (<https://multi-x.org>), that generates volumetric meshes, sets patient-specific boundary conditions using a statistical population model, assembles and executes fluid dynamic simulations, and provides patient-specific intra-aneurysmal flows and thrombus formation information. However, the thrombosis modelling using ANSYS CFX is very time-consuming, e.g., the simulation of thrombosis in a flow-diverted aneurysm can take up to one month using 96 cores. Therefore, we also investigate physics-informed deep learning models of thrombus formation by utilising the power of physics-informed neural networks and GPUs.

The following chapters in this thesis are organised as follows:

Chapter 2: This chapter introduces the background of aneurysmal haemodynamics and thrombosis modelling and gives details of our patient-specific aneurysmal haemodynamics and thrombosis modelling workflow. In addition, my technical contributions in automating the workflow, improving virtual coiling for wide-neck aneurysms, and narrowing thrombosis initiation to areas near the wall are also described at the end of this chapter.

Chapter 3: This chapter presents first how we establish the clinical prevalence of spontaneous thrombosis (ST) in IAs with different characteristics and different demographics, then how we calibrate the haemodynamic thresholds (RT and SR) of thrombus formation by matching our numerical ST prevalence to the real clinical data, and finally investigate the differences in the ST prevalence and aneurysmal haemodynamic factors (RT and SR) in normotensive and hypertensive patients. This study is enabled

through a fully automatic multi-scale modelling workflow that we created to accelerate population-based *in silico* studies.

Liu Q., Sarrami-Foroushani A., Wang Y., MacRaïld M., Kelly C., Lin F., Xia Y., Song S., Ravikumar N., Patankar T., Taylor Z., Lassila, T., Frangi, A.F.. Haemodynamics of Thrombus Formation in Intracranial Aneurysms: An in Silico Observational Study. APL Bioengineering. 2023 Sep 1 (JCR Q1, IF6.6, Editor's pick).

Chapter 4: This chapter identifies the most influential factors of our thrombosis model through a comprehensive global sensitivity analysis and further validates the thrombosis model based on a real patient case using patient-specific parameters for those identified as influential ones and the previously calibrated trigger thresholds of thrombosis initiation.

Liu Q., Lassila, T., Lin F., Patankar T., Islim F., MacRaïld M., Song S., Xu H., Chen X., Taylor Z., Sarrami-Foroushani A., Frangi, A.F.. Key Influencers in an Aneurysmal Thrombosis Model: A Sensitivity Analysis and Validation Study. APL Bioengineering. 2025 Feb 11 (JCR Q1, IF6.6, Editor's pick).

Chapter 5: This chapter is to investigate physics-informed deep learning models of thrombus formation. We investigate how PINNs perform in solving ADR equations and whether better time-marching schemes can improve the long-term stability of PINNs.

Liu Q., Lassila T., Nie L., Shone F., MacRaïld M., Taylor ZA., Sarrami-Foroushani A., Frangi A.F.. Time Discretisation in the Solution of Advection-Diffusion-Reaction Equations with PINNs. Bioengineering & Translational Medicine (2025), under review.

Chapter 6: This chapter concludes the thesis and discusses the outlooks and future works.

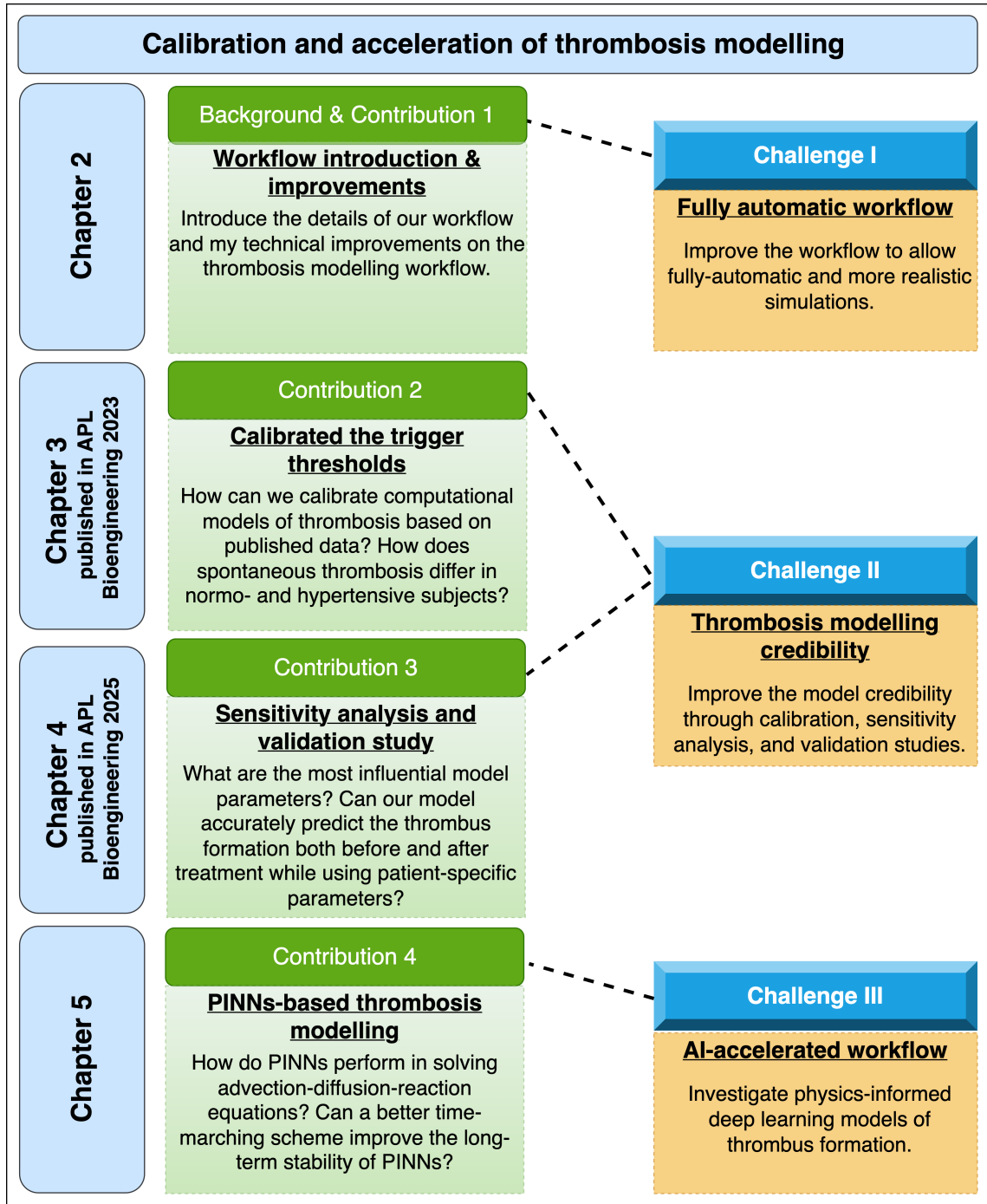


Figure 1.4: A graphical representation of the thesis structure, and the contribution of each chapter.

CHAPTER 2

Medical Image-Based Patient-Specific CFD
Workflow for Thrombus Formation in
Intracranial Aneurysms

Medical image-based CFD of IAs has become a widely-used tool for elucidating the role of haemodynamic forces in aneurysm development and rupture [Valen-Sendstad et al., 2018]. At the same time, it is well-known that an image-based CFD workflow is subject to numerous sources of uncertainty along its workflow, e.g., the image quality of the aneurysm; digital segmentation of the aneurysm and vessel (thresholds, filtering, smoothing, etc.); inlet flow boundary conditions; rigid wall assumption; and other CFD solver settings. In this chapter, I will introduce the details of our CFD workflow (Fig. 2.1), the common sources of uncertainty and our effort to increase the credibility of our workflow.

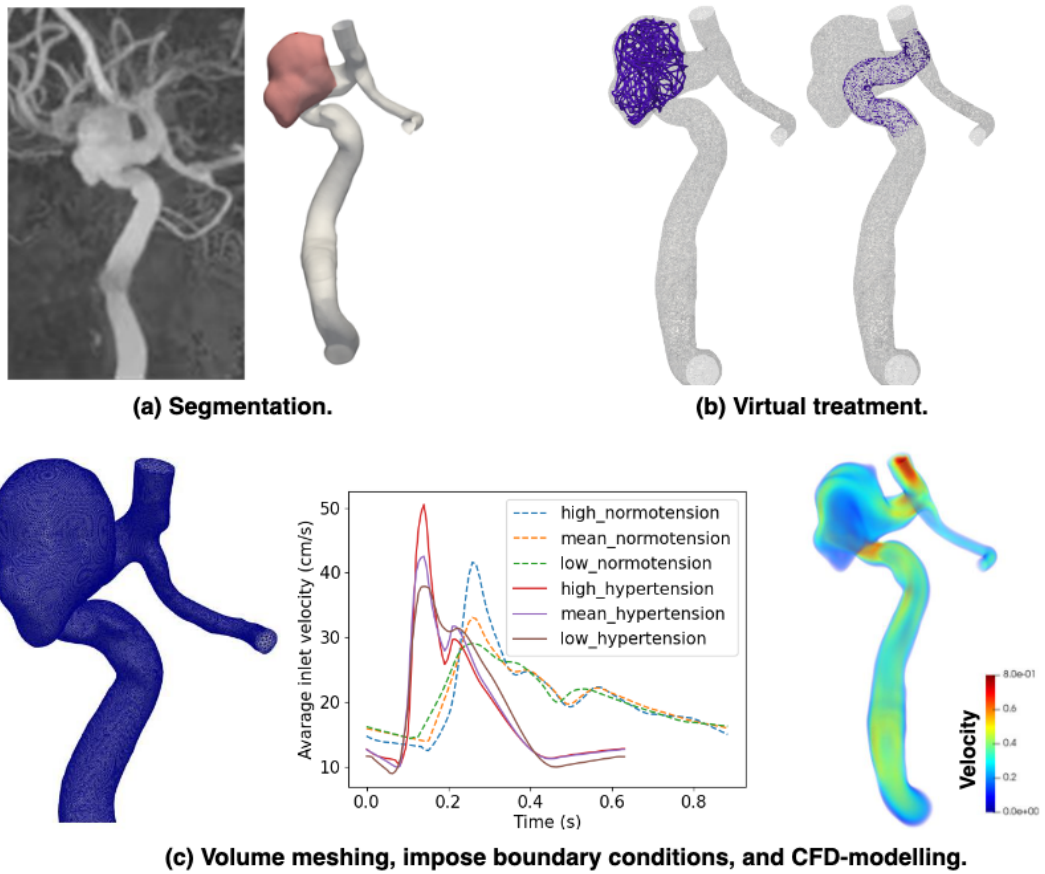


Figure 2.1: Medical image-based CFD workflow. (a) Patient’s angiogram and vascular surface model. (b) Virtual treatment: coiling (left) and stenting (right). (c) Volume meshing using ANSYS ICEM CFD v19.3, impose patient-specific inlet flow waveforms, and run simulations in ANSYS CFX v19.3.

2.1 Vascular Blood Flow Modelling

2.1.1 Aneurysm Imaging and Digital Segmentation

With the development of CT angiography (CTA) [Chappell et al., 2003], magnetic resonance angiography (MRA) [Sailer et al., 2014], and 3D rotational angiography (3DRA) [van Rooij et al., 2008], the image-based patient-specific analysis of the haemodynamics of IAs has been increasingly important for diagnosis, treatment plan, and follow-up [Ren et al., 2016]. For medium and large IAs, MRA achieves diagnostic accuracy that is equivalent to that of CTA. However, for aneurysms less than 5 mm, most studies have shown CTA to be superior, with MRA sensitivity dropping to 56% [Jacobson and Trobe, 1999, Jayaraman et al., 2004, Korogi et al., 1999]. Compared with other imaging technologies, 3DRA can depict considerably more small additional angiographic aneurysms (e.g., 1-3 mm) for which the sensitivity of CTA and MRA is known to be less than 90% [Alberico et al., 1995]. In clinical practice, CTA and MRA have become the first-line imaging modalities for IAs owing to their minimally invasive nature. However, as the reconstructed 3DRA images can show only the enhanced vascular lumina, which allows observing any desired region without hiding over projecting bony structures, the diagnosis and measurement of IAs can be performed more accurately by using 3DRA technology [Ren et al., 2016]. Therefore, despite greater invasiveness and increased risk to the patient, 3DRA remains a useful and critically important tool in the detection and treatment of IAs and is usually used as the gold standard.

The process of subdividing an image into its constituent parts that are homogeneous in feature is called image segmentation, and it aims to extract some useful information [Ramesh et al., 2021]. For generating an aneurysm model, the first step is to segment image data in order to obtain the 3D geometry of the aneurysm with its proximal and distal vessels. The segmentation process depends on the imaging modality, with 3DRA typically considered the gold standard due to its high spatial resolution [Rayz and Cohen-Gadol, 2020]. Alternatively, aneurysmal geometries can be obtained from CTA and MRA data. While CTA and MRA have no significant differences in reproducing aneurysm geometry [Ren et al., 2016], Geers et al. [2011] reported significant differences in aneurysm necks reconstructed from CTA versus those obtained from 3DRA, which were explained by the difference in imaging resolution. The ac-

curacy of image-based CFD simulation is highly dependent on vessel and aneurysm geometry, with medical image segmentation methods directly affecting the accuracy of the aneurysm model construction. [Sen et al. \[2014\]](#) assessed three segmentation methods for the analysis of 45 IA models in terms of geometry shape, volume, and haemodynamic results. Although based on the same CTA data, different methods of image segmentation generated variations in shape and volume, thus resulting in significant differences in computed haemodynamic parameters. Image resolution, quality, and segmentation methods are considered to be major sources of variability for image-based patient-specific modelling [[Berg et al., 2018](#), [Steinman and Pereira, 2019](#)].

The patient image data (3DRA) in this thesis are from the @neurIST [[Iavindrasana et al., 2008](#), [Villa-Uriol et al., 2011](#)] project. All images are anonymised, respecting the @neurIST ethical use approval for the use of patient data (<http://www.aneurist.org>). We use a 3D multi-task segmentation neural network [[Lin et al., 2023](#)] to complete the segmentation of the vessel and aneurysm dome automatically. This segmentation network achieves an average Dice score of 0.82 by using the manually segmented results [[Iavindrasana et al., 2008](#), [Villa-Uriol et al., 2011](#)] as reference and an average surface-to-surface error of 0.20 mm (less than the in-plane resolution (0.35 mm/pixel)). The details of the segmentation algorithm and segmentation results can be found in [[Lin et al., 2023](#)]. From the segmentation, we acquire patient-specific vascular surface models that are used to generate unstructured volumetric meshes. We use ANSYS ICEM CFD v19.3 (Ansys Inc. Canonsburg, PA, USA) to generate unstructured volumetric meshes. To discretise the computational domain, including the vascular region and aneurysm sac, tetrahedral elements with a maximum edge size of 0.2 mm and five layers of prismatic elements with a maximum edge size of 0.1 mm are used. [Sarrami-Foroushani et al. \[2019\]](#) performed mesh convergence tests based on the inflow rate at the aneurysm neck and the sac-averaged concentrations of the fibrin and platelets. They demonstrated that the above-mentioned mesh resolution was fine enough to achieve an accurate flow solution. In addition to tests by [Sarrami-Foroushani et al. \[2019\]](#), we performed a mesh independence test based on the maximum residence time (RT) in the aneurysm sac [[Liu et al., 2023](#)]. When using a fine mesh (tetrahedral elements with a maximum edge size of 0.1 mm and five layers of prismatic elements with a maximum edge size of 0.1 mm) as the reference in the test, the maximum RT obtained on the above-mentioned element sizes (tetrahedral elements with maximum edge size of 0.2 mm and five layers

of prismatic elements with a maximum edge size of 0.1 mm) differed from the maximum RT of the reference mesh by 2.5%.

2.1.2 Blood Flow Modelling

Although the rheology of blood can be described by using a Newtonian model with a constant viscosity or by using non-Newtonian models that consider the shear-thinning behaviour of blood [Sarrami-Foroushani et al., 2017], almost all CFD teams in the literature [Valen-Sendstad et al., 2018] assumed Newtonian rheology, with blood density typically between 1.05 and 1.06 g/cm³, and viscosity almost equally divided between 0.0035 and 0.004 Pa · s. In the literature, some studies have reported the magnification of non-Newtonian effects in slow-flow regions [Morales et al., 2013, Rayz et al., 2008]. However, based on the review work and meta-analysis of Sarrami-Foroushani et al. [2017], the differences between aneurysmal wall shear stress (WSS) values produced by different rheological models have not been shown to be significant, and the influence of blood rheological models on the WSS distribution is also negligible.

The computational study of blood flow in brain arteries has usually been approached by the assumption that the considered arterial wall moments are significantly small [Ramana Reddy and Srikanth, 2020]. Accordingly, wall distensibility is neglected in almost all CFD simulations of blood flow in aneurysms, and a no-slip boundary condition is imposed [Sarrami-Foroushani et al., 2017, Valen-Sendstad et al., 2018]. Although the meta-analysis [Sarrami-Foroushani et al., 2017] suggested an effect of wall distensibility on the prediction of WSS magnitude by CFD, quantitative comparisons based on global space-averaged measures showed an agreement between the rigid-wall and non-rigid-wall (flow-structure-interaction) simulations when the distribution of WSS on the aneurysm wall or the main flow characteristics in the aneurysm are of interest. Currently, in the context of IA modelling, almost all teams assumed rigid walls with no-slip boundary conditions.

Inflow boundary conditions are either taken from the literature or obtained from patient-specific measurements [Sarrami-Foroushani et al., 2017]. Comparing results obtained from simulations with typical literature-based and patient-specific inflow boundary conditions has observed great differences in the magnitude of aneurysmal WSS and oscillatory shear index (OSI). Although patient-specific inlet boundary conditions are superior to the literature-based inflow conditions, in vivo measurement-derived inflow

boundary conditions are usually unavailable for population-level aneurysm modelling.

At the outlets, the commonly used approaches are zero-pressure, Murray’s law (divide outflows according to the cube of the diameter), and reduced-order models, with zero-pressure imposed by the majority of CFD teams [Valen-Sendstad et al., 2018]. Despite variability in outflow boundary condition implementations across computational methodologies, the flow distribution to the dominant vascular branch demonstrated remarkably consistency in haemodynamic simulations, as evidenced by Valen-Sendstad et al. [2018]. Outflow boundary conditions appeared to have only a minor impact on the variability of outflow divisions. However, they did not test whether and how these might impact flow and WSS patterns for individual aneurysms. In a study (of which I am a coauthor) named “Off-label in-silico flow diverter performance assessment in posterior communicating artery aneurysms”, we compared imposing an 80:20, 60:40, 50:50, 40:60, 20:80 mass flow split at the middle cerebral artery (MCA) and the anterior cerebral artery (ACA) outlets with the default zero pressure condition we used in the posterior communicating artery (PComA) trial. We found that downstream conditions are not very important for the aneurysm flow but that conditions applied to any branch vessels that originate in the vicinity of the aneurysm are important (e.g., the PComA). This PComA trial study was submitted to the Journal of NeuroInterventional Surgery and received a major revision comment (June 2024).

2.1.3 Patient-Specific Inlet Flow Waveforms

Previous studies have found that inlet flow boundary conditions of CFD models affect IA haemodynamics, with inter-subject variability in cerebral blood flow found to be 10-20% [Bowker et al., 2010, Geers et al., 2014, Lassila et al., 2020, Xiang et al., 2014]. With in-vivo measurement-derived boundary conditions unavailable for our cohort, we used a previously developed Multivariate Gaussian Model (MGM) [Sarrami-Froushani et al., 2016] to generate patient-specific boundary conditions as internal carotid flow waveforms. The MGM model was trained and calibrated using the data from 17 healthy young adults [Ford et al., 2005]. A virtual population of 1000 normotensive waveforms was then generated, and three of them, i.e., high, mean, and low, were selected to maximise the variability across the entire virtual population (by selecting high/low as the upper/lower bounds of the 1000 waveforms). To consider inter-subject variability, these three representative waveforms were used as inlet boundary conditions for flow

simulations. To enable population-wide comparisons, Poiseuille’s law was used to scale the mean waveform such that the time-averaged WSS was 1.5 Pa at the inlet for each patient (elimination of mean effect).

2.2 Virtual Endovascular Treatment

2.2.1 Coiling

Endovascular coiling is a well-established therapy for treating IAs. The novelty of this approach is the catheter insertion of a coil, which is soft and adapts to different sizes and shapes of aneurysms, within the aneurysm so as to reduce haemodynamic exchange between the aneurysm and parent artery (Fig. 2.1 (b)). Although coiling is associated with lower mortality and morbidity rates compared with surgical clipping, its outcome is strongly influenced by packing density and is not always predictable [Morales et al., 2011a]. Packing density is defined as the ratio between the inserted coils and aneurysm volume, and usually, the aneurysms are packed as densely as possible.

The virtual coiling technique used in this thesis was proposed by Morales et al. [2010]. The coils are defined by diameter and length, and the algorithm generates the centreline of the coil with points separated by a limited distance. Each coil is progressively placed by advancing its tip, which starts from an initial position inside the aneurysm. The tip motion is constrained by the aneurysm dome, its ostium, and other previously inserted coils. The technique sequentially places the coils inside the aneurysms until either the known patient-specific number of coils or the desired packing density is achieved. The details of the virtual coiling technique can be found in [Morales et al., 2010, 2011a,b].

2.2.2 Stenting and Flow Diverter

As mentioned before, the most difficult IAs to treat with coiling are those with a wide neck (neck size ≥ 4 mm) due to the difficulty in stabilising the coils inside the aneurysm [Pierot and Biondi, 2016]. This prompted the development of more complex endovascular techniques, including stent-assisted coiling. The initial experience of aneurysm stenting showed relatively poor safety, as the porosity of early stents was high, and so occlusion by flow diversion was not possible. Then, improvements were made to the initial stent design to create a flow-diverter or flow-diverting stent [Phillips

[et al., 2010](#)]. Flow diverters are low-porosity stents designed to reduce haemodynamic exchange between the aneurysm and parent vessel, which helps to form thrombi within the aneurysm sac (Fig. 2.1 (b)). Flow diverters have revolutionised the endovascular management of unruptured, complex, wide-neck, and giant aneurysms [[Al-Mufti et al., 2020](#)]. Nowadays, several types of flow diverter devices have been approved for the treatment of IAs: the Pipeline Embolization Device (Covidien), the Silk (Balt), the Flow Re-direction Endoluminal Device (Microvention), the p64 Flow-Modulation Device (Phoenix), and the Surpass Flow-Diverter (Stryker).

We used the Fast Virtual Stenting method [[Larrabide et al., 2012](#)] to create the geometric models of the deployed flow diverters. To virtually release the stent, the first step is to initialise the mesh inside the vessel geometry, which includes: (1) the creation of the simplex points around the vessel centreline; (2) the creation of the simplex mesh connectivity using the previously created points; and (3) the creation of the stent mesh. Then, an iterative algorithm can be started to update the stent mesh position based on the vascular geometry. The details of the Fast Virtual Stenting method and the in silico application of this method can be found in [[Larrabide et al., 2012](#), [Liu et al., 2023](#), [Sarrami-Foroushani et al., 2019, 2021](#)].

2.3 Aneurysmal Thrombosis Modelling

2.3.1 Hemostasis and Thrombosis

Hemostasis [[Colman, 2006](#), [Weitz and Fredenburgh, 2013](#)] is a complex and critical physiological process that stops bleeding at the site of an injury while maintaining normal blood flow elsewhere in the circulation, while thrombosis [[Yesudasan and Averett, 2019](#)] is the process of the formation of a blood clot inside a blood vessel, obstructing the flow of blood through the circulatory system. Both hemostasis and thrombosis involve blood clotting, and under physiological conditions, the formation of a blood clot is a well-regulated process that includes three phases: (1) primary hemostasis, (2) secondary hemostasis/coagulation, and (3) fibrinolysis [[Goeijenbier et al., 2012](#)]. The details of hemostasis and thrombosis can be found in [[Colman, 2006](#), [Neubauer and Zieger, 2022](#), [Risman et al., 2023](#), [Smith et al., 2015](#)]. The formation of a blood clot is very complex with at least 80 coupled reactions that regulate clot growth. The most important and commonly-modelled reactions are platelet activation, thrombin generation

2.3 Aneurysmal Thrombosis Modelling

and fibrin generation.

The key difference between normal hemostasis and aneurysmal thrombosis relates to how primary hemostasis is triggered (Fig. 2.2). In normal hemostasis, initiation is triggered by blood exposure in the endothelial tissue caused by injury to the vascular wall, while in cerebral aneurysm thrombosis, it has been linked to endothelial damage present in the aneurysm sac, wall inflammation, blood-borne tissue factor, and the contact with artificial surfaces after treatment [Giesen et al., 1999, Ngoepe et al., 2018, Sarrami-Foroushani et al., 2017, Smith et al., 2015].

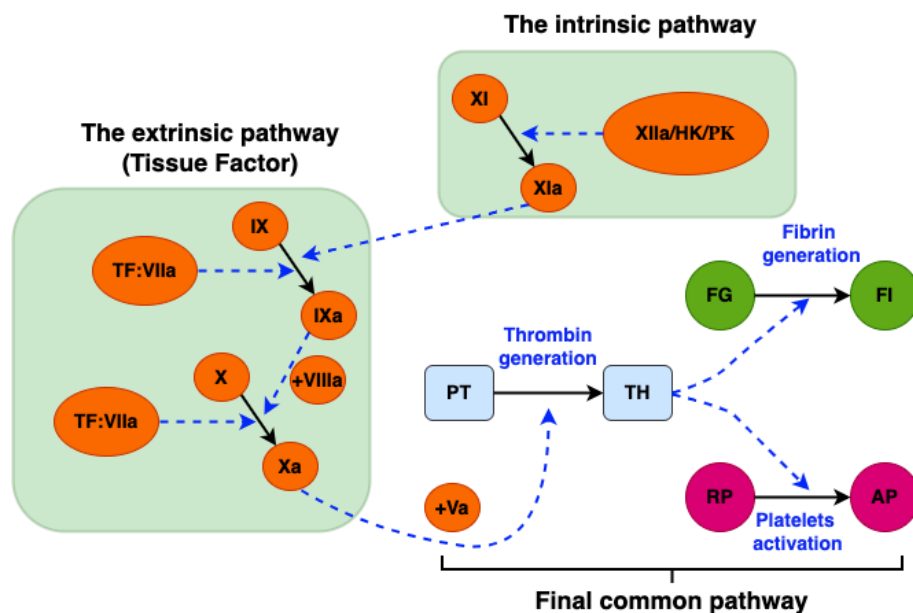


Figure 2.2: Overview of the coagulation cascade. The coagulation cascade is initiated in two different mechanisms: the intrinsic pathway (initiated by factors within the blood) and the extrinsic pathway (triggered by external trauma). Both pathways converge at the production of factor Xa. The common pathway results in the generation of a burst of thrombin, which converts fibrinogen to fibrin and activates platelets. Note: XIa represents the activation of XI. HK, high-molecular-weight kininogen; PK, plasma prekallikrein; TF, tissue factor; TF:VIIa, tissue factor binds factor VIIa; PT, prothrombin; TH, thrombin; FG, fibrinogen; FI, fibrin; RP, resting platelets; AP, activated platelets.

2.3.2 Literature Thrombosis Models

The multi-scale and multi-physics nature of thrombosis has inspired a wide range of modelling approaches applied to various phenomena that aim to address how a thrombus forms [Gutierrez et al., 2023]. Gutierrez et al. [2023] classified the commonly used thrombosis modelling techniques as (a) continuum models in which quantities such as velocity or concentration of blood constituents are spatially averaged and mapped onto finite regions in the computational domain or (b) particle models in which flow and chemical quantities are, instead, represented as collections of particles. Continuum models usually model large-scale processes on the order of millimetres [Gutiérrez et al., 2021, Steinman, 2002, Taylor and Figueroa, 2009] and discretise a blood domain in order to solve algebraic equations that represent differential equations. In continuum models, cells and biochemical species such as platelets are commonly treated as averaged homogeneous species as they are much smaller than the whole modelling domain. Alternatively, particle models use particles instead of a mesh to represent flow, platelets, and other biochemical species. Particle models can capture the deformation and collision physics of platelets and red blood cells in flow [Qi and Shaqfeh, 2018, Skorzewski et al., 2013, Vahidkhah et al., 2014]. Current laptops can sufficiently solve steady flow in a patient-specific vessel using continuum models within hours. However, transient flow in complex geometries involving turbulence or particle-based models of thousands of particles can take weeks to months, even on a high-performance computing cluster. It may not be feasible on a standard computer. How computational models can be applied to simulate various thrombosis processes depends on the end goal for the model and is largely driven by the practical constraints of computational cost (time and computational power) required for a simulation. More details about the advantages and disadvantages of existing literature continuum and particle models and how computational models can be applied to simulate various thrombosis processes were summarised and discussed in [Gutierrez et al., 2023]. Although different modelling methods can be coupled as informed by the scale and physics, the development of an all-encompassing computational model of thrombosis, combining all relevant underlying phenomena for patient-specific applications remains impractical, and, instead, it is necessary to simplify models and to focus on specific questions.

Ngoepe et al. [2018] summarised the literature on computational models of physiological (natural hemostasis) and pathological (thrombosis) clotting. They found that

2.3 Aneurysmal Thrombosis Modelling

these models typically consist of different physical subsystems (e.g., platelets, coagulation, and haemodynamics) that are coupled together to simulate the thrombus formation process [Ngoepe et al., 2018]. The platelet models [Chatterjee et al., 2010, Filipovic et al., 2008, Flamm et al., 2012, Mody and King, 2008, Purvis et al., 2008] focus on the adhesion, activation, and aggregation of platelets and sometimes the coagulation reactions supported by the platelet membranes; the coagulation network models [Hemker et al., 2000, Hemker and Kremers, 2013, Hemker et al., 2002, Hockin et al., 2002, Mann et al., 2006, Wagenvoord et al., 2006] focus solely on the biochemical reactions which result in the formation of thrombin and ultimately, fibrin; the integrated models [Anand et al., 2006, 2008, Leiderman and Fogelson, 2011, Leiderman et al., 2008, Sarrami-Foroushani et al., 2019, Sorensen et al., 1999, Storti and Van De Vosse, 2014, Xu et al., 2008] incorporate platelet activation/aggregation, biochemical reactions, and haemodynamics, which can provide a mechanism for coupling the different systems that contribute to the clot formation process and are therefore more readily applicable to specialised aneurysmal thrombosis models. Although various hemostasis and thrombosis models have been developed and presented in the literature, integrated models designed specifically for brain aneurysm thrombosis are rare. Ouared et al. [2008] defined a mesoscopic model for aneurysmal thrombus formation, implementing platelets transport, adhesion, and aggregation on top of a 2D Lattice Boltzmann haemodynamics model. In their model, thrombosis starts and grows below a shear rate (SR) threshold and stops above it. Bedekar et al. [2005] first combined biochemical reactions with haemodynamics in patient-derived brain aneurysm geometries. They formulated an integrated model that accounts for a detailed description of clot formation biochemistry, activation mechanisms, surface adhesion, and aneurysmal haemodynamics. Before that, the complex biochemical reactions were usually implemented in idealised geometries, while only the haemodynamics were calculated using realistic geometries. By building the trigger mechanism on the SR thresholding approach introduced by [Ouared et al., 2008], Ngoepe and Ventikos [2016] developed a comprehensive computational model of clotting that accounts for biochemical reactions coupled with 3D haemodynamics in image-derived patient aneurysms in the presence of a virtually deployed stent. The reactions were initiated by expressing TF along a portion of the aneurysm wall where the SR was below a given threshold. Ou et al. [2017] assumed that the concentration of fibrin was seen to increase dramatically, signalling the initiation

of coagulation when SR was decreased to below 10 s^{-1} . Their model has been validated by studies in an experimental rat model and then applied to an idealised saccular aneurysm treated with flow-diverter. Although SR is considered one of the important parameters that contribute to thrombosis, Rayz et al. [2010] found that a model with both low SR and high residence time (RT) could predict thrombosed areas significantly better than the models using RT or SR alone. The RT of a fluid particle (or local RT) is the time that the particle has spent inside a domain since its entry [Ghirelli and Leckner, 2004]. Sarrami-Foroushani et al. [2019] assumed thrombosis to initiate and progress in regions where SR fell below a specific threshold (25 s^{-1}) and RT was greater than a threshold (5 s). Their novel contribution combines platelet activation and transport with fibrin generation, which is key to characterising stable and unstable thrombus. Their integrated model coupled haemodynamics and biochemical reactions and defined a flow-induced platelet index (FiPi) as a quantitative measure of thrombus stability. Sarrami-Foroushani et al. [2019]’s model has been validated against an in vitro phantom study of two flow-diverting stents with different sizing.

In summary, an ideal computational thrombosis model would be capable of predicting both the haemodynamic changes and clot coagulation after endovascular treatment and would determine the best course for an individual [Ngoepe et al., 2018]. Although there is a wide range of hemostasis and thrombosis models in the literature, most of the physiological (thrombosis) models have been implemented in two-dimensional frameworks only. The integrated 3D models designed specifically for brain aneurysm thrombosis and that can be applied to patient-specific aneurysmal thrombosis modelling both before and after treatment are rare. The integrated 3D thrombosis model originally developed by Sarrami-Foroushani et al. [2019] incorporates biochemical reactions, platelet activity, and haemodynamics, and this model could be considered as a useful tool in clinical decision-making after further population-level model credibility assessment.

2.3.3 Residence Time

The most challenging part of a mechanistic model of thrombus formation in aneurysms is the mechanism used to describe thrombosis initiation, as it is complicated and not fully understood yet [Ngoepe et al., 2018, Sarrami-Foroushani et al., 2017]. It has been shown that aneurysmal thrombi form or at least deposit in slow flow and

2.3 Aneurysmal Thrombosis Modelling

low shear regions [Malaspinas et al., 2016, Ou et al., 2017, Rayz et al., 2008, Sarrami-Foroushani et al., 2017]. CFD models use blood flow stasis as a surrogate for thrombosis initiation mechanisms, with RT and SR being the most widely used parameters in flow stasis-induced thrombosis models [Cebal et al., 2014, Ouared et al., 2016, Rayz et al., 2010, Sarrami-Foroushani et al., 2019].

The RT of a fluid particle (or local RT) is the time that the particle has spent inside a domain since its entry [Ghirelli and Leckner, 2004]. The details of the definition of RT can be found in [Ghirelli and Leckner, 2004, Levenspiel, 1998]. The mean RT at a point can be measured by introducing a pulse of tracer in the inlet to the domain, while measuring the tracer concentration at a given point continuously. The mean RT is defined as:

$$RT \equiv \frac{\int_0^\infty C_{RT} t dt}{\int_0^\infty C_{RT} dt}, \quad (2.1)$$

where C_{RT} is the local concentration of RT at a given point, and t is the time elapsed since the injection of the tracer.

The literature RT calculation methods can be classified into Eulerian (e.g., Eulerian RT, Virtual-ink RT, Eulerian indicator RT, Point-wise RT) and Lagrangian (e.g., Particle RT, Mean exposure time) approaches, where several measures have been created to calculate RT [Reza and Arzani, 2019]. We used the Eulerian RT approach (a widely-used effective approach) [Liu et al., 2023, Menichini and Xu, 2016, Rayz and Cohen-Gadol, 2020, Sarrami-Foroushani et al., 2019] in our workflow, and RT was modelled as a tracer passively transported with the blood flow by solving the following advection-diffusion-reaction equation:

$$\frac{\partial C_{RT}}{\partial t} + \mathbf{u} \cdot \nabla C_{RT} = D_{RT} \nabla^2 C_{RT} + 1, \quad (2.2)$$

where t is time, \mathbf{u} is the velocity vector, C_{RT} is the local concentration of RT, and D_{RT} represents the self-diffusivity of the flow ($D_{RT} = 1.14 \times 10^{-11} m^2 s^{-1}$) [Harrison et al., 2007, Menichini and Xu, 2016]. The source term considers a unit increase in the concentration of RT for each unit increase in time [Menichini and Xu, 2016].

Three main triggers of flow stasis-based thrombosis models appear in the literature: (1) high RT alone; (2) low SR or WSS alone; and (3) high RT and low SR/WSS in combination. However, there is no clear consensus on the values of the trigger thresholds. In Chapter 3, we calibrate these trigger thresholds based on clinical spontaneous throm-

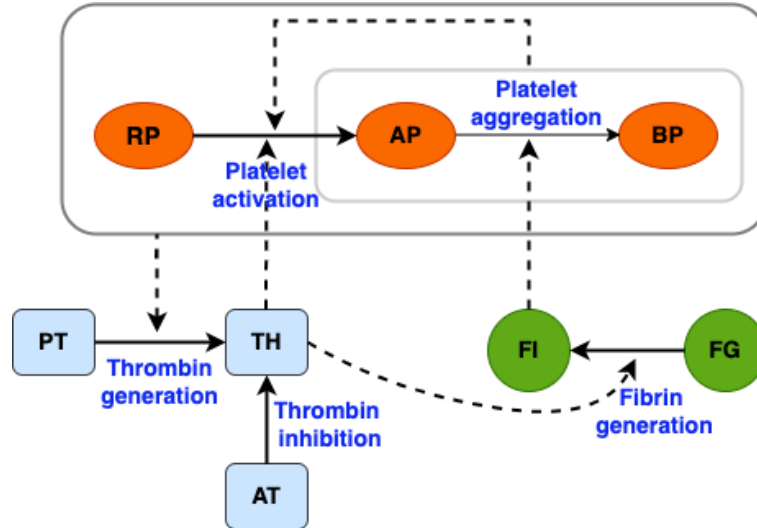


Figure 2.3: The thrombosis model in our group including four main biochemically-coupled events: Thrombin generation, Fibrin generation, Platelet activation, and Platelet aggregation.

bosis prevalence, and this calibration study paper was published in APL Bioengineering as an editor’s pick paper [Liu et al., 2023].

2.3.4 The Flow Stasis-Induced Thrombosis Model

The flow stasis-induced thrombosis model used in our group was originally developed by Sarrami-Foroushani et al. [2019]. Sarrami-Foroushani et al. [2019] assumed thrombosis to initiate and progress in regions where RT was greater than a threshold (e.g., 2.0 s) and SR fell below a specific threshold (e.g., 25 s^{-1}). The novelty of this integrated thrombosis model (incorporating biochemical reactions, platelet activity, and haemodynamics) is that they defined a flow-induced platelet index (FiPi) as a quantitative measure of thrombus stability. FiPi quantifies the effect of blood flow on the transport of platelets to and from the site of thrombus formation and thus on the final platelet content of the formed thrombus. This model is not only capable of predicting both the haemodynamic changes and thrombus formation after endovascular treatment but is also able to predict the long-term thrombus stability by investigating the thrombus composition.

As shown in Fig. 2.3, four main biochemically-coupled events that result in thrombus of fibrin mesh and aggregated platelets were considered, with five biochemical

2.3 Aneurysmal Thrombosis Modelling

species: prothrombin (PT), thrombin (TH), anti-thrombin (AT), fibrinogen (FG), fibrin (FI), and three categories of platelets: resting platelets (RP), activated platelets (AP), fibrin bound aggregated platelets (BP). (1) Thrombin generation — conversion of prothrombin to thrombin on the surface of resting, activated, and bound platelets, also considered thrombin inhibition by anti-thrombin; (2) Fibrin generation — thrombin is able to convert fibrinogen into (insoluble) fibrin; (3) Platelet activation — resting platelets become activated by exposure to thrombin or other activated/bound platelets; and (4) Platelet aggregation — activated platelets attached to the fibrin network aggregate to form bound platelets.

Three-dimensional momentum equations for incompressible and Newtonian fluid, the Navier-Stokes equations, were used to describe blood flow. The vessel wall was assumed to be rigid [Humphrey and Taylor, 2008], and the no-slip wall boundary condition was imposed; the mean Reynolds number at the inlet was 338; a Poiseuille profile was imposed at the inlet; and a zero-pressure condition was prescribed at all outlets [Sarrami-Foroushani et al., 2019]. The Navier-Stokes equations for an incompressible Newtonian fluid are given by:

$$\rho \frac{\partial \mathbf{u}}{\partial t} + \rho(\mathbf{u} \cdot \nabla) \mathbf{u} = -\nabla p + \mu \nabla^2 \mathbf{u} - \mu \Phi(k_f, k_p) \mathbf{u}, \quad (2.3)$$

where \mathbf{u} is the velocity vector, t is time, and p is the pressure. Blood flow was regarded as an incompressible and Newtonian fluid with a constant density ρ of 1060 kg/m³ and viscosity μ of 0.004 Pa · s [Geers et al., 2014, Villa-Uriol et al., 2011]. To consider the effect of the thrombus on the fluid velocity field, without modelling the fluid-structure interaction, the blood thrombus was regarded as a porous medium with both fibrin and bound platelet components. A Darcy term, $\mu \Phi(C_f, C_p) \mathbf{u}$, was added to the momentum equations. The function $\Phi(C_f, C_p)$ was defined as:

$$\Phi(C_f, C_p) = \frac{1}{k_{fi}} \phi_p^{fi} + \frac{1}{k_{bp}} \phi_p^{bp}, \quad (2.4)$$

where k_{fi} and k_{bp} are permeabilities of the thrombus due to fibrin fibres and bound platelets, respectively. The Hill functions, of form $\phi_x^i = C_i^n / (C_i^n + C_{i,50}^n)$, ϕ_p^{fi} and ϕ_p^{bp} were used to make sure that there is no flow restriction in non-thrombosed regions, while flow restriction increases to half of its maximal value as fibrin and platelet concentrations approach 600 nM and 7×10^5 platelets/ μm^3 , respectively. We set $n = 4$ to ensure a sharp boundary between the clot and blood.

2.3 Aneurysmal Thrombosis Modelling

Denoted by C_{pt} , C_{th} , C_{at} , C_{fg} , C_{fi} , C_{rp} , C_{ap} , and C_{bp} , the bulk concentration of prothrombin, thrombin, anti-thrombin, fibrinogen, fibrin, resting platelets, activated platelets and bound platelets, respectively. The transport of each species was modelled using the advection-diffusion-reaction (ADR) equation (2.5).

$$\frac{\partial C_i}{\partial t} + (\mathbf{u} \cdot \nabla) C_i = D_i \nabla^2 C_i + S_i, \quad (2.5)$$

Where C_i is the species concentration, D_i is the diffusion coefficient, and S_i is the reaction term. For bound platelets, the advection and diffusion terms need to be removed to represent platelets adhered to the clot. The reaction source terms in equation (2.5) were as follows (more details can be found in [Sarrami-Foroushani et al., 2019]):

$$S_{pt} = -k_{th}^{rp} C_{rp} C_{pt} - k_{th}^{ap} C_{ap} C_{pt} - k_{th}^{bp} C_{bp} C_{pt} \quad (2.6)$$

$$S_{th} = k_{th}^{rp} C_{rp} C_{pt} + k_{th}^{ap} C_{ap} C_{pt} + k_{th}^{bp} C_{bp} C_{pt} - k_{th}^{at} C_{at} C_{th} \quad (2.7)$$

$$S_{at} = -k_{th}^{at} C_{at} C_{th} \quad (2.8)$$

$$S_{fg} = -S_{fi} = -k_{fi}^{th} C_{th} C_{fg} / (k_{m,fi}^{th} + C_{fg}) \quad (2.9)$$

$$S_{rp} = -k_{pa}^{th} \phi_{pa}^{th} C_{rp} - k_{pa}^{ap} C_{rp} \quad (2.10)$$

$$S_{ap} = k_{pa}^{th} \phi_{pa}^{th} C_{rp} + k_{pa}^{ap} C_{rp} - k_{pb} \phi_{pb}^{fi} C_{ap} \quad (2.11)$$

$$S_{bp} = k_{pb} \phi_{pb}^{fi} C_{ap} \quad (2.12)$$

Platelet activation by thrombin was assumed to occur when thrombin concentration was greater than 9×10^{-1} nM [Sorensen et al., 1999]. This was modelled by multiplying the associated reaction source term by a Hill function, ϕ_{pa}^{th} , with $n = 4$. The platelet recruitment and deposition were assumed to depend on the concentration of free platelets and the value of a function representing fibrin-platelet. This was modelled by multiplying the associated source term by a second-order Hill function ϕ_{pb}^{fi} with $C_{fi,50} = 60$ nM (10% of the threshold concentration, 600 nM, at which fibrin clot is assumed to

be formed). The details of all model parameters can be found in Table 4.1, Table 4.2, and Table 4.3, and more details can be found in [Liu et al., 2023, Sarrami-Foroushani et al., 2019].

FiPi was defined as the relative difference in platelet concentration between a closed and an open system:

$$FiPi = \frac{C_{bp}^{open} - C_{bp}^{closed}}{C_{bp}^{closed}} = \frac{C_{bp}^{open}}{C_{rp,0} + C_{ap,0}} - 1 \quad (2.13)$$

Where $C_{rp,0}$ and $C_{ap,0}$ are initial concentrations of resting and activated platelets in the clot-free blood, respectively. In a closed system with no inflow or outflow, the platelet content of the clot is equal to the initial concentration of platelets in the system. However, in an open system, because platelets can attach to the clot, the platelet content of the clot would differ from that in a closed system. FiPi quantifies the effect of blood flow on the movement of platelets in and out of the thrombus formation site, and thus on the final platelet content of the formed thrombus.

2.4 Summary of Our CFD Workflow

It is well-known that different CFD codes and approaches will produce differing results. Although medical image-based CFD of IAs has become a widely-used tool for elucidating the role of haemodynamic forces in aneurysm development and rupture, the CFD tools are subject to numerous sources of uncertainty [Valen-Sendstad et al., 2018]. The common sources of uncertainty [Sarrami-Foroushani et al., 2016, 2017, Valen-Sendstad et al., 2018] for the image-based CFD tools and our effort to increase the credibility of our model are outlined below. It should be noted that image segmentation and surface mesh generation are not part of this study.

1. **Digital segmentation of the vessel and aneurysm:** We used a 3D multi-task segmentation neural network to complete the segmentation of the vessel and aneurysm dome automatically. Using the manually segmented results [Iavindrasana et al., 2008, Villa-Uriol et al., 2011] as references, this segmentation network achieved an average Dice score of 0.81 and an average surface-to-surface error of 0.20 mm (less than the in-plane resolution (0.35 mm/pixel)) for aneurysm segmentation; and an average Dice score of 0.91 and average surface-to-surface error

of 0.25 mm for vessel segmentation. The details of the segmentation algorithm and performance can be found in [Lin et al. \[2023\]](#).

- 2. Mesh and time-step resolutions:** (1) We used ANSYS ICEM CFD v19.3 (Ansys Inc. Canonsburg, PA, USA) to generate unstructured volumetric meshes. To discretise the computational domain, including the vascular region and aneurysm sac, tetrahedral elements with a maximum edge size of 0.2 mm and five layers of prismatic elements with a maximum edge size of 0.1 mm were used. [Sarrami-Foroushani et al. \[2019\]](#) performed the mesh convergence tests based on the inflow rate at the aneurysm neck, and according to their tests, mesh independence was obtained for the above-mentioned element sizes. (2) Unless otherwise stated, the transient blood flow simulations were run for 3 cardiac cycles in the flow-only model and 200 cardiac cycles in the full thrombosis model. Each cardiac cycle was equally discretised into 200 steps [[Sarrami-Foroushani et al., 2019](#)]. CFX's adaptive time-stepping with minimum, maximum, and initial time steps of 0.0001s, 0.05s, and 0.01s was used in all simulations.

3. Blood flow modelling:

- **Newtonian assumption:** In the literature, blood rheology was often assumed to be Newtonian, but non-Newtonian effects were suggested to be important in the slow-flow regions [[Sarrami-Foroushani et al., 2017](#)]. In this thesis, we compared CFD simulations performed with Newtonian and the classic Casson [[Xiang et al., 2012](#)] model (non-Newtonian) in 5 large and giant cases in terms of the maximum RT and the minimum SR in the aneurysm sac. According to the results of Tukey's range test (details of the Tukey's range test results can be found in Chapter 3), both the absolute mean differences of RT and SR are smaller than the critical values. Therefore, the difference in means between Newtonian results and non-Newtonian results is not statistically significant ($\alpha = 0.05$), and the Newtonian assumption is applicable to this thesis.
- **Inlet flow velocity boundary conditions:** With in-vivo measurement-derived boundary conditions unavailable for our cohort, we used a previously developed Multivariate Gaussian Model (MGM) [[Sarrami-Foroushani et al., 2016](#)] to generate patient-specific boundary conditions as internal carotid

flow waveforms. The MGM model was trained and calibrated by the data from 17 healthy young adults [Ford et al., 2005]. A virtual population of 1000 normotensive waveforms was then generated while three of them, i.e., high, mean, and low, were selected to maximise the variability across the entire virtual population (by selecting high/low as the upper/lower bounds of the 1000 waveforms). To consider inter-subject variability, these three representative waveforms were used as inlet boundary conditions for flow simulations. Poiseuille’s law was used to scale the MGM-generated waveforms to achieve a time-averaged wall shear stress of 1.5 Pa at the inlet.

- Viscosity and density: Blood flow was regarded as an incompressible and Newtonian fluid with a constant density ρ of 1060 kg/m³ and viscosity μ of 0.004 Pa · s [Geers et al., 2014, Villa-Uriol et al., 2011].
- Outlet boundary conditions and the pragmatic assumption of rigid wall: We assumed the vessel wall was rigid [Humphrey and Taylor, 2008], and the no-slip wall boundary condition was imposed; a zero-pressure condition was prescribed at all outlets [Sarrami-Foroushani et al., 2019].
- Other CFD solver settings: The coupled Navier-Stokes equations and transport equations were solved in ANSYS CFX v19.3 (Ansys Inc., Canonsburg, PA, USA) using a finite volume method [Sarrami-Foroushani et al., 2019].

As mentioned above, we imposed the commonly used assumptions (e.g., rigid wall, Newtonian flow, and zero-pressure outlets) and parameters (blood viscosity and density values) from the literature. We also calibrated or validated each component of our framework in the previous work of our group: (1) The basic CFD solver setting (ANSYS CFX), blood viscosity/density, Newtonian assumption, rigid wall assumption, and zero-pressure outlets were imposed in our group’s previous study [Larrabide et al., 2012], where contrast time-density curves for in vitro and CFD data were generated and used to compare the in vitro experiments and CFD analysis for intracranial aneurysmal stenting. In vitro and CFD experiments were stated to be in agreement, especially for the quantitative comparison of the contrast density curves; (2) Digital segmentation of the vessel and aneurysm was from a previously published study [Lin et al., 2023]; (3) The internal carotid flow waveforms were generated from a cerebral autoregulation system (CARS) model originally proposed by Mader et al [Mader et al., 2015]. The details about how they extended this model to include the between/within-subjects variability

2.5 Improved CFD Workflow (Technical Contributions)

of the internal carotid flow waveforms can be found in our team’s previously published study [Lassila et al., 2020, Sarrami-Foroushani et al., 2016]; (4) The thrombosis model was originally developed by Sarrami-Foroushani et al. [2019]. They built computer models of the in vitro phantom experiments and compared computational simulations of the flow-diverter-induced thrombosis against in vitro observations reported by Gester et al. [2016]. Good agreement was achieved in that study.

2.5 Improved CFD Workflow (Technical Contributions)

2.5.1 Fully Automatic Volume Meshing and Post-Processing

As shown in Fig. 2.4, we obtained the patient-specific vascular surface model from segmentation. We used to manually generate the inlet and outlet surfaces, semi-automatically create a neck surface to separate the vessel and aneurysm domains, and semi-automatically generate the unstructured volumetric meshes using ANSYS ICEM CFD v19.3. During my PhD research, I developed several Python scripts to automate the volume meshing and post-processing components of our CFD workflow.

Inlet and Outlet Surfaces

The first step in generating unstructured volumetric meshes automatically, is to create the inlet and outlet surfaces. A Python module named “vedo” can be used for capping the vascular surface model to obtain the inlet and outlet surfaces. I created a Python script based on two main functions, ‘caps = vessel_surface.cap(return_cap=True)’ and ‘cap_surfaces = caps.split(maxdepth=40)’, from “vedo” to obtain the inlet and outlet surfaces automatically. Then I used ‘vedo.Mesh.area(surface_name)’ to calculate the area of each surface and set the surface with the largest area as the inlet while all other surfaces are used as outlets automatically. The function ‘vedo.mesh.Mesh.cap()’ generates a “cap” on a clipped mesh, or caps sharp edges, the function ‘vedo.mesh.Mesh.split()’ splits a mesh by connectivity, while the function ‘vedo.mesh.Mesh.area()’ computes the surface area of the mesh. More details about the above vedo functions can be found in ‘<https://vedo.embl.es/#gallery>’. The above scripts were tested on 109 aneurysm cases in the calibration study in Chapter 3.

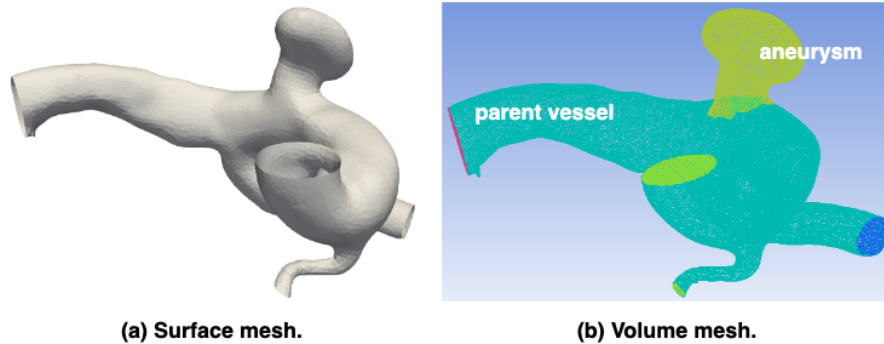


Figure 2.4: From segmentation, we acquired the patient-specific vascular surface model (a) that can be used to generate unstructured volumetric meshes (b) using ANSYS ICEM CFD v19.3 (Ansys Inc. Canonsburg, PA, USA). During volume meshing, a neck surface was used to separate the computational domain into parent vessel and aneurysm.

Neck Surface

The main aims of using a neck surface to separate the vessel and aneurysm domains for running simulations are as follows: (1) Since the thrombosis model is very time-consuming (usually taking days to weeks per case), we can constrain the biochemical reactions to occur only inside the aneurysm domain in ANSYS CFX to accelerate the simulations. (2) We can easily output, post-process, and analyse the haemodynamics and thrombus formation information inside the aneurysm, as we are more interested in information inside the aneurysm sac rather than the entire computational domain.

However, the neck surface may lead to poor volume meshing and thus incorrect simulation results (Fig. 2.5(a)). Although semi-automatically selecting some points along the mesh element edges for generating the neck surface can reduce the likelihood of poor volume meshing compared to using a plane for automatic cutting, we still need to manually pre-process the vascular surface model. Neck-surface-related issues persist even using the semi-automatic approach, with about 8.3% (10/121) cases having a problematic neck surface.

Suppose the neck surface is not generated along the mesh element edges to separate the vessel and aneurysm geometries. In that case, it might be identified as a wall surface (where blood flow can not pass through) rather than an internal wall (where blood flow can pass through), leading to incorrect simulation results Fig. 2.5(a). To avoid this issue, one approach is to use a single combined vessel and aneurysm surface

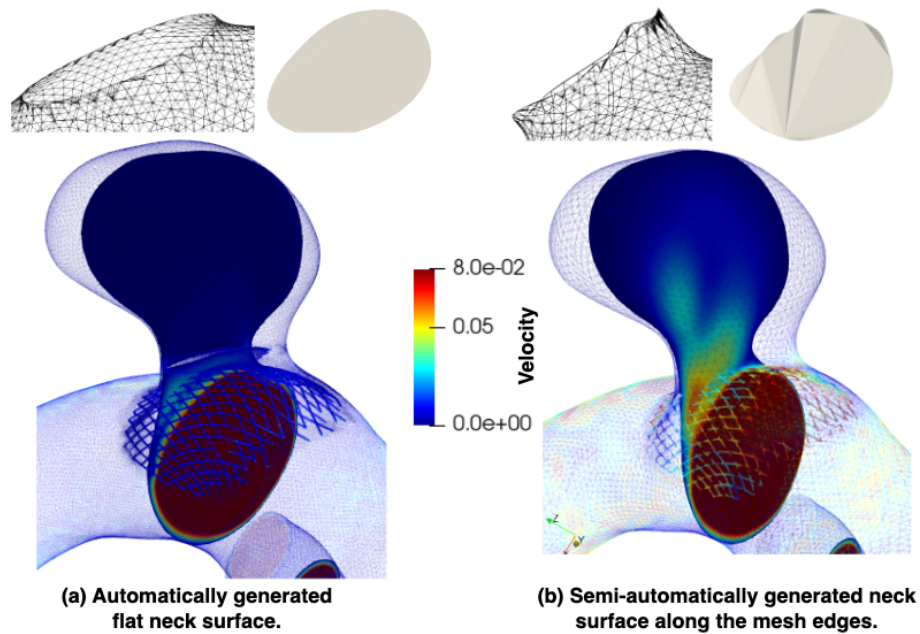


Figure 2.5: The neck surface can sometimes result in poor volume meshing outcomes, leading to incorrect simulation results. (a) If the aneurysm is cut out using a plane and then automatically capped to create a flat neck surface, this surface can sometimes be mistakenly identified as a wall during volume meshing. As a result, no blood flow (zero velocity inside the aneurysm) can be transported to the aneurysm sac. (b) If points along the mesh element edges are manually selected to separate the vessel from the aneurysm, and the neck surface is then semi-automatically generated using ANSYS ICEM, the neck surface is usually treated as an internal wall during volume meshing, allowing blood flow to pass through.

2.5 Improved CFD Workflow (Technical Contributions)

model to generate the volumetric meshes for simulations. Then, we can automatically extract haemodynamic and thrombus formation information inside the aneurysm sac during post-processing using a ‘vedo’ function. For example, the function “inside_aneurysm_points = aneurysm_mesh.inside_points(combined_vessel_and_aneurysm_mesh, invert=False, tol=1e-5, return_ids=True)” can be used to extract points within the aneurysm sac from the whole computational domain without relying on the neck surface.

The limitation of this approach is that we need to run the thrombosis model for the entire computational domain (both the parent vessel and aneurysm sac), which is time-consuming. To address this, another approach involves using a single combined vessel and aneurysm surface model to generate the entire volumetric meshes, then splitting the entire domain into vessel and aneurysm domains. Once all volume mesh elements are generated and named, for example, “VESSEL”, we can select the volumetric mesh elements inside the aneurysm and rename them as “ANEURYSM” in ANSYS ICEM. This process can be automated by calculating the minimum and maximum coordinates of the sac surface using Python (e.g., “min_sac_coordinates = [numpy.min(sac.x), numpy.min(sac.y), numpy.min(sac.z)]”) and creating the “ANEURYSM” domain using ICEM functions such as “ic_uns_create_selection_subset 0”, “ic_uns_subset_add_region uns_sel_0 {min_sac_coordinates max_sac_coordinates}”, and “ic_uns_set_part uns_sel_0 ANEURYSM”. All remaining unselected volume mesh elements will be assigned to the “VESSEL” domain by default.

In summary, I have proposed two automated methods to address the neck-surface-related issue described above. The first method involves extracting information within the aneurysm during post-processing, which has been tested on 42 cases in the calibration study presented in Chapter 3. The second method involves splitting the combined computational domain into “ANEURYSM” and “VESSEL” domains during volume meshing, which was tested on 5 cases and used in the sensitivity analysis and validation study in Chapter 4. Additionally, I created a Python script to generalise the ANSYS ICEM MACRO (.rpl file) for generating volume meshes across various scenarios, including different numbers of inlet and outlet surfaces, with or without neck surfaces, with or without the splitting of the combined vessel and aneurysm domain, and with or without coils and stent devices. Consequently, the volume meshing, simulation, and post-processing components of our workflow are now fully automated.

2.5.2 Improved Virtual Coiling for Wide-Neck Aneurysms

Clinically, when treating wide-neck aneurysms with flow-diverter stents and coils, clinicians typically insert the coils into the aneurysm sac first, followed by the deployment of the flow-diverter. The aneurysms are usually packed as densely as possible with coils. The flow diverter stabilises the coils within the aneurysm sac, ensuring there is no apparent gap or intersection between the stent and the coils.

In our CFD workflow, the virtual coiling and virtual stenting algorithms were developed independently. This may lead to two potential issues when treating wide-neck aneurysms with virtual coils and flow-diverters: (1) possible crossing or overlap between the virtual stent and coils, and (2) an unrealistic gap between the virtual stent and coils.

The virtual stenting process updates the stent mesh position based on the parent vessel geometry, with the deployed stent serving as a virtual reconstruction of the parent vessel, while the virtual coiling technique places coils one by one into an aneurysm geometry defined by its wall and ostium. Since these virtual treatment techniques were developed independently, the virtual treatment outcomes are closely related to the geometries used. Virtual coiling results depend on the aneurysm sac geometry, while the parent vessel geometry influences virtual stenting results. For wide-neck aneurysms, where there is often no distinct neck to separate the aneurysm sac from the parent vessel, this can result in intersections or unrealistic gaps between the stent and coils.

As illustrated in Fig. 2.6, the issues mentioned can be addressed by reconstructing a virtual vessel surface within the aneurysm geometry for use in the virtual coiling algorithm. The improved approach involves the following steps: (1) separate the aneurysm and vessel and virtually deploy the stent using the vessel geometry; (2) reconstruct a virtual vessel surface based on the stent (illustrated as the yellow surface in Fig. 2.6(b)); (3) extrude the edge of the virtual vessel surface to make contact with the aneurysm wall, then combine them to obtain a fully closed aneurysm geometry with the reconstructed vessel surface; and (4) open a small ostium on the reconstructed virtual vessel surface to insert the coils. This approach allows for the aneurysm sac to be packed densely with coils while avoiding intersections or unrealistic gaps between the stent and coils.

The improved virtual coiling strategy was employed in the patient-specific validation

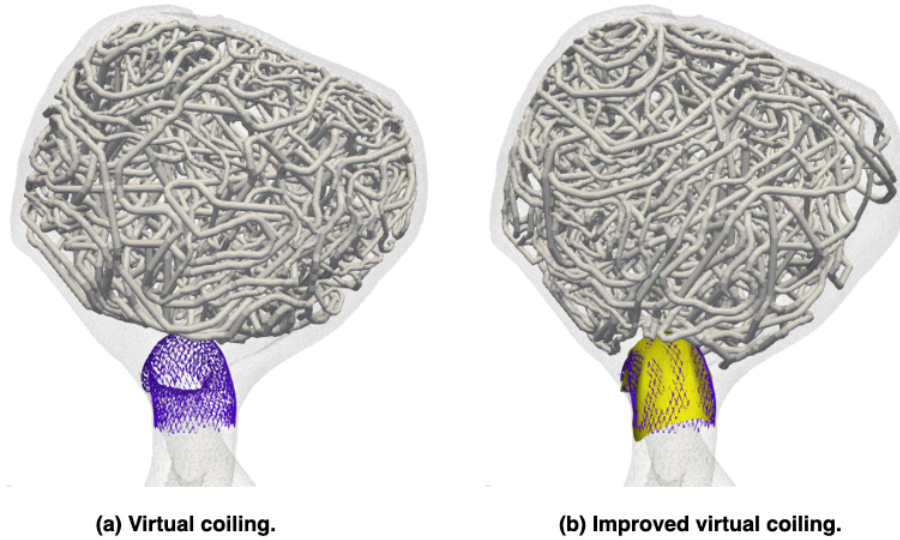


Figure 2.6: Improved virtual coiling for wide-neck aneurysms. (a) There are apparent gaps between the virtual coils and stent on the left and right side of the stent while the coils already contact with the top of the stent. (b) Improved virtual coiling to reduce gaps between the stent and coils and also avoid intersection.

case described in Chapter 4 (the sensitivity analysis and validation study paper), where we modelled the post-treatment haemodynamics and thrombus formation using patient-specific coils and flow-diverter stents.

2.5.3 Narrowing the Thrombosis Initiation to Areas Near the Wall

Sarrami-Foroushani et al. [2019] assumed that thrombosis initiates and progresses in regions where RT exceeds greater than a threshold (5 s) and SR falls below a specific threshold (25 s^{-1}). In Chapter 3, we calibrated these trigger thresholds based on clinical spontaneous thrombosis prevalence data, adjusting the RT threshold to 1.9 s and the SR threshold to 11 s^{-1} [Liu et al., 2023]. Furthermore, we enhanced the trigger mechanism to constrain thrombus initiation and progression to areas near the vessel wall or other thrombosed regions where the fibrin concentration, C_{fi} , is greater than 600 nM [Sarrami-Foroushani et al., 2019].

In untreated aneurysms, thrombi cannot remain suspended in the aneurysm lumen without anchors. It will be carried away by blood flow and either adhere to the vessel wall or be transported into the parent vessel. Given that we focus on saccular aneurysms

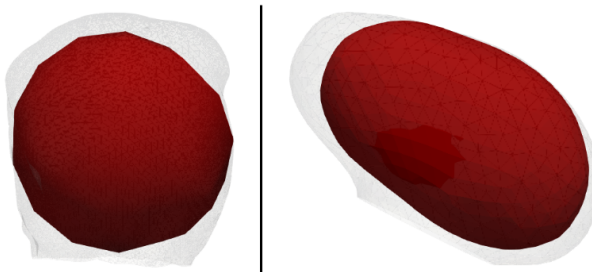


Figure 2.7: The aneurysms sac of saccular aneurysms can be approximated with a least square fit (or inscribed) ellipsoid or sphere.

in this thesis (which constitute 90% of IAs [Keedy, 2006]), and these aneurysms are typically spherical, the aneurysm sac can be approximated as a least-square fit ellipsoid or sphere [Piccinelli et al., 2012]. As illustrated in Fig. 2.7, we can separate aneurysm points into near-wall points and internal points using a virtual ellipsoid or sphere inside the aneurysm sac. The centre of the virtual ellipsoid or sphere is aligned with the centre of the least-square fit ellipsoid or sphere. The radius of the virtual ellipsoid or sphere is set to half of the radius of the least-square fit ellipsoid or sphere. We then use a Hill function to constrain thrombus initiation for all internal points. The Hill function is a sigmoidal activation function of form $\phi_p^{fi} = C_{fi}^n / (C_{fi}^n + C_{fi,50}^n)$, where the rate of occurrence of event, p , requires an appropriate concentration of fibrin, $C_{i,50}$ is the concentration of fibrin where the half-maximal activation (half saturation) occurs, and the Hill coefficient (the exponent n) reflects the steepness of the response curve. In this thesis, we set $C_{i,50} = 600$ nM and $n = 4$ in the trigger mechanism.

This thrombosis initiation narrowing strategy was employed in a patient-specific validation case in Chapter 4 (the sensitivity analysis and validation study paper), where we improved the accuracy of the thrombosis model predictions to better align with clinical realities prior to treatment.

CHAPTER 3

Haemodynamics of Thrombus Formation in
Intracranial Aneurysms: An in Silico
Observational Study

Abstract—How prevalent is spontaneous thrombosis in a population containing all sizes of intracranial aneurysms? How can we calibrate computational models of thrombosis based on published data? How does spontaneous thrombosis differ in normo- and hypertensive subjects? We address the first question through a thorough analysis of published data sets that provide spontaneous thrombosis rates across different aneurysm characteristics. This analysis provides data for a subgroup of the general population of aneurysms, namely those of large and giant size (>10 mm). Based on these observed spontaneous thrombosis rates, our computational modelling platform enables the first in silico observational study of spontaneous thrombosis prevalence across a broader set of aneurysms phenotypes. We generate 109 virtual patients and use a novel approach to calibrate two trigger thresholds: residence time and shear rate, thus addressing the second question. We then address the third question by utilizing this calibrated model to provide new insights into the effects of hypertension on spontaneous thrombosis.

We demonstrate how a mechanistic thrombosis model calibrated on an intracranial aneurysm cohort can help estimate spontaneous thrombosis prevalence in a broader aneurysm population. This study is enabled through a fully automatic multi-scale modelling workflow. We use the clinical spontaneous thrombosis data as an indirect population-level validation of a complex computational modelling framework. Furthermore, our framework allows exploration of the influence of hypertension in spontaneous thrombosis. This lays the foundation for in silico clinical trials of cerebrovascular devices in high-risk populations, e.g. assessing the performance of flow diverters in aneurysms for hypertensive patients.

3.1 Introduction

Spontaneous thrombosis (ST) of large and giant (>10 mm) unruptured intracranial aneurysms (IAs) is a common event that can be detected incidentally during advanced neuroradiological studies before treatment [Alberto et al., 2020, Cohen et al., 2007, Whittle et al., 1982]. These spontaneously thrombosed aneurysms are considered unstable dynamic structures that may grow, recanalise, bleed, compress, or cause thromboembolic events [Cohen et al., 2003, 2007, Whittle et al., 1982]. Partially spontaneously thrombosed aneurysms may serve as a source of emboli leading to ischemic attack [Brownlee et al., 1995, Whittle et al., 1982] or cerebral infarction [Alberto et al., 2020,

[Brownlee et al., 1995](#)]. Complete ST can sometimes stabilise the growth of the lesion, however, 33% (7/21) of the completely thrombosed aneurysms presented recanalisation at follow-up [[Alberto et al., 2020](#)].

Given this, it is worth asking, what is the precise prevalence of ST formation in IAs? In the literature, spontaneous intra-aneurysmal thrombosis is reported as a common phenomenon, and the ST prevalence reported in different studies varies widely. The ST prevalence rate of pediatric patients (8.3%-16.9%) is higher than in adults [[Lasjaunias et al., 2005](#), [Liang et al., 2009](#)], while female patients are more likely to present with ST than male patients [[Alberto et al., 2020](#)]. Similarly, differences are observed depending on the aneurysms themselves, with ST in small aneurysms (≤ 10 mm) a much rarer phenomenon [[Alberto et al., 2020](#), [Ohta et al., 2001](#)] than the approximately 50% prevalence rate in giant IAs (≥ 25 mm) [[Schubiger et al., 1980](#), [Whittle et al., 1982](#)]. Despite the statistics, the prevalence of ST on a population level is not well-understood, as most studies had small sample sizes. We collect the clinically-reported prevalence rates of ST (partial or complete) in IAs without treatment in the literature and conduct a statistical analysis to identify the prevalence rate of ST across different patient demographics and aneurysm characteristics.

Experimental studies have highlighted the importance of haemodynamic factors in the growth and rupture of aneurysms [[Artmann et al., 1984](#), [Meng et al., 2014](#)]. CFD models use high RT and low SR to describe the thrombosis initiation. However, there is no consensus on the trigger thresholds, with different values used throughout the literature [[de Sousa et al., 2016](#), [Gorring et al., 2015](#), [Hathcock, 2006](#), [Rayz et al., 2010](#), [Sarrami-Foroushani et al., 2019](#)]. Therefore, there is a need to calibrate RT and SR thresholds for use in thrombosis models [[Sarrami-Foroushani et al., 2019](#)]. In this study, we create, for the first time, an automatic computational workflow that enables population-level in silico studies to calibrate haemodynamic thresholds (RT and SR) of thrombus formation against real population-specific data.

Finally, we use our calibrated thrombosis model to study the effect of hypertension on ST. Hypertension is a well-known risk factor of unruptured IAs [[Vlak et al., 2013](#)] and more than 75% of saccular IA patients have hypertension [[Kotikoski et al., 2018](#)]. The flow diverter performance assessment (FD-PASS) in silico trial showed that hypertension may cause less effective flow diversion [[Sarrami-Foroushani et al., 2021](#)], while the IntrePED study reported an association between hypertension and ischaemic

stroke in flow-diverted aneurysms [Brinjikji et al., 2016]. We modelled hypertension as boundary conditions modulated by a cerebral autoregulation system (CARS) model [Lassila et al., 2020] originally proposed by Mader et al. [2015].

This study aims to first establish the prevalence of ST in IAs with different characteristics and different demographics. We then calibrate the haemodynamic thresholds (RT and SR) of thrombus formation by matching our numerical ST prevalence to the real clinical data. Finally, we use our calibrated thrombosis model to investigate the differences in the ST prevalence and aneurysmal haemodynamic factors (RT and SR) in normotensive and hypertensive patients. The novelty of this study is that we create, for the first time, a fully automatic multi-scale modelling workflow that enables population-based *in silico* studies to calibrate haemodynamic thresholds (RT and SR) of thrombus formation against real population-specific data. We demonstrate how a mechanistic thrombosis model calibrated on an IA cohort (large and giant IAs only) can help estimate ST prevalence in a broader aneurysm population (all sizes included). In addition, our framework can provide new insights into the impact of hypertension on thrombosis by modelling hypertension as boundary conditions modulated by a CARS model [Lassila et al., 2020].

3.2 Materials and Methods

Through a thorough analysis of published data sets that provided ST rates for a subgroup of the general population of aneurysms, namely those of large and giant aneurysms (>10 mm), we estimated the clinical ST prevalence of large and giant IAs for our simulation cohort. Using the clinical ST prevalence rate, we performed an *in silico* observational study in 109 virtual patients to calibrate RT and SR thresholds and estimate ST prevalence in a broader IA population. We further investigated how ST differs in normo- and hypertensive conditions. The haemodynamic factors were calculated using an automatic workflow (Fig. 3.1). While each component of our methodological framework has been independently developed and validated before, this study is the first to model and present such a complex process on the largest patient cohort to date.

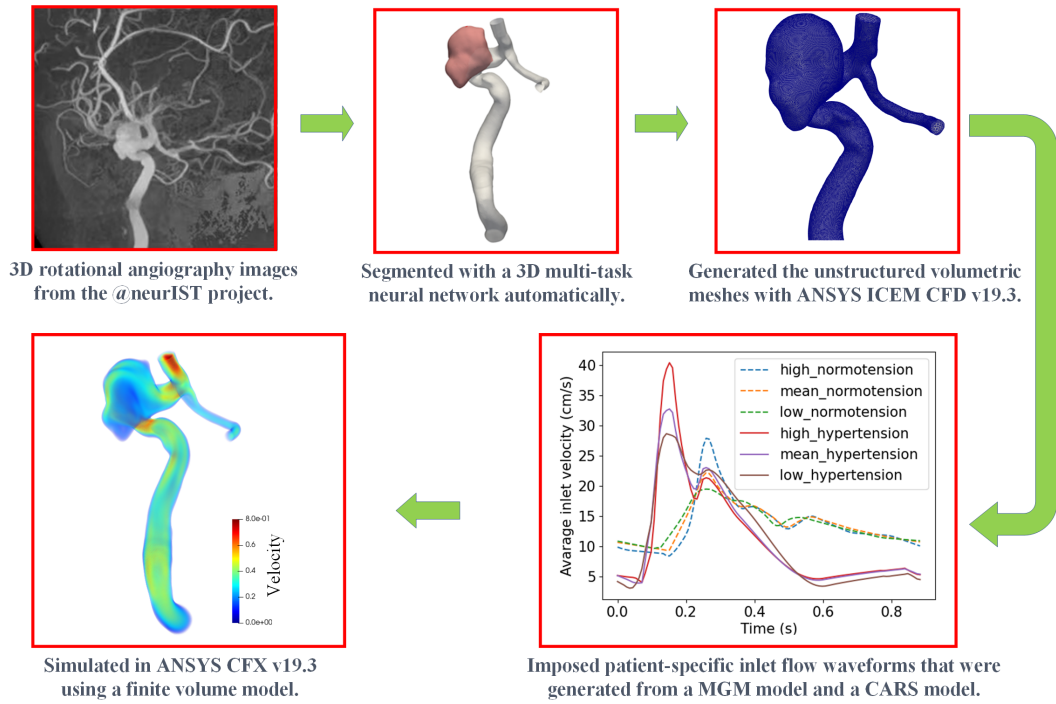


Figure 3.1: Automatic workflow on MULTI-X. The images were from the @neurIST project [Iavindrasana et al., 2008, Villa-Uriol et al., 2011]. We applied a multi-tasking neural network to automatically segment these images [Lin et al., 2023] and generate the corresponding patient-specific vascular surface models, and then we used ANSYS ICEM CFD v19.3 (Ansys Inc. Canonsburg, PA, USA) to generate unstructured volumetric meshes. The patient-specific inlet flow waveforms were generated from a Multivariate Gaussian Model (MGM) [Sarrami-Foroushani et al., 2016] and a CARS model [Lassila et al., 2020]. Finally, the coupled Navier-Stokes equations and transport equation for RT were solved in ANSYS CFX v19.3 (Ansys Inc., Canonsburg, PA, USA) using a finite volume method [Sarrami-Foroushani et al., 2019].

3.2.1 Systematic Literature Review

To estimate the ST prevalence for different aneurysm characteristics, a comprehensive and systematic review of the literature up to July 2021 was conducted on the MEDLINE database. We searched for articles reporting cohort cases of IA ST (partial or complete). The articles were identified using Boolean searches on PubMed with the following keywords “((spontaneous thrombosis) or (spontaneous clot formation)) and ((intracranial aneurysms) or (cerebral aneurysms))”. The search strategy followed the PRISMA (Preferred reporting items for systematic review and meta-analysis protocols) guidelines [Shamseer et al., 2015]. Case report articles were not considered. Only articles in English were considered and only those reporting patient cohorts. Aneurysms were divided into three groups: small (≤ 10 mm), large (>10 mm and <25 mm), and giant (≥ 25 mm) according to the sizes reported by the investigators.

After the systematic literature review, we were able to estimate the ST prevalence of aneurysms of different sizes. For a population, the ST prevalence (P) is given by

$$P = \frac{N_s P_s + N_l P_l + N_g P_g}{N_s + N_l + N_g} \times 100\%, \quad (3.1)$$

where N_s , N_l , and N_g are the numbers of small, large, and giant IAs, respectively. P_s , P_l , and P_g are the ST prevalence of small, large, and giant IAs, respectively. However, ST is rarely reported in small IAs, so we used the collected ST prevalence of only large and giant IAs, P_l and P_g , to estimate the clinical ST prevalence for our cohort according to its distribution of large and giant cases. We calibrated our clotting model by matching the numerical ST prevalence to the estimated clinical ST prevalence for our simulation cohort. After calibration, we used the calibrated model to predict the ST prevalence for small aneurysms, P_s . Finally, the ST prevalence for a broader general population can be estimated by equation (3.1).

3.2.2 In Silico Observational Study

Patient and Aneurysm Characteristics

The patient image data in this paper were from the @neurIST project [Iavindrasana et al., 2008, Villa-Uriol et al., 2011]. All images were anonymised, respecting the @neurIST ethical approval for the use of patient data (<http://www.aneurist.org>). We only considered single aneurysm cases. 109 patient datasets (72 female, 37 male), with 67

small, 40 large, and 2 giant IAs, were available. Among the 109 cases, 67 small, 21 large, and 1 giant case were segmented automatically, while the other 19 large and 1 giant case were manually segmented in the @neurIST project. The details of the population characteristics of our simulation cohort can be found in Table 3.1, the average age of our simulation cohort is 51 years (range 22-78 years) and the mean aneurysm neck size is 5.0 ± 2.1 mm (range 1.7 - 12.3 mm). Of these 109 IAs, 61%(67/109) are small IAs, 37%(40/109) are large IAs, and 2%(2/109) are giant IAs. It is well-established in the literature that aneurysm size is the most important factor associated with ST [Alberto et al., 2020, Ohta et al., 2001, Scerrati et al., 2019]. The distribution of aneurysm sizes in our simulation cohort is quite similar to that of the general population obtained from a large consecutive series of 1993 ruptured IAs [Korja et al., 2016]: 68%(1355/1993) small IAs, 30%(598/1993) large IAs, and 2%(40/1993) giant IAs. Thus, the size-based ST prevalence calculated by our calibrated model can be applied to the general population.

Flow Simulations

For our *in silico* observational study of ST, RT was modelled as a tracer passively transported with the blood flow by solving equation (2.2) described in Chapter 2. SR was calculated automatically by using an associated built-in variable in ANSYS CFX [Sarrami-Foroushani et al., 2019].

In the literature, blood rheology was often assumed to be Newtonian, but non-Newtonian effects were suggested to be important in the slow-flow regions [Sarrami-Foroushani et al., 2017]. In this study, we compared CFD simulations performed with Newtonian and the classic Casson [Xiang et al., 2012] model (non-Newtonian) in 5 large and giant cases in terms of the maximum RT and the minimum SR in the aneurysm sac (Table 3.2). According to the results of Tukey’s range test, both the absolute mean difference of RT and SR are smaller than the critical values, thus the difference in means between Newtonian results and non-Newtonian results is not statistically significant ($\alpha = 0.05$). In addition, when using the calibrated RT and SR thresholds, 1.9 s and 11 s^{-1} , the numerical thrombosis status predicted by the Newtonian model and the non-Newtonian model is the same in all 5 cases. Therefore, the Newtonian assumption is applicable to this study.

For a given case, if RT is greater than the RT threshold and SR is less than the

Table 3.1: Population Characteristics.

<i>Number of aneurysms</i>	109
<i>Age, year</i>	
Mean \pm SD (N)	51.4 \pm 6.4 (109)
Median	51.0
Range	22.0-78.0
Female sex, % (n/N)	66.1 (72/109)
<i>Aneurysm size, mm</i>	
Mean \pm SD (N)	9.2 \pm 4.7 (109)
Median	7.9
Range	2.5-30.9
Small ($d \leq 10$ mm), % (n/N)	61 (67/109)
Large (10 mm $< d < 25$ mm), % (n/N)	37 (40/109)
Giant ($d \geq 25$ mm), % (n/N)	2 (2/109)
<i>Aneurysm neck, mm</i>	
Mean \pm SD (N)	5.0 \pm 2.1 (109)
Median	4.4
Range	1.7-12.3
<i>Aneurysm location</i>	
ICA/PComA, % (n/N)	62.4 (68/109)
MCA, % (n/N)	21.1 (23/109)
BA/PCA/SCA, % (n/N)	11.9 (13/109)
ACA, % (n/N)	4.6 (5/109)

ICA, internal carotid artery; PComA, posterior communicating artery; MCA, middle cerebral artery; BA, basilar artery; PCA, posterior cerebral artery; SCA, superior cerebellar artery; ACA, anterior cerebral artery.

3.2 Materials and Methods

Table 3.2: The maximum RT and minimum SR assuming Newtonian and non-Newtonian blood flows.

Cases	RT(s)		SR(s ⁻¹)	
	Newtonian	non-Newtonian	Newtonian	non-Newtonian
The max RT case	2.84	2.52	0.004	0.001
The median RT case	2.39	2.72	9.18	1.79
The median SR case	1.10	1.63	13.31	9.07
The median non-sphericity case	2.47	2.49	4.21	1.39
The min non-sphericity case	2.35	2.40	24.57	23.50
Mean	2.230	2.352	10.255	7.150
Variance	0.349	0.141	71.407	76.805
Tukey's range test				
		3.261		3.261
	$q(2,8,\alpha=0.05)$			
	$T = q \times \sqrt{\frac{MSE}{n}}$	0.722		12.555
	Absolute mean difference	0.122(<0.721)		3.105(<12.555)
	Significant difference at $\alpha = 0.05$	No		No

The max RT cases is also the min SR case; the median RT case is also the max non-sphericity case; MSE, mean square error; n, the number of items in one sample.

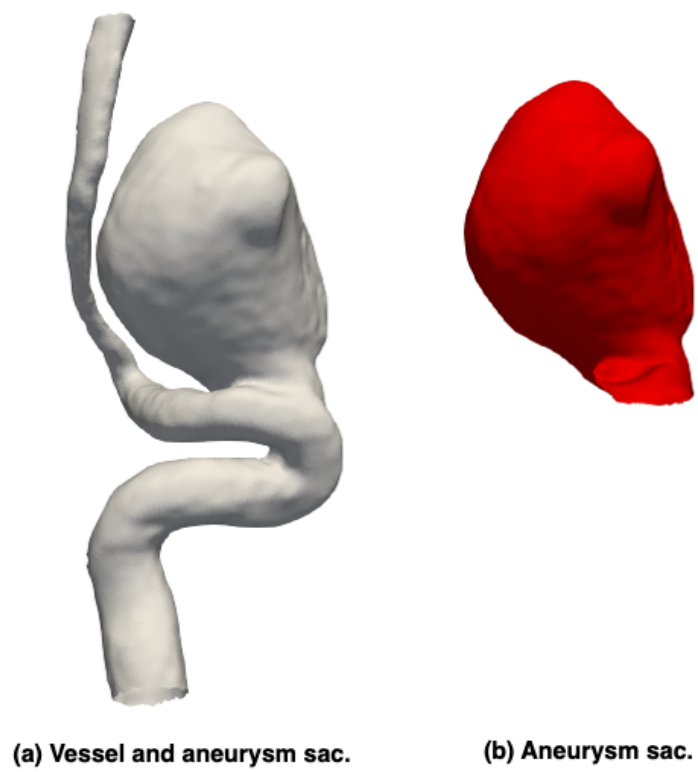


Figure 3.2: Segment the aneurysm sac alone and then extract the RT and SR information inside the aneurysm sac during post-processing.

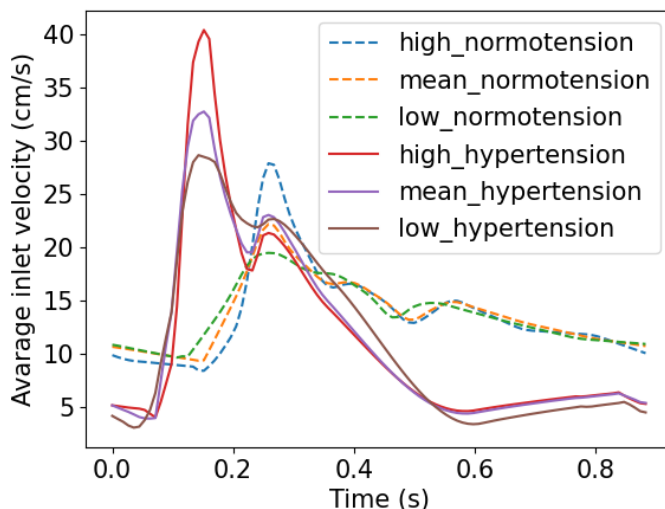


Figure 3.3: Patient-specific inlet flow waveforms.

SR threshold in the aneurysm sac, thrombus formation is assumed to initiate. We performed a series of unsteady simulations using the generated volumetric meshes and calculated the magnitude and distribution of RT and SR on the whole computational domain (both the vessel and the aneurysm sac) and on the isolated aneurysm sac for each case (Fig. 3.2). By varying the values of the RT and SR thresholds, we obtained different numerical ST prevalence across our cohort of large and giant IAs. Finally, by matching the simulated ST prevalence in our large and giant IA cohort to the clinical ST prevalence, we were able to obtain a plausible range of trigger threshold values for RT and SR and calibrate our model.

Patient-Specific Inlet Flow Boundary Conditions

According to the latest definition of hypertension from the American College of Cardiology/American Heart Association (ACC/AHA) in November 2017 [Yancy et al., 2017], participants are considered hypertensive if they have a measured systolic blood pressure $SBP \geq 130$ mmHg or a measured diastolic blood pressure $DBP \geq 80$ mmHg. We use a computational model of cerebral autoregulation [Lassila et al., 2020] originally proposed by Mader et al. [2015] to model the effect of hypertension on IA haemodynamics. The CARS model takes the normotensive blood flow waveforms calculated for each virtual case (the generation of the normotensive inflow waveforms can be found in

Chapter 2), estimates the corresponding normotensive pressure waveforms (SBP: 90-120 mmHg, DBP: 70-80 mmHg, heart rate: 68 bpm), scales the normotensive pressure waveforms to hypertensive waveforms (fixed scale factor 1.3 of SBP and DBP [Lassila et al., 2020, Ogoh et al., 2005], 68 bpm), and finally generates the associated hypertensive waveforms. Fig. 3.3 shows the inlet flow waveforms for a 51-year-old female.

3.3 Results

3.3.1 Clinical ST prevalence

According to our search strategy, 434 studies were initially identified; after removing duplicates and case reports, 185 articles remained. 152 were excluded by title or abstract reading, while 33 underwent further detailed review for eligibility. A total of 11 studies were finally included in the statistical analysis.

The details of the collected cohort data of ST in large and giant aneurysms are shown in Table 3.3 and Table 3.4. In Table 3.5, we present the summary of all ST prevalence calculated from the results of our literature review. There are 646 IAs in total. The distribution of aneurysm sizes in these 646 IAs are as follows: 68%(437/646) small, 4%(29/646) large, and 28%(180/646) giant IAs. Of the 29 large IAs, 7 cases presented with ST. Therefore, the ST prevalence (partial or complete) for large IAs is 24.1%(7/29) \pm 7.9%, with 90% confidence. Of the 180 giant IAs, 97 cases were thrombosed. Therefore, the ST prevalence (partial and complete) for giant IAs is 53.9%(97/180) \pm 6.1%, with 90% confidence.

For our simulation cohort with 40 large and 2 giant cases, according to equation (3.1), we estimated the ST prevalence rate as 25.5%. We used this as a criterion to calibrate the RT and SR threshold parameters.

3.3.2 Numerical Results of RT and SR

The maximum RT and minimum SR in the aneurysm sac at mean flow normotensive conditions for all 42 large and giant cases are shown in Table 3.6. For a given pair of RT and SR thresholds, we obtained a specific numerical ST prevalence for large and giant IAs. We plotted all combinations of RT and SR threshold values that can make the simulated ST prevalence close (within $\pm 5\%$) to the clinical ST prevalence of 25.5% (Fig. 3.4). The overlap of these parameters at high, mean, and low is considered to

Table 3.3: ST prevalence of large aneurysms (large IAs only).

	cohort1	cohort2	summary
Number of large IAs	14	15	29
Age, year			
Mean	52	44	47
Range	15-76	6-81	6-81
Aneurysm size, mm			
Mean \pm SD (N)	14.3 \pm 3.6 (14)	-	-
Median	13.9	-	-
Range	10.0-20.5	-	-
Aneurysm location			
ICA/PComA, % (n/N)	42.8 (6/14)	93.3 (14/15)	69.0 (20/29)
MCA, % (n/N)	28.6 (4/14)	0	13.8 (4/29)
BA, % (n/N)	21.4 (3/14)	6.7 (1/15)	13.8 (4/29)
Other, % (n/N)	7.1 (1/14)	0	3.4 (1/29)
ST IAs	5	2	7
ST prevalence			24.1% \pm 7.9% (7/29)

ST, spontaneous thrombosis; The cohort1 data were from [Baumgartner et al. \[1994\]](#) and the cohort2 data were from [Saatci et al. \[2003\]](#).

3.3 Results

Table 3.4: ST prevalence of giant aneurysms (giant IAs only).

	cohort1	cohort2	cohort3	cohort4	cohort5	summary
Number of giant IAs	1	18	10	22	129	180
Age, year						
Mean	52	44	45	49	68	55
Range	15-76	6-81	14-70	21-66	5-85	5-85
Aneurysm size, mm						
Mean \pm SD (N)	25.3 \pm 0 (1)	-	36.0 \pm 7.0 (10)	-	-	-
Median	25.3	-	33.5	-	-	-
Range	25.3-25.3	-	27-50	-	-	-
Aneurysm location						
ICA/PComA, % (n/N)	100.0 (1/1)	94.4 (17/18)	60.0 (6/10)	31.8 (7/22)	38.8 (50/129)	45.0 (81/180)
MCA, % (n/N)	0	0	20.0 (2/10)	45.5 (10/22)	31.8 (41/129)	29.4 (53/180)
BA, % (n/N)	0	0	20.0 (2/10)	18.2 (4/22)	24.8 (32/129)	21.1 (38/180)
Other, % (n/N)	0	5.6 (1/18)	0	4.5 (1/22)	4.6 (6/129)	4.5 (8/180)
ST IAs	0	9	6	12	70	97
ST prevalence						53.9% \pm 6.1% (97/180)

The cohort1 data were from [Baumgartner et al. \[1994\]](#), the cohort2 data were from [Saatci et al. \[2003\]](#), the cohort3 data were from [Schubiger et al. \[1980\]](#), the cohort4 data were from [Whittle et al. \[1982\]](#) and the cohort5 data were from [Nurminen et al. \[2014\]](#).

Table 3.5: Summary of the literature ST prevalence.

Characteristics	ST prevalence	References
Giant (≥ 25 mm)	53.9%(97/180) \pm 6.1%	Schubiger et al. [1980] ; Whittle et al. [1982] ; Baumgartner et al. [1994] ; Nurminen et al. [2014] ; Saatci et al. [2003]
Large (>10 mm and <25 mm)	24.1%(7/29) \pm 7.9%	Baumgartner et al. [1994] ; Saatci et al. [2003]
Small (≤ 10 mm)	Rarely reported	Alberto et al. [2020] ; Ohta et al. [2001] ; Scerrati et al. [2019]
ICA (giant)	42.1%(32/76) \pm 9.3%	Schubiger et al. [1980] ; Whittle et al. [1982] ; Baumgartner et al. [1994] ; Nurminen et al. [2014] ; Saatci et al. [2003] ; Pierot et al. [2012]
MCA (giant)	62.3%(33/53) \pm 11.0%	Schubiger et al. [1980] ; Whittle et al. [1982] ; Nurminen et al. [2014]
BA (giant)	63.2%(24/38) \pm 12.9%	Schubiger et al. [1980] ; Whittle et al. [1982] ; Nurminen et al. [2014]
Sex	Slight female prevalence	Alberto et al. [2020]
Age (<15 years)	8.3% – 16.9%	Lasjaunias et al. [2005] ; Liang et al. [2009]

ICA, internal carotid artery; MCA, middle cerebral artery; BA, basilar artery.

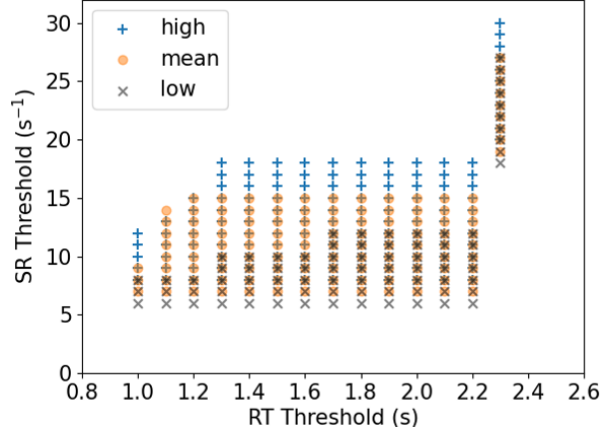


Figure 3.4: For a given case, thrombus formation in the aneurysm sac is assumed to initiate when the RT exceeds the RT threshold and the SR is below the SR threshold. We systematically explored all possible combinations of RT (ranging from 0 s to 5 s with 0.1 s increments) and SR (ranging from 0 s⁻¹ to 50 s⁻¹ with 1 s⁻¹ increments). Scatter plots were then generated to visualise the RT-SR parameter combinations where the numerical ST prevalence aligned with the clinical ST prevalence (25.5%) observed in large and giant aneurysms, with a 5% tolerance. For three different inflow waveforms (high, mean, and low waveforms), different RT and SR combinations were obtained. The plausible threshold values for thrombus formation are those located within the overlap area, as this region indicates where the thresholds are largely independent of inter-subject flow variability.

be the plausible range of thresholds since it indicates where the thresholds are largely independent of the inter-subject flow variability. We have 42 large and giant cases in total, and an increase or decrease of one thrombosed case increases or decreases the ST prevalence by 2.4%. In Fig. 3.4, we set a 5% tolerance for the numerical ST prevalence (tolerance for 2 cases), so the threshold values in the overlap region in Fig. 3.4 make the numerical ST prevalence between 20.5-30.5%. For the overlap area in Fig. 3.4, the RT and SR thresholds are in the ranges [1.0, 2.3] s and [8, 27] s⁻¹, respectively. The average value of RT and SR in the overlap area are 1.9 s and 11 s⁻¹, respectively.

When using the average value of RT and SR thresholds, i.e., 1.9 s and 11 s⁻¹, the numerical ST prevalence of large and giant IAs for our cohort is 28.6%(12/42) ± 11.5%, while the numerical ST prevalence of small IAs for our cohort is 17.9%(12/67) ± 7.7%. We estimated the ST prevalence of large IAs (24.1% ± 7.9%) and giant IAs (53.9% ± 6.1%) from the literature data and we obtained the ST prevalence of small IAs (17.9% ± 7.7%) from our observational study. The distribution of aneurysm sizes in a general population with 1993 IAs [Korja et al., 2016] is: 68% (1355/1993) small IAs, 30% (598/1993) large IAs, and 2% (40/1993) giant IAs. Therefore, the ST prevalence of the

3.3 Results

Table 3.6: Numerical results of Max RT and Min SR in the aneurysm sac for large and giant IAs.

Case	Max RT (s)	Min SR (s^{-1})	Size (mm)	Age (years)	Sex	Location
Mean \pm SD	2.02 \pm 0.67	20.31 \pm 16.84	13.80 \pm 4.40	51.6 \pm 5.7	-	-
Median	2.38	15.31	11.70	51	-	-
Range	0.48-2.84	0.004-76.59	10.14-30.92	43-75	-	-
1	1.56	13.05	11.39	51	F	MCA
2	2.16	8.46	13.20	52	F	MCA
3	2.48	2.71	17.87	51	F	BA
4	2.31	6.02	17.28	66	M	BA
5	0.50	42.08	15.92	48	M	PCoMA
6	2.47	14.31	20.63	51	F	ICA
7	1.10	13.31	15.23	51	F	PCoMA
8	2.47	4.21	10.60	50	M	MCA
9	2.84	0.004	11.10	43	F	BA
10	0.50	19.30	10.20	54	M	ICA
11	1.59	40.19	11.70	51	F	PCoMA
12	2.39	9.18	10.43	51	F	PCoMA
13	2.29	18.74	25.50	52	M	ICA
14	0.86	29.52	10.45	44	F	ICA
15	1.63	30.82	10.90	51	M	PCoMA
16	2.43	6.21	20.20	54	F	BA
17	1.89	21.53	11.47	44	M	MCA
18	2.37	12.51	10.20	52	F	ICA
19	0.48	69.34	16.00	51	F	PCoMA
20	1.32	32.72	11.81	51	F	ICA
21	1.77	30.64	11.20	43	F	PCoMA
22	2.43	11.27	12.75	48	F	BA
23	2.57	8.55	15.07	51	F	ICA
24	2.68	5.13	19.78	51	F	ICA
25	2.47	9.46	12.59	66	F	ICA
26	2.45	8.67	11.67	46	M	MCA
27	2.48	16.31	10.14	51	M	MCA
28	2.34	34.37	10.31	75	F	MCA
29	2.23	20.91	11.06	51	F	ICA
30	2.50	10.85	10.49	51	M	SCA
31	2.60	29.66	11.52	51	M	ICA
32	2.45	35.68	13.93	51	F	ICA
33	2.42	17.63	16.70	51	F	ICA
34	0.99	76.59	10.32	51	M	ICA
35	2.49	38.04	10.80	51	F	PCoMA
36	1.69	36.39	16.02	51	F	PCoMA
37	2.35	24.57	11.18	51	M	PCoMA
38	2.44	3.73	30.92	51	F	BA
39	2.39	7.47	15.69	51	F	PCoMA
40	0.59	29.80	12.61	51	F	ICA
41	2.52	0.05	11.10	51	F	PCA
42	2.52	3.17	11.71	58	M	ACA

Table 3.7: Comparison between thrombosed and non-thrombosed aneurysms.

	ST large/-giant	Non-ST large/-giant	p value	ST small	Non-ST small	p value
Number of IAs	12	30		12	55	
Age (year)	51.9 ± 5.7	51.5 ± 5.8	0.83	50.5 ± 3.3	51.4 ± 7.5	0.55
Female,%(n/N)	58.3%(7/12)	66.7%(20/30)	0.35	66.7%(8/12)	72.7%(40/55)	0.84
Size (mm)	15.6 ± 6.1	13.1 ± 3.5	0.19	6.9 ± 1.0	6.1 ± 1.8	0.09
Neck width (mm)	6.3 ± 2.6	6.9 ± 2.1	0.49	3.4 ± 0.6	4.0 ± 1.1	0.01
Aspect ratio	1.9 ± 0.4	1.6 ± 0.7	0.05	1.7 ± 0.4	1.1 ± 0.5	8.2e-4
Non-sphericity	0.26 ± 0.05	0.19 ± 0.06	4.5e-4	0.26 ± 0.03	0.16 ± 0.06	1.7e-4
Max RT (s)	2.51 ± 0.14	1.83 ± 0.72	2.1e-5	2.46 ± 0.20	0.73 ± 0.60	4.1e-24
Min SR (s^{-1})	4.80 ± 3.10	26.52 ± 16.36	5.2e-8	3.23 ± 2.76	81.30 ± 102.52	8.0e-7
Aneurysm location						
ICA/PComA, % (n/N)	25.0 (3/12)	76.7 (23/30)		66.7 (8/12)	61.8 (34/55)	
MCA/Sylvian, % (n/N)	16.7 (2/12)	16.7 (5/30)		16.7 (2/12)	25.4 (14/55)	
BA/PCA/SCA, % (n/N)	50.0 (6/12)	6.6 (2/30)		8.3 (1/12)	7.3 (4/55)	
ACA, % (n/N)	8.3 (1/12)	0 (0/30)		8.3 (1/12)	5.5 (3/55)	
p values were computed using the two-tailed t-test.						

ICA, internal carotid artery; PComA, posterior communicating artery; MCA, middle cerebral artery; BA, basilar artery; PCA, posterior cerebral artery; SCA, superior cerebellar artery; ACA, anterior cerebral artery.

general population containing all sizes of intracranial aneurysms can be estimated by equation (3.1) as $20.5\%(408/1993) \pm 1.5\%$.

Our simulation results show that bigger aneurysms are more likely to be thrombosed, which is consistent with the literature data [Alberto et al., 2020, Lawton et al., 2005, Ohta et al., 2001, Scerrati et al., 2019]. No exact ST prevalence for small IAs is reported in the literature. From a hemodynamics point of view, our study found that the numerical ST prevalence for small IAs of our cohort is 17.9%. Those thrombosed small IAs have a significantly higher aspect ratio (AR), measured as aneurysm height-to-neck width, than the non-thrombosed small IAs (Table 4.5).

To investigate why bigger aneurysms are more likely to present with ST, we compared the demographics and aneurysm characteristics for thrombosed large and giant IAs, non-thrombosed large and giant IAs, thrombosed small IAs, and non-thrombosed small IAs (Table 4.5). The above grouping for all 109 cases is based on the model-predicted ST status. These four groups are very similar in terms of patient age and

sex, but the size and AR of the thrombosed groups are larger than that of the non-thrombosed groups. 62.5% (15/24) of the thrombosed group are high AR (>1.6) [Sarrami-Foroushani et al., 2021] IAs. In contrast, high AR cases only account for 24.7% (21/85) of the non-thrombosed group. In our cohort, bigger aneurysms are also more likely to be high AR cases, with 59.5% (25/42) of the large and giant IAs having a high AR, while only 16.4% (11/67) of the small IAs have a high AR. The thrombosed groups, including both large/giant and small IAs, have a significantly higher AR and non-sphericity than the non-thrombosed groups. Our results show that IAs with higher AR and non-sphericity are more likely to be thrombosed and bigger aneurysms usually have a higher AR.

We also analysed the relationships between aneurysm geometry characteristics and the two haemodynamic factors, RT and SR, for all 109 cases. As shown in Fig. 3.5, correlation between size and RT/SR is weaker than between AR and RT/SR, and the maximum RT increases with AR. The minimum SR in the aneurysm sac decreases with both size and AR.

3.3.3 The Effect of Hypertension on the ST Prevalence

We imposed hypertensive inlet waveforms to investigate how hypertension affects the ST prevalence in large and giant IAs. Our numerical results show that the ST prevalence of large and giant IAs of our cohort at hypertension is 23.8%, which is lower than at normotension (28.6%). To investigate why ST might be less common in hypertensive patients, we compared normotension and hypertension in terms of the maximum RT and minimum SR in the aneurysm sac for all 42 large and giant IAs (Fig. 3.6). No significant differences are observed in the maximum RT calculated under normotensive and hypertensive conditions ($p = 0.5928$). However, 90.5% (38/42) of cases in hypertension have a higher minimum SR than in normotension ($p = 0.0007$). This explains why flow stasis-induced computational models show a relatively lower ST prevalence in hypertensive patients.

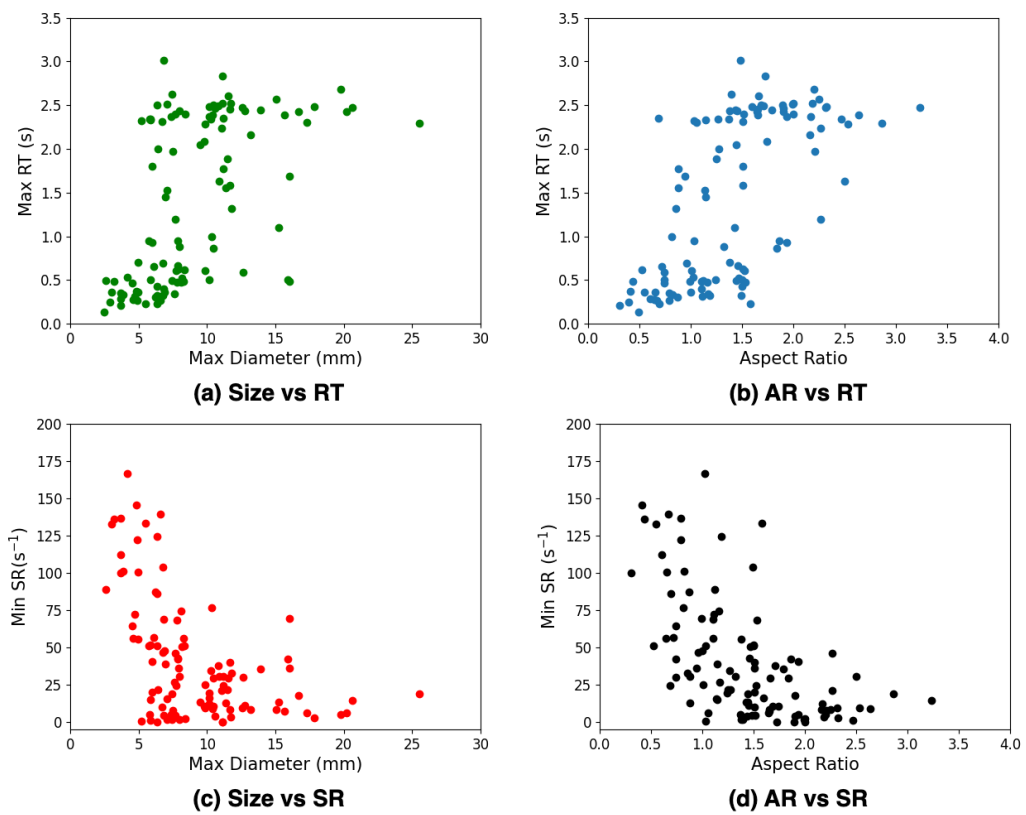


Figure 3.5: Relationships between aneurysm geometry characteristics and RT/SR for the whole simulation cohort.

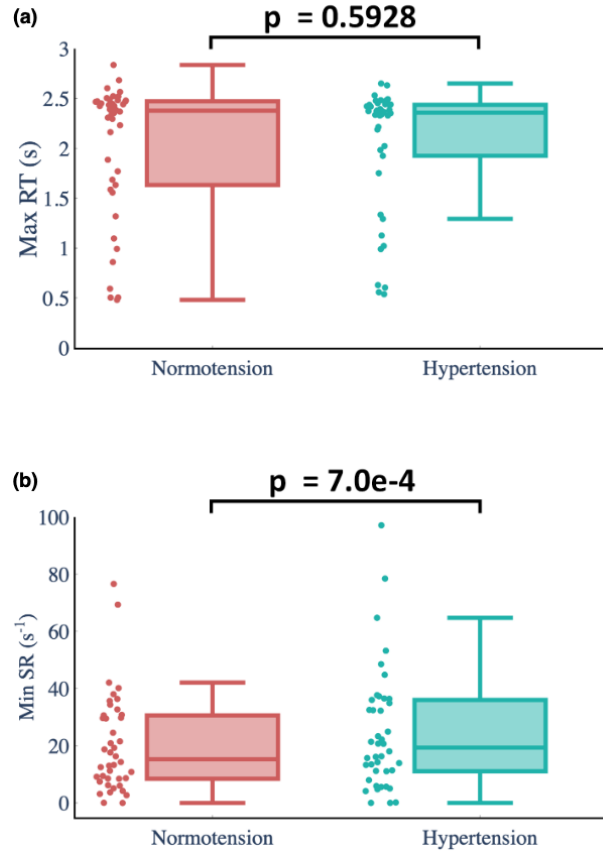


Figure 3.6: Comparison between normotension and hypertension for all 42 large and giant IAs in terms of the maximum RT and the minimum SR. In the box and whiskers plot, the horizontal line within the box denotes the median value. The lower and upper edges of the box denote the 25th and 75th percentiles. The ends of the whiskers are drawn to the upper and lower extreme values. p values were computed using the two-tailed t-test. (a) Maximum residence time (RT). (b) Minimum shear rate (SR).

3.4 Discussion

The prevalence of ST in large and giant aneurysms reported in the literature varies widely. ST occurs in 10% to 30% of unruptured large and giant aneurysms [Alberto et al., 2020], while the prevalence of ST varies from 30% to 70% [Alberto et al., 2020, Scerrati et al., 2019, Schubiger et al., 1980, Whittle et al., 1982] in giant aneurysms alone. For a specific cohort, the distribution of large and giant IAs can vary. The ST prevalence may be higher with a larger proportion of giant cases. This might be one of the main reasons why the ST prevalence in large and giant IAs varies widely. Another reason is that some statistics are based on limited sample size. To obtain more accurate

ST prevalence in aneurysms of different sizes, we conducted a comprehensive literature review. We collected 646 cases in the literature, with 437 small, 29 large, and 180 giant IAs. 7 out of 29 large IAs and 97 out of 180 giant IAs spontaneously thrombosed, therefore, the ST prevalence is $24.1\%(7/29) \pm 7.9\%$ for large IAs and $53.9\%(97/180) \pm 6.1\%$ for giant IAs, with 90% confidence. These were used as benchmarks to calculate the ST prevalence of large and giant IAs according to the distribution of large and giant IAs in our simulation cohort. Although large and giant IAs are more likely than small IAs to be spontaneously thrombosed, the intraluminal thrombosis is present in approximately the same proportion of giant aneurysms, regardless of location [Nurminen et al., 2014]. The ST prevalence of large and giant IAs in different locations (ICA, MCA, and BA) is shown in Table 3.5, but these statistics are not included in our calibration experiment as it is well-established that aneurysm size [Alberto et al., 2020, Ohta et al., 2001, Scerrati et al., 2019] is the main factor associated with ST, irrespective of its location [Nurminen et al., 2014].

Three main triggers of flow stasis-based clotting models appear in the literature: (1) high RT alone; (2) low SR or wall shear stress (WSS) alone; and (3) high RT and low SR/WSS in combination. However, there is no clear consensus on the values of the trigger thresholds, and published works studying ST haemodynamic thresholds often have small sample sizes. Based on CFD simulations conducted on 113 aneurysms—where particles injected into the parent vessel were tracked over multiple cardiac cycles—Leemans et al. [2019] found that the particle residence time for four out of five partially thrombosed aneurysms had a long residence time (>1.9 s). While thrombus formation has been reported to initiate as early as $RT = 1$ s [Hathcock, 2006], Marsh et al. [2020] found in their experiments that a threshold of $RT \geq 1$ s was ineffective as multiple patients in their cohort demonstrated a median $RT > 1$ s in the aneurysm, even before treatment. Reza and Arzani [2019] critically compared different RT measures in aneurysms. They compared Particle RT, Eulerian RT, and Virtual-ink RT (RT_{VI}) in one cerebral aneurysm geometry and obtained maximum RT values in the aneurysm sac of 0.66 s, 1.05 s, and 6.25 s, respectively. Rayz et al. [2010] estimated RT_{VI} and analysed the distribution of RT for 3 cases, for which they found that the mean RT was 18.22 ± 11 s (range 0.63-40.13 s) in the thrombosed area. Their results showed that a model with both low WSS and high RT could predict thrombosed areas significantly better than the models using RT or WSS alone. WSS correlates with SR through the viscosity

Table 3.8: Comparison between our CFD calibrated thresholds and the literature thresholds.

Results	Simulation	Literature
RT threshold (s)	1.9 (range: 1-2.3)	1 – 5 [Hathcock, 2006, Leemans et al., 2019, Marsh et al., 2020, Rayz et al., 2010, Sarrami-Foroushani et al., 2019]
SR threshold (s^{-1})	11 (range: 8-27)	10 – 25 [de Sousa et al., 2016, Gorrington et al., 2015, Sarrami-Foroushani et al., 2019]

of the fluid; however, SR is a measure of total blood deformation, which is a better indication of blood stagnation and potential thrombosis because it takes into account the shear forces due to both the wall and the surrounding fluid [Gorrington et al., 2015]. Based on experimental results from Nyilas et al. [1975], Gorrington et al. [2015] assumed that flow-induced thrombosis would be initiated when $SR < 10 s^{-1}$; however, a limitation of their work is that simulations were based on an idealized cavity rather than a real aneurysm geometry. Based on a Fourier analysis of SR at thrombosed locations in the aneurysm sac of 10 CFD simulations, de Sousa et al. [2016] determined $25 s^{-1}$ as the threshold for the initiation of thrombosis.

High RT and low SR are usually used in computational models to characterise the flow stasis that triggers the thrombus formation process in the aneurysm sac. We calibrated RT and SR thresholds using the clinical ST prevalence of large and giant IAs. Following calibration, the plausible range of RT and SR thresholds for our model are located in the overlap area in Fig. 3.4, which indicates that the corresponding simulation results are largely independent of the inter-subject flow variability. As shown in Table 3.8, the RT threshold is in the range [1.0, 2.3] s, with an average value of 1.9 s; the ST threshold is in the range [8, 27] s^{-1} , with an average value of 11 s^{-1} . The calibrated RT and SR thresholds are consistent with the literature and also more reliable due to the rigorous calibration based on clinical data.

ST is not a well-documented phenomenon in hypertensive patients. This might be because most patients treated for aneurysms have blood pressure-controlling measures in place [Thompson et al., 2015]. Using the calibrated RT and SR threshold values, our model predicted a slightly lower ST prevalence for our virtual cohort in hypertensive

conditions, modelled as boundary conditions from a CARS model [Lassila et al., 2020]. As shown in Fig. 3.6, the minimum SR in the aneurysm sac in hypertension is usually higher than in normotension ($P < 0.001$), although the maximum RT is relatively similar ($p = 0.5928$). SR is sensitive to changes in normotensive and hypertensive conditions, whereas RT is robust. Blood flow stasis-induced models are usually triggered by high RT and low SR. In a specific area in the aneurysm sac, only if RT is higher than the RT threshold and SR is lower than the SR threshold is the clotting process assumed to initiate. From our simulation results, the hypertensive conditions have limited effect on RT and SR in the aneurysm sac, thus only causing a slightly lower ST prevalence than is found in normotensive patients.

We performed CFD simulations for 109 cases and analysed the relationship between aneurysm geometry characteristics and flow, finding that bigger aneurysms usually have a higher AR in our cohort (Table 4.5). Higher AR and more complex shape (higher non-sphericity) lead to higher RT and lower SR in the aneurysm sac, and high RT and low SR ultimately trigger the thrombosis formation. There is a strong link between IA morphology and haemodynamics [de Sousa et al., 2016]. The high prevalence of thrombus formation within large and giant IAs is related to AR [Ohta et al., 2001]. Although high AR is not sufficient for reliable prediction of thrombus formation, IAs with higher AR are more likely to present with ST. High AR results in low velocity, low SR, and inhibition of pulsatile blood flow (Fig. 3.7, Fig. 3.8, and Fig. 3.9), leading to a pro-inflammatory and pro-coagulable micro-environment at the aneurysm wall [Alberto et al., 2020, de Sousa et al., 2016].

3.4.1 An Example Case Comparison Between Normotension and Hypertension

In this section, we show how hypertension affects the distribution and magnitude of RT and SR with an example case. We performed six simulations for each virtual case using six different inlet flow waveforms. A middle-aged female patient case (51 years old, aneurysm size 17.8 mm, AR 2.3, location Basilar Tip) was selected for a detailed analysis. The inlet flow shown in Fig. 3.3, which is generated from a MGM model [Sarrami-Foroushani et al., 2016] and a CARS model [Lassila et al., 2020] according to the age and gender of the patient, is imposed for simulation for this case. As shown in Fig. 3.10, the time-averaged velocity distributions are roughly similar for normotension and hypertension, although the velocity magnitude is slightly higher for normotension.

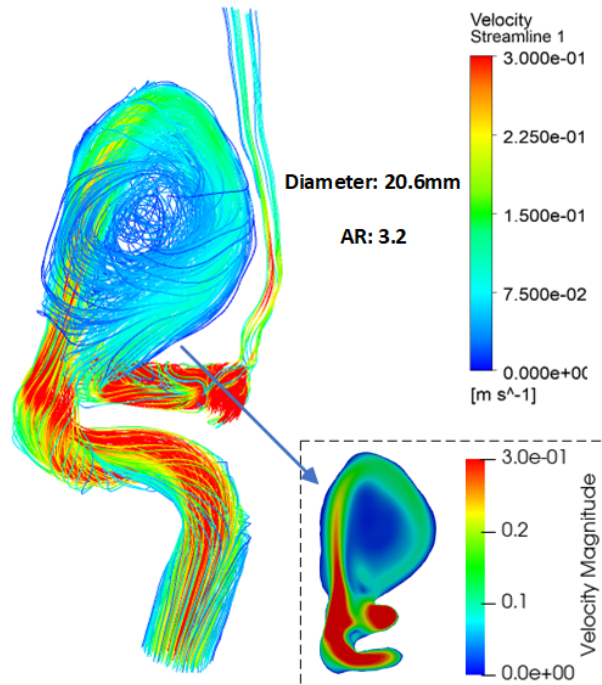


Figure 3.7: Velocity field and streamline plot of the highest AR case.

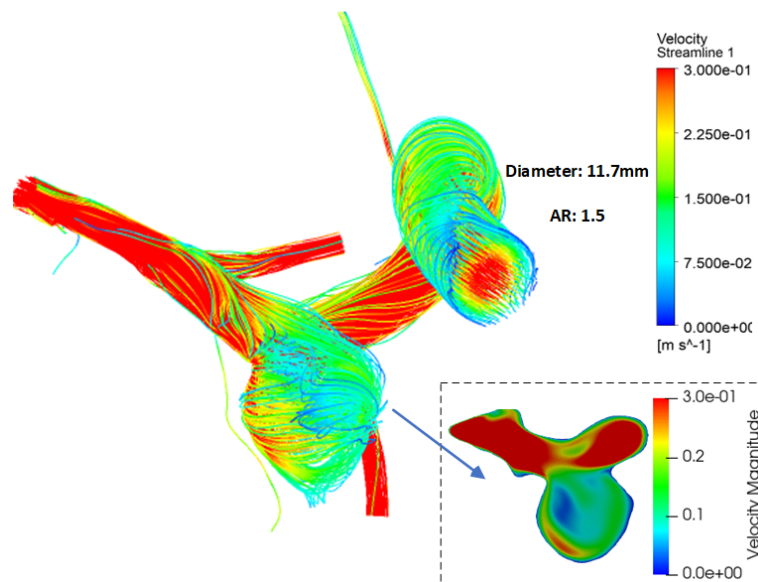


Figure 3.8: Velocity field and streamline plot of the mean AR case.

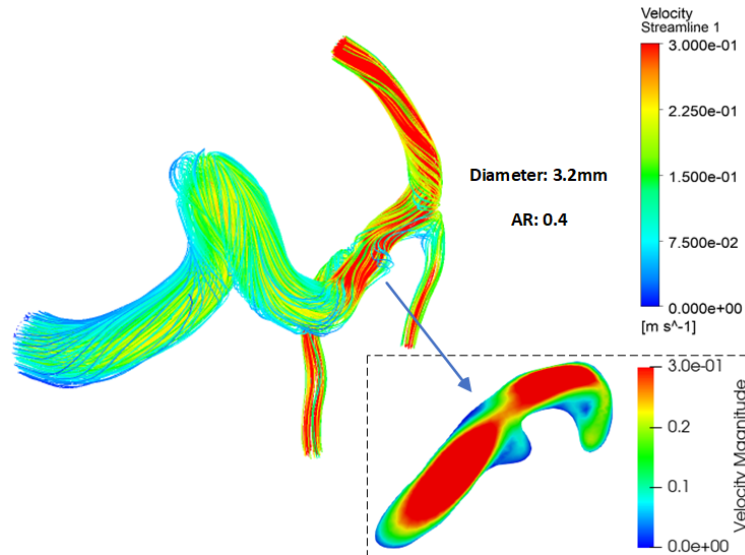


Figure 3.9: Velocity field and streamline plot of the lowest AR case.

This is because although the peak velocity of the hypertensive inlet flow waveform is higher than that of the normotensive inlet flow waveform, the mean velocity is higher for normotension (mean: 13.78 cm/s) than for hypertension (mean: 11.29 cm/s).

For a given state (normotension/hypertension), the distribution and magnitude of RT and SR are almost equivalent. For example, in Fig. 3.11, the results of Fig. 3.11(a) and Fig. 3.11(b) are very similar. The difference between the maximum RT values in normotensive and hypertensive conditions is small, whereas the distribution of RT differs. We found apparent differences in both the magnitude and distribution of SR from normotension to hypertension. In this case, slightly lower maximum RT and higher minimum SR in the aneurysm sac are observed in hypertensive conditions.

3.4.2 Limitations

Limitations: (1) We assumed clotting in the aneurysm sac was triggered by blood flow stasis, and high RT and low SR were usually used in computational models to characterise the flow stasis. Therefore, we only focused on studying RT and SR in this paper. (2) Although we performed a systematic review, we did not find enough data to estimate ST prevalence for small aneurysms. It is well-established that aneurysm size is the most important factor associated with ST and this phenomenon in large and giant aneurysms is well-documented. We only used the clinical ST prevalence of large

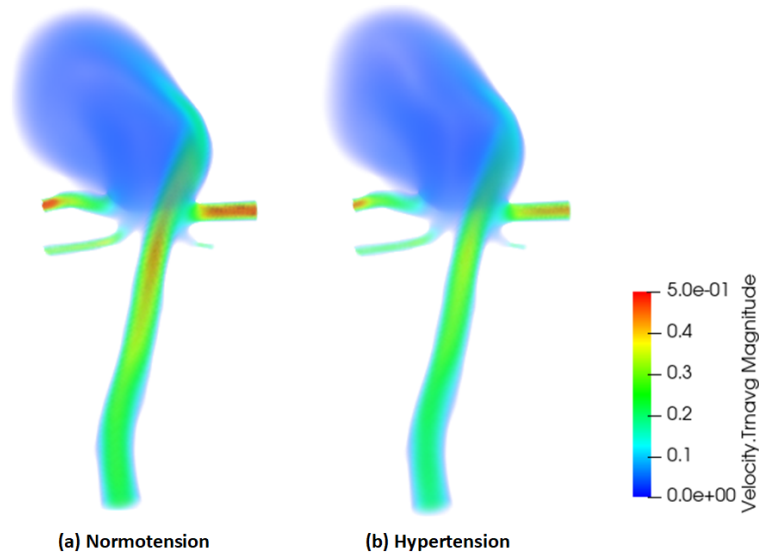


Figure 3.10: Comparison of the time-averaged velocity distribution between normotension and hypertension. The mean inlet flow velocity in normotension and hypertension is 13.78 cm/s and 11.29 cm/s, respectively.

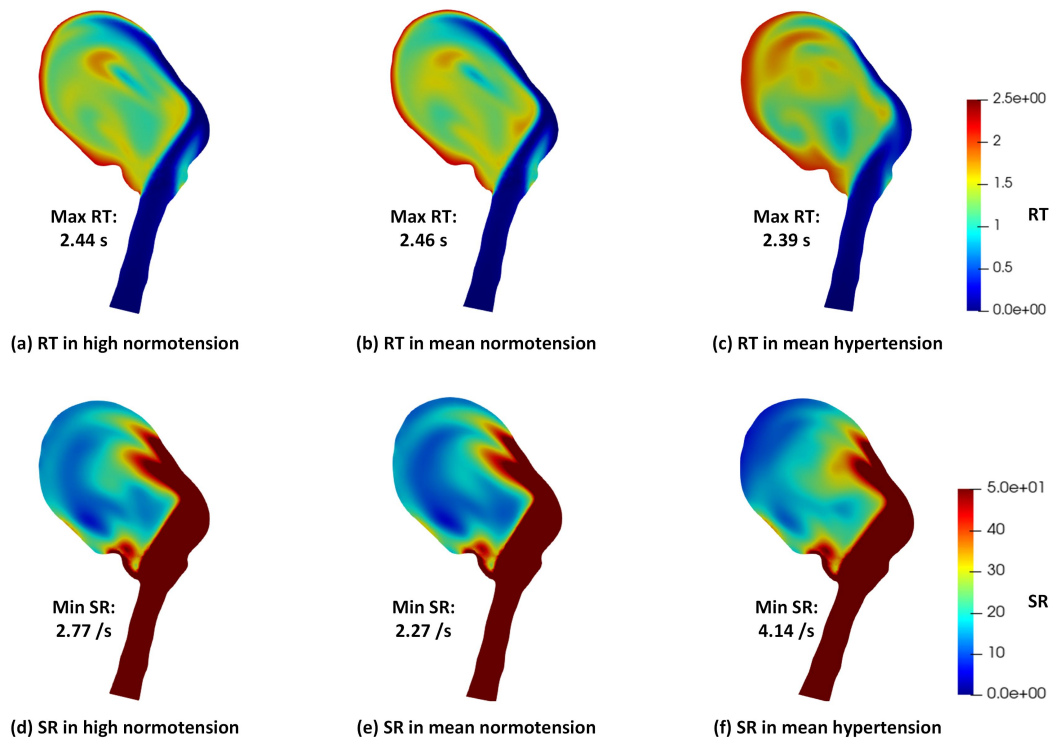


Figure 3.11: Residence Time (RT) and Shear Rate (SR) distribution in normotension and hypertension.

and giant IAs to calibrate our clotting model. (3) There were few ST cases reported in hypertensive patients for us to use to estimate the ST prevalence and compare our results. This might be because most patients treated for aneurysms have blood pressure-controlling measures in place. Ours is the first study that looked into RT and SR for hypertensive patients. Our results showing a slightly lower prevalence of ST in hypertensive cases were based only on the haemodynamics point of view and there may be other physiology involved that was not included in our analysis.

3.4.3 Conclusion

In this sensitivity analysis into stasis-driven thrombosis trigger thresholds, we first conducted a systematic literature review to estimate the clinical ST prevalence rate for a subgroup of the general population of aneurysms, namely those of large and giant size (>10 mm). We then performed a series of numerical simulations for a virtual cohort of 109 patients and used the estimated clinical ST prevalence of large and giant IAs as a criterion to calibrate the trigger thresholds in thrombosis models. We showed how thrombosis models can be calibrated on aneurysm cohort and then help to estimate the ST prevalence for a general population. To accelerate this *in silico* calibration experiment, we created a fully automatic workflow to segment the image data, generate the volume mesh, impose patient-specific boundary conditions and run the simulations on a cloud computing platform. Our results showed that the high prevalence of thrombus formation within large and giant IAs is related to high AR. Bigger aneurysms usually have a higher AR, and IAs with higher AR are more likely to be thrombosed. Our calibration experiment identified the plausible values of two commonly used thrombosis trigger threshold parameters, RT and SR, as 1.9 s and 11 s^{-1} , respectively. Furthermore, our model predicted a slightly lower ST prevalence in hypertensive than in normotensive patients due to the larger minimum SR in the aneurysm sac caused by hypertension. We found that SR is sensitive to the changes of boundary conditions from normotension to hypertension, while RT is more robust. This study not only collated ST literature and demonstrated how clinical ST prevalence data could guide computational thrombus formation modelling by identifying plausible ranges of model parameters, but also revealed that ST may be less common in hypertensive patients with large and giant IAs.

CHAPTER 4

Key Influencers in an Aneurysmal Thrombosis
Model: A Sensitivity Analysis and Validation
Study

Abstract—Thrombosis is a biological response closely related to IAs, and the formation of thrombi inside the aneurysm is an important determinant of outcome after endovascular therapy. As the regulation of thrombosis is immensely complicated and the mechanisms governing thrombus formation are not fully understood, mathematical and computational modelling has been increasingly used to gain insight into thrombosis over the last 30 years. To have a robust computational thrombosis model for possible clinical use in the future, it is essential to assess the model’s credibility through comprehensive sensitivity analysis of model parameters and validation studies based on clinical information of real patients. Here, we conduct a global sensitivity analysis on a previously developed thrombosis model, utilising thrombus composition, the flow-induced platelet index, and the bound platelet concentration as output metrics. These metrics are selected for their relevance to thrombus stability. The flow-induced platelet index quantifies the effect of blood flow on the transport of platelets to and from the site of thrombus formation and thus on the final platelet content of the formed thrombus. The sensitivity analysis of the thrombus composition indicates that the concentration of resting platelets most influences the final thrombus composition. Then, for the first time, we validate the thrombosis model based on a real patient case using patient-specific resting platelet concentration and two previously calibrated trigger thresholds for thrombosis initiation. We show that our thrombosis model is capable of predicting thrombus formation both before and after endovascular treatment.

4.1 Introduction

Intracranial aneurysm (IA) is a type of cerebrovascular pathology, which is a localized dilation or ballooning of the cerebral blood vessel caused by the weakness of the wall of a cerebral artery or vein [Withers et al., 2013]. There are three main treatment options for patients with IAs: observation, surgical therapy, and endovascular therapy [Keedy, 2006]. The goal of treating patients with unruptured IAs is to maximise their duration of high-quality life by optimally balancing the risks of aneurysm rupture with those of treatment-related adverse outcomes [Burns and Brown, 2009]. In the literature, 24.2% (244/1009) IAs [Briganti et al., 2015] failed to obtain aneurysm occlusion after endovascular or surgical treatment; aneurysm reopening and retreatment after endovascular coiling occurred in 20.8% (1697/8161) and 10.3% (840/8161), respectively [Ferns et al., 2009]. Some aneurysms failed to develop a stable clot even with sufficient levels

of flow reduction and may end up with post-treatment rupture, leading to high risks of mortality and morbidity [Byrne and Szikora, 2012, Kulcsár and Szikora, 2012, Sarrami-Foroushani et al., 2019]. From autopsy studies of aneurysms, researchers found that there are two different types of thrombi: organised white thrombus, rich in fibrin and platelet, and non-organised red thrombus, rich in fibrin and erythrocyte [Fischer et al., 2012, Sarrami-Foroushani et al., 2019, Turowski et al., 2011]. They can be found in stable clots and unstable clots, respectively. Red thrombi are the result of stagnation of blood flow, resulting in a clot containing all elements of normal blood, and they contain more enmeshed erythrocytes among sparse fibrin strands compared to precipitation or white thrombi. The red thrombi are expected to progress to organised white thrombi; otherwise, they may promote an inflammatory reaction, eventually leading to the disintegration of the aneurysm wall with subsequent rupture. Achieving organised white thrombi may reduce the probability of post-treatment rupture, and non-organised red thrombi have also been suggested as a potential predictor for unsatisfactory treatment results [Fischer et al., 2012, Sarrami-Foroushani et al., 2019, Turowski et al., 2011].

In unruptured aneurysms, thrombosis (spontaneous or device-induced) can stabilize the aneurysm or accelerate the path to rupture [Ngoepe et al., 2018]. Currently, in vivo or image-based analysis of thrombosis haemodynamics in realistic anatomies and physiologies is very difficult, if not impossible [Liu et al., 2023]. In recent decades, significant effort has been directed towards computational predictions of haemodynamics in aneurysms [Ngoepe et al., 2018]. However, computational prediction of thrombosis within aneurysms is relatively unexplored. The integrated thrombosis model originally developed by Sarrami-Foroushani et al. [2019] incorporates biochemical reactions, platelet activity, and haemodynamics. Briefly, the model combines platelet activation and transport with fibrin generation and defines a flow-induced platelet index (FiPi) as a quantitative measure of thrombus stability. According to aneurysm autopsy studies, two different types of thrombus have been identified: the unstable red thrombus (rich in fibrin and erythrocytes) and the stable white thrombus (rich in fibrin and platelets). FiPi quantifies the effect of blood flow on the transport of platelets to and from the site of thrombus formation, and thus on the final platelet content of the formed thrombus. FiPi is related to the initial concentration of the resting platelets, the initial concentration of the activated platelets, and the concentration of the bound platelets. During the thrombus formation process, resting platelets become activated by expos-

ure to thrombin or other activated platelets. The activated platelets adhere to the fibrin network aggregate to form bound platelets. Both activated and bound platelets are derived from resting platelets, and thus FiPi is highly related to the resting platelet concentration. [Sarrami-Foroushani et al. \[2019\]](#) set $\text{FiPi} > 0.15$ as a threshold for the formation of fibrin and platelet-rich white thrombi. This thrombosis model is not only capable of predicting both the haemodynamic changes and the thrombus formation process but is also able to predict long-term thrombus stability by investigating the thrombus composition. However, such a comprehensive computational thrombosis model that considers both haemodynamics and biochemical reactions is very complex with a large number of uncertain model parameters. Previously, we calibrated the haemodynamic thresholds, residence time (RT), and shear rate (SR), of thrombosis initiation against real population-specific data [[Liu et al., 2023](#)], but how the rest of the model parameters affect the final formed thrombus has not yet been assessed. To have a robust computational thrombosis model for possible clinical use in the future, it is essential to assess the model reliability through comprehensive sensitivity analysis (SA) of the model parameters and validation studies based on clinical information from real patients. Uncertainty quantification of a computational model is crucial in *in silico* trials to ensure the accuracy and reliability of predictions (model credibility) [[Food et al., 2021](#)], thus improving confidence in regulatory submissions. It helps identify and manage potential risks, ensuring robust and credible simulation outcomes that can effectively replace or supplement traditional clinical trials.

This paper aims to first identify the most influential factors in our previously developed thrombosis model [[Sarrami-Foroushani et al., 2019](#)] through a comprehensive global SA. We then validate the thrombosis model based on a real patient case (partial thrombosis before treatment and residual neck after immediate post-treatment) using patient-specific parameters for those identified as influential and two previously calibrated trigger thresholds [[Liu et al., 2023](#)] of thrombosis initiation. In addition, we improve our thrombosis modelling for untreated aneurysms by narrowing the thrombosis initiation in areas near the wall, as in the real situation, the thrombus is difficult to be suspended in an aneurysm lumen on its own without any anchors to the surrounding aneurysm wall. The novelty of this study is that we not only identify the most influential factors in the modelling of aneurysmal thrombosis, but also demonstrate for the first time the ability of our thrombosis model in predicting the thrombus

Table 4.1: 5 parameters that no need to be assessed.

Parameters	Default value (a)	Reference	Lower bound (50%a)	Upper bound (200%a)
Other				
Thrombin (nM)	0	[Anand et al., 2003]	*	*
Fibrin (nM)	0	[Anand et al., 2003]	*	*
Bound platelets (nM)	0	*	*	*
RT threshold (s)	1.9	Liu et al. [2023]	1	5
SR threshold (s^{-1})	11	Liu et al. [2023]	10	25

formation both before and after treatment based on a clinical case of the patient.

4.2 Materials and Methods

4.2.1 The thrombosis model parameters

The flow-stasis-induced thrombosis model in our group was originally developed by Sarrami-Foroushani et al. [2019]. Sarrami-Foroushani et al. [2019] assumed thrombosis to initiate and progress in regions where RT is greater than a threshold (e.g., 2.0 s) and SR is less than a threshold (e.g., $25 s^{-1}$). These trigger thresholds were calibrated by Liu et al. [2023] as 1.9 s and $11 s^{-1}$, respectively. As shown in Fig. 2.3, four main biochemically-coupled events that result in thrombus of fibrin mesh and aggregated platelets were considered. Details of the simulation specifications and equations for describing the blood flow transport and the biochemical reactions can be found in Chapter 2. FiPi was defined as the relative difference in the platelet concentration between a closed and an open system. More details can be found in chapter 2 equation (2.13) and Sarrami-Foroushani et al. [2019].

As shown in Table 4.1, Table 4.2, and Table 4.3, there are 31 input parameters in our thrombosis model. The default values of these 31 parameters are obtained from literature [Sarrami-Foroushani et al., 2019]. To perform comprehensive SA, we identify the upper and lower bounds of each parameter from the literature (e.g., upper and lower bounds of the fibrinogen concentration) or UK Biobank (e.g., upper and lower bounds of the resting platelet concentration). Where this information was not available, the upper and lower bounds of each parameter used in the following SA are set as the

Table 4.2: 12 parameters can be assessed with the 0D model and Sobol' method.

Parameters	Default value (a)	Reference	Lower bound (50%a)	Upper bound (200%a)
OD model and Sobol'				
$K_{th}^{rp}(UPLT^{-1}s^{-1}uM^{-1})$	6.5×10^{-10}	Sorensen et al. [1999]	50%a	200%a
$K_{th}^{ap}(UPLT^{-1}s^{-1}uM^{-1})$	3.69×10^{-9}	Sorensen et al. [1999]	50%a	200%a
$K_{th}^{bp}(UPLT^{-1}s^{-1}uM^{-1})$	3.69×10^{-10}	Sorensen et al. [1999]	50%a	200%a
$K_{th}^{at}(uM^{-1}s^{-1})$	7.083×10^{-3}	Sorensen et al. [1999]	50%a	200%a
$K_{fi}^{th}(s^{-1})$	59.0	Anand et al. [2003]	50%a	200%a
$K_{m,fi}^{th}(nM)$	3160	Anand et al. [2003]	50%a	200%a
$K_{pa}^{th}(s^{-1})$	0.5	[Kuharsky and Fogelson, 2001]	50%a	200%a
$K_{pa}^{ap}(nM^{-1}s^{-1})$	0.3	[Kuharsky and Fogelson, 2001]	50%a	200%a
$K_{pb}(s^{-1})$	1.0×10^4	[Leiderman and Fogelson, 2011]	50%a	200%a
$C_{fi,50}(nM)$	600	[Anand et al., 2003]	50%a	200%a
$C_{bp,50}(platelets/um^3)$	7.0×10^5	[Wufsus et al., 2013]	50%a	200%a
$C_{th,50}(nM)$	9.11×10^{-1}	Sorensen et al. [1999]	50%a	200%a

Table 4.3: 14 parameters can be assessed with the full 3D model and EE method.

Parameters	Default value (a)	Reference	Lower bound (50%a)	Upper bound (200%a)
3D model and EE				
$D_{pt}(cm^2s^{-1})$	5.21×10^{-7}	[Anand et al., 2003]	50%a	200%a
$D_{at}(cm^2s^{-1})$	5.57×10^{-7}	[Anand et al., 2003]	50%a	200%a
$D_{th}(cm^2s^{-1})$	6.47×10^{-7}	[Anand et al., 2003]	50%a	200%a
$D_{fg}(cm^2s^{-1})$	3.10×10^{-7}	[Anand et al., 2003]	50%a	200%a
$D_{fi}(cm^2s^{-1})$	2.47×10^{-7}	[Anand et al., 2003]	50%a	200%a
$D_{rp}(cm^2s^{-1})$	2.50×10^{-7}	[Leiderman and Fogelson, 2011]	50%a	200%a
$D_{ap}(cm^2s^{-1})$	2.50×10^{-7}	[Leiderman and Fogelson, 2011]	50%a	200%a
$K_{fi}(um^2)$	1.2×10^{-1}	[Wufsus et al., 2013]	0.0015×10^{-1}	1.2×10^{-1}
$K_{bp}(um^2)$	3.1×10^{-1}	[Wufsus et al., 2013]	50%a	200%a
Prothrombin (nM)	1400	[Anand et al., 2003]	1100	200%a
Antithrombin (nM)	2410	[Anand et al., 2003]	50%a	3400
Fibrinogen (nM)	7000	[Anand et al., 2003]	4000	10000
Resting platelets (ml^{-1})	2×10^8	UK Biobank	1.14×10^8	4.38×10^8
Activated platelets (%)	5	Sorensen et al. [1999]	1	20

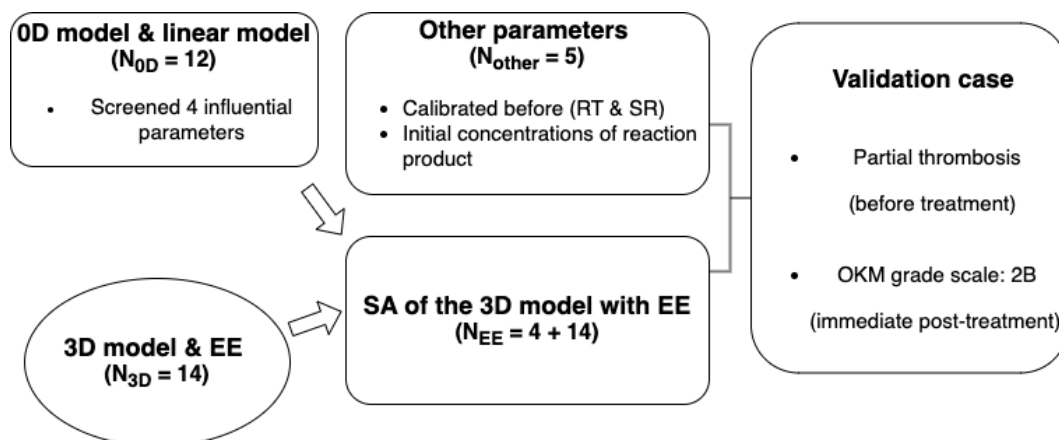


Figure 4.1: The sensitivity analysis (SA) workflow. There are 31 parameters in our thrombosis model with 12 parameters that can be assessed with a lumped 0D model, 14 that can be investigated with the 3D full model, and 5 others that do not need to be assessed. We first screened 4 influential parameters from the 12 kinetic-associated parameters using the lumped 0D model, then performed SA with the elementary effect (EE) method using the 3D full model for 18 (4 + 14) parameters to identify the most influential model parameter. Finally, we further demonstrated the necessity of SA with a validation case by comparing the simulation results under patient-specific and non-patient-specific settings with the clinical ground truth.

variation 200% (upper bound) or 50% (lower bound) of the literature default value.

There are five parameters that do not need to be included in the SA (Fig. 4.1 and Table S1). Three of these parameters are the initial concentrations of thrombin, fibrin, and bound platelets, as we assume that no thrombus formed before the thrombus formation process began. These three biochemical species are also the product of the associated biochemical reactions; for example, thrombin is generated by the conversion of prothrombin to thrombin on the surface of resting and activated platelets. Therefore, it is reasonable to set the initial concentrations of these three species to 0. The other two parameters that are not included in the SA are the RT and SR thresholds, as these were previously calibrated by Liu et al. [2023] using the prevalence of clinical spontaneous thrombosis.

The thrombosis model is complex and time-consuming, requiring 5-20 days per case using 256 cores, as it combines haemodynamics with eight coupled biochemical reactions. To efficiently identify the most influential parameters, we first developed a lumped parameter model and used the least-squares fitted linear model [Saltelli, 2008] to screen for key parameters from the 12 kinetic parameters. For those identified as

key parameters using the lumped parameter model, along with the other 14 parameters, we then employed the 3D full thrombosis model and the elementary effect (EE) method [Andrea et al., 2008] to identify the most influential parameters. Finally, we validated the thrombosis model using a real patient case, which exhibited partial thrombosis before treatment and a residual neck after immediate post-treatment, by applying patient-specific values for the parameters identified as the most influential.

4.2.2 0D model and least-squares fitted linear model

We denote by C_{PT} , C_{TH} , C_{AT} , C_{FG} , C_{FI} , C_{RP} , C_{AP} , and C_{BP} the bulk concentrations of prothrombin, thrombin, antithrombin, fibrinogen, fibrin, resting platelets, activated platelets, and bound platelets, respectively. The biochemical reaction of each species in the lumped parameter model was modelled using the following equation:

$$\frac{\partial C_i}{\partial t} = S_i, \quad (4.1)$$

where C_i is the species concentration and S_i is the reaction term. The full form of all advection-diffusion-reaction equations can be found in the supplementary material.

In the simplified lumped parameter model, we assume that each species is fully diffused at its initial concentration. We then apply the least-squares fitted linear model [Saltelli, 2008] to investigate the lumped parameter model using the duration of thrombus formation (the simulation time from 0% to the final 95% thrombosed) as the output metric.

As a first approximation, the dependency can be viewed as linear in each parameter. Consider a model with k inputs $\mathbf{X} = (X_1, X_2, \dots, X_k)$ and the output metric is Y , the entire model being simulated would behave approximately like so:

$$Y = b_0 + \sum_{i=1}^k b_i X_i = b_0 + b_1 X_1 + b_2 X_2 + \dots + b_{k-1} X_{k-1} + b_k X_k \quad (4.2)$$

where the b_i 's are all constants that we assume are unknown at the start of SA. When the model is run with a set of parameter values, a data point becomes available for SA. In general n simulations will result in the following $n \times (k + 1)$ system of linear equations,

$$\begin{bmatrix} 1 & x_{11} & \cdots & x_{1k} \\ 1 & x_{21} & \cdots & x_{2k} \\ \vdots & \vdots & \ddots & \vdots \\ 1 & x_{n1} & \cdots & x_{nk} \end{bmatrix} \begin{pmatrix} b_0 \\ b_1 \\ \vdots \\ b_k \end{pmatrix} = \begin{pmatrix} y_1 \\ y_2 \\ \vdots \\ y_n \end{pmatrix}$$

which can be abbreviated using matrix notation as

$$X_{nk}B_k = Y_n \tag{4.3}$$

The matrix X_{nk} has 1's in the first column, and experimental values for the k parameters in the n simulations in the remaining columns. B_k contains the $k + 1$ unknown coefficients corresponding to the intercept b_0 and the k parameters. Y_n contains the n output values from the n simulations. Unless otherwise stated, we used $n = 1000$. If n is strictly greater than $k + 1$, it will not be possible to solve the equations exactly, unless the model is in fact linear, as the system of equation is overdetermined [Saltelli, 2008]. However, a least-squares solution will generally be available. As solving an overdetermined system of equations for a least-squares solution is computationally expensive and random samples tend to be poorly conditioned for large k because of clustering, we used Sobol sequences [Renardy et al., 2021] to generate the samples. Sobol sequences are a particularly common example of low-discrepancy sequences and exhibited faster convergence in comparison with random and Latin hypercube sampling (LHS) sampling, as has been demonstrated with correlated normal distributions in finance applications [Bianchetti et al., 2016].

4.2.3 Elementary effect (EE) method

The EE method [Andrea et al., 2008] can be regarded as an extension of the changing one parameter at a time (OAT) approach but it is a global approach as the EE method partially overcomes the limitations of the OAT approach by introducing wider ranges of variations for inputs and averaging a number of local measures so as to remove the dependence on a single sample point. Consider a model with k inputs $\mathbf{x} = (x_1, x_2, \dots, x_k)$, the input space is discretised into a p -level grid Ω . For a given

value of x , the elementary effect of the i th factor is defined as:

$$EE_i = \frac{[y(x_1, x_2, \dots, x_{i-1}, x_i + \Delta, \dots, x_k) - y(x_1, x_2, \dots, x_k)]}{\Delta}, \quad (4.4)$$

where p is the number of levels, Δ is a value in $1/(p-1), \dots, 1-1/(p-1)$. $\mathbf{x} = (x_1, x_2, \dots, x_k)$ is any selected value in Ω such that the transformed point $(x + e_i\Delta)$ is still in Ω and e_i is a vector of zeros but with a unit as its i th component.

Morris [1991] suggested an efficient design to build r paths of $(k+1)$ points in the input space, each providing one EE value for each of k parameters, r independent paths give r EE values for each parameter. The sensitivity measure, improved by Saltelli et al. [2005], μ^* and σ are the estimates of the mean of the absolute values and the standard deviation of the EE distribution associated with the i th parameter. μ_i^* is a measure of influence of the i th parameter on the output metric, while σ_i is a measure of non-linear and/or interactive effects of the i th parameter. Here, the output metric is the measure of thrombus composition (FiPi and the bound platelet concentration).

$$\mu_i = \frac{1}{r} \sum_{j=1}^r EE_i^j, \quad (4.5)$$

$$\mu_i^* = \frac{1}{r} \sum_{j=1}^r |EE_i^j|, \quad (4.6)$$

$$\sigma_i^2 = \frac{1}{r-1} \sum_{j=1}^r (EE_i^j - \mu)^2, \quad (4.7)$$

The computational cost to implement the EE method is $r(k+1)$. Unless otherwise stated, we used $p = 4$ and $r = 5$ in this study.

4.2.4 Validation study

After the comprehensive SA study, we identified the most influential parameters of our thrombosis model. To improve the model's performance and credibility, it is necessary to obtain patient-specific values for the parameters identified as influential ones. After anonymisation, we used a patient case (partial thrombosis before treatment and residual neck after immediate flow diverter & coiling treatment; Male; 52 years old; normotension; platelet count, $2.07 \times 10^{11}/ml$; aneurysm size, 16.5 mm; aspect

Table 4.4: Patient-specific flow-diverter model and coils information.

Flow-diverter	P64 (4×24 mm)
Coils	
1	Target XL 360 standard 14 mm \times 50 cm
2	Target XL 360 standard 12 mm \times 45 cm
3	Target 360 standard 10 mm \times 30 cm
4	Target XL 360 soft 8 mm \times 30 cm
5	Target 360 soft 7 mm \times 30 cm
6	Target 360 soft 5 mm \times 30 cm
7	Target XL 360 soft 6 mm \times 20 cm
8	Target 360 soft 5 mm \times 20 cm
9	Target 360 soft 5 mm \times 20 cm
10	Target 360 soft 5 mm \times 15 cm

ratio, 2.2; location, MCA) from Leeds General Infirmary as a validation study case by comparing the thrombus regions predicted by our model with the clinical ground truth both before and after treatment. We collected the 3D rotational angiography images and detailed clinical records from Leeds General Infirmary (Fig. 4.2 (a)), segmented the vasculature and aneurysm with a deep learning-based approach VASeg[Lin et al., 2023], manually labeled the partially thrombosed regions with ITK-SNAP 3.8.0 (Fig. 4.2 (b)), obtained the patient-specific vascular surface mesh, deployed the virtual stent and coils with GIMIAS (version 1.8.r1) [Larrabide et al., 2009], generated the volume mesh using ANSYS ICEM CFD v19.3 (Ansys Inc. Canonsburg, PA, USA), imposed the patient-specific inlet flow waveform generated from a multivariate Gaussian model[Lassila et al., 2020, Sarrami-Foroushani et al., 2016], ran the thrombosis model on an HPC cluster ARC4, and post-processed the simulation results with ANSYS CFD-POST and Paraview 5.10.0-RC1. The patient-specific clinical flow-diverter model and coils information can be found in Table 4.4.

When modelling the stent, we are often concerned with alterations in the flow pattern and haemodynamics in the aneurysm rather than detailed flow fields near the walls of the parent vessel[Appanaboyina et al., 2009]. Given this, only the portion of the stent that crosses the neck of the aneurysm is modelled to reduce the computational expense of the simulations. The resolution of the mesh in the vicinity of the stent wires

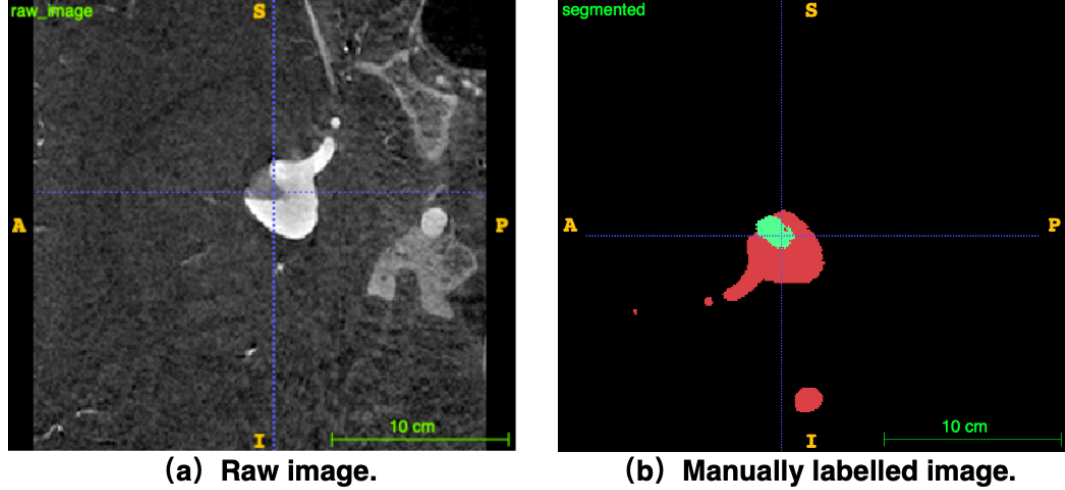


Figure 4.2: A partially thrombosed clinical case with manual label of the thrombosis region before treatment. (a) The raw image from Leeds General Infirmary. (b) The manually labelled partial thrombosis regions (the green regions), the manually labelled aneurysm sac and parent vessel regions (the red regions).

was set according to [Sarrami-Foroushani et al. \[2019\]](#), where the independence of the mesh was obtained for the maximum edge size of 0.01 mm on the wires. The packing density, defined as the ratio of the volume of the physically inserted coil to the volume of the aneurysm, for this patient-specific case is 21.5%. The coils were discretised with a mesh resolution of $1.5 \times$ the diameter of the primary coil [[Babiker et al., 2013](#), [Fujimura et al., 2018](#)]. The above settings resulted in volumetric meshes with 27 million total number of elements for this patient-specific case with a single flow diverter and 10 coils. The details of the mesh convergence analysis were previously described in Chapter 2 and [[Liu et al., 2023](#), [Sarrami-Foroushani et al., 2019](#)].

4.2.5 Narrowing the thrombosis initiation to areas near the wall

[Rayz et al. \[2010\]](#) found that thrombus forms in layers, with the initial layer adhering to the arterial wall in regions of increased flow residence time and then gradually expanding into the aneurysmal bulge. Moreover, imaging studies of untreated aneurysms often show thrombus formations that are closely associated with areas of altered flow patterns near the aneurysm wall, rather than suspended freely within the aneurysm sac [[Strother et al., 1989](#)]. For untreated aneurysms, the thrombus is difficult to be suspended in an aneurysm lumen on its own without any anchors to the aneurysm

wall. Previously, we calibrated the trigger thresholds based on the prevalence of clinical spontaneous thrombosis (RT threshold 1.9 s and SR threshold 11 s^{-1}) [Liu et al., 2023]. Here, we further constrain the thrombus to only initiate and progress near the wall or other thrombosed regions (where the fibrin concentration, C_{FI} , is greater than 600 nM [Sarrami-Foroushani et al., 2019]).

In this study, we mainly consider saccular aneurysms as the saccular type accounts for 90% of IAs [Keedy, 2006]. Saccular aneurysms are spherical in shape and the aneurysm sac can be approximated with a least square fit ellipsoid or sphere [Piccinelli et al., 2012]. Therefore, we can separate all aneurysm points into near-wall points and internal points by a virtual ellipsoid or sphere inside the aneurysm sac. We set the center of the virtual ellipsoid or sphere to coincide with the center of the least square fit ellipsoid or sphere. The radius of the virtual ellipsoid and sphere is set as half the value of the least square fit ellipsoid or sphere radius. Then we used a Hill function to constrain the initiation of thrombus formation for all internal points. The Hill function is a sigmoidal activation function of the form $\phi_p^{fi} = C_{FI}^n / (C_{FI}^n + C_{FI,50}^n)$, where the rate of occurrence of an event, p , requires an appropriate concentration of fibrin, $C_{i,50}$ is the fibrin concentration where the half maximum activation (half saturation) occurs, and the Hill coefficient (the exponent n) reflects the steepness of the response curve. In this study, we set $C_{i,50} = 600 \text{ nM}$ and $n = 4$ in the trigger mechanism.

Spontaneous thrombosis of unruptured intracranial aneurysms is a common event that can be detected incidentally during advanced neuroradiological studies before treatment [Alberto et al., 2020, Cohen et al., 2007, Whittle et al., 1982]. These spontaneously thrombosed aneurysms are considered unstable dynamic structures that may grow, recanalize, bleed, compress, or cause thromboembolic events [Cohen et al., 2003, 2007, Whittle et al., 1982]. The validation case may eventually become complete spontaneous thrombosis. But it was treated when the partial thrombosis was fresh and unstable, as noted by the clinician. Complete spontaneous thrombosis can sometimes stabilize the growth of the lesion, however, 33% (7/21) of the completely thrombosed aneurysms presented recanalization at follow-up [Alberto et al., 2020]. The spontaneously formed thrombus was neither stable nor mature before treatment, making it inappropriate to compare a converged simulation result with an unstable and unconverged clinical ground truth. For the pre-treatment simulations, our approach is to select the simulation time that best matches the clinical ground truth. For instance,

in the non-constrained initiation model, the thrombus formed at 30 seconds of simulation time closely resembles the clinical ground truth, so we used this time point. Consequently, for the constrained initiation model, we also ran the simulation for 30 seconds.

4.3 Results

4.3.1 SA results of the lumped parameter model

Using the reduced lumped parameter model, we conducted 14,000 simulations for -50% to +200% variation of 12 kinetic parameters (Table 4.2) using the thrombus formation duration as the output metric. As shown in Fig. 4.3, the SA results indicate that the duration of thrombus formation is sensitive to 4 kinetic parameters: $C_{FI,50}$, K_{FI}^{TH} , K_{TH}^{AP} , and K_{TH}^{AT} . Platelet recruitment and deposition were assumed to depend on the concentration of free platelets and the value of a second-order Hill function ϕ_{PB}^{FI} with $C_{FI,50} = 60$ nM. K_{FI}^{TH} is a kinetic constant related to thrombin-mediated fibrin generation. K_{TH}^{AP} is the kinetic constant of the kinetic reaction of thrombin generation on the surface of activated platelets. Thrombin inhibition by antithrombin was modelled as a second-order reaction with kinetic constant, K_{TH}^{AT} . The other 8 kinetic-related parameters have limited or negligible effects on the lumped parameter model.

4.3.2 SA results of the full 3D model using EE method

We identified 4 key parameters from the SA results of the lumped parameter model. These 4 kinetic-related parameters and another 14 parameters (Table 4.3) were assessed based on a 3D aneurysm geometry (Fig. 4.4: a spontaneous thrombosis case from our previous study [Liu et al., 2023]; Male; 51 years old; aneurysm size, 6.8 mm; aspect ratio, 1.5; location, PCoA) using the 3D full model and EE method. For 18 parameters and 5 randomly generated paths, we conducted $r(k+1) = 95$ model runs for the 3D full thrombosis model using the EE method. According to previous studies [Anand et al., 2003, 2008, Sarrami-Foroushani et al., 2019], the clot was assumed to be formed in regions where the fibrin concentration is greater than 600 nM. As shown in Fig. 4.5, the space-averaged fibrin concentration in the aneurysm sac is converged at 100 cardiac cycles when using three different resting platelet concentration values. Therefore, we

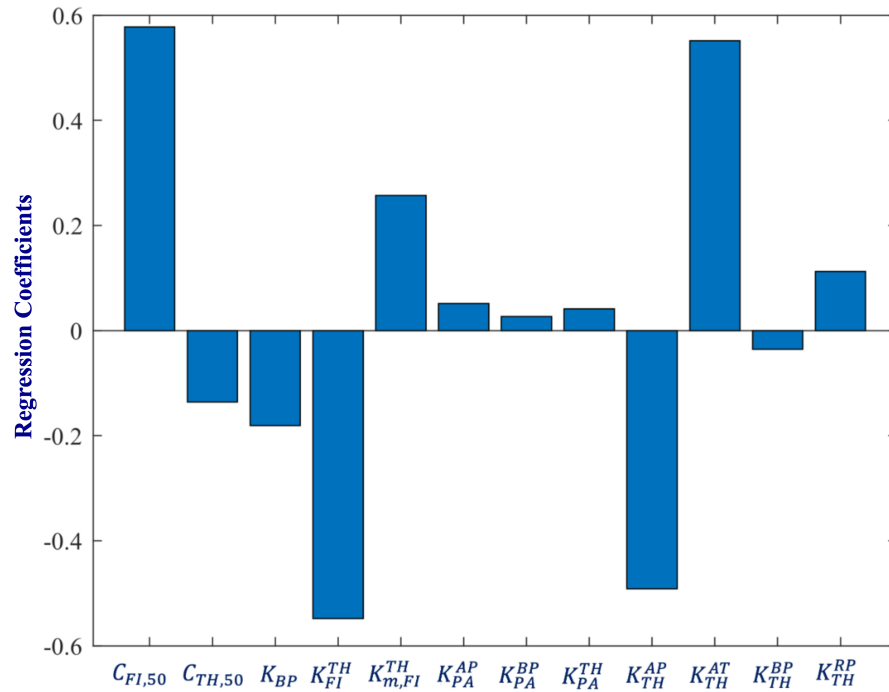


Figure 4.3: The 0D model & least-squares fitted linear model results show that 4 kinetic-related parameters: $C_{FI,50}$, K_{FI}^{TH} , K_{TH}^{AP} , and K_{TH}^{AT} have significant effect on the lumped parameter model.

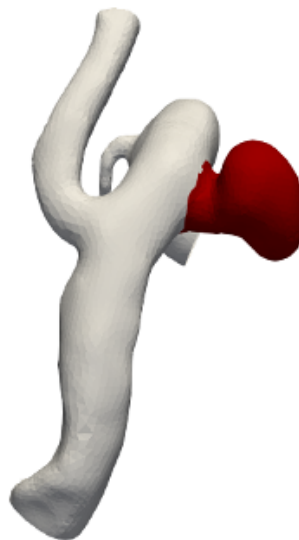


Figure 4.4: 3D vessel & aneurysm geometry used in the sensitivity analysis study.

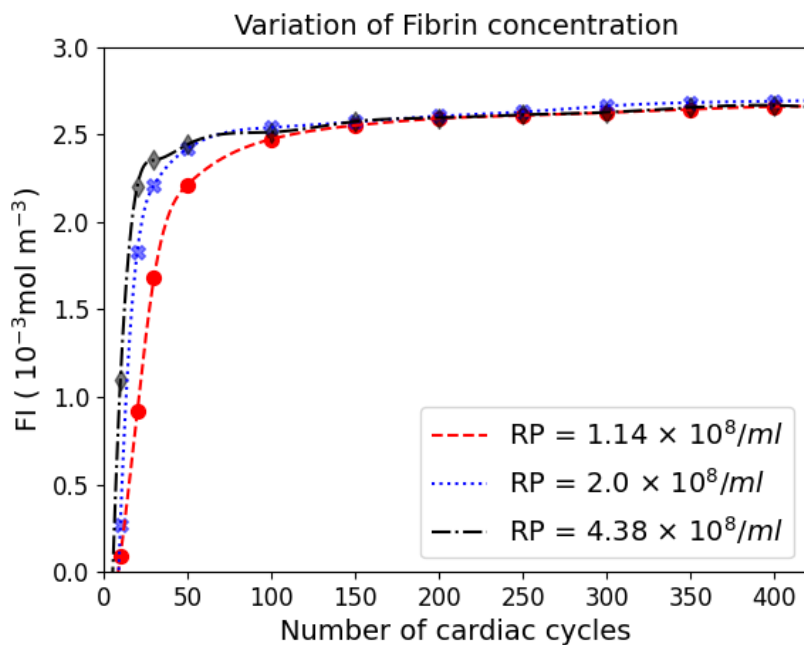


Figure 4.5: Convergence of the sensitivity analysis simulations.

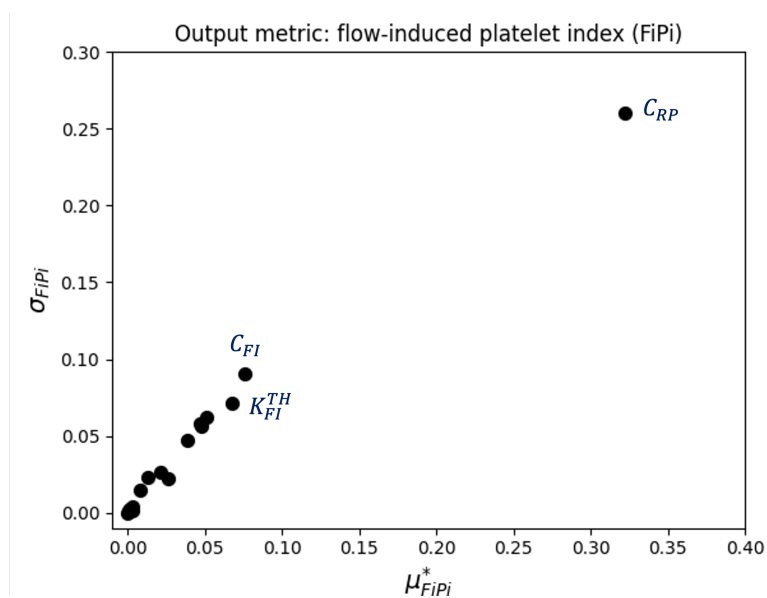


Figure 4.6: The 3D model & Elementary effect (EE) method results using FiPi as the output metric indicate that the resting platelet concentration is the unique most important parameter that affects the final formed thrombus composition.

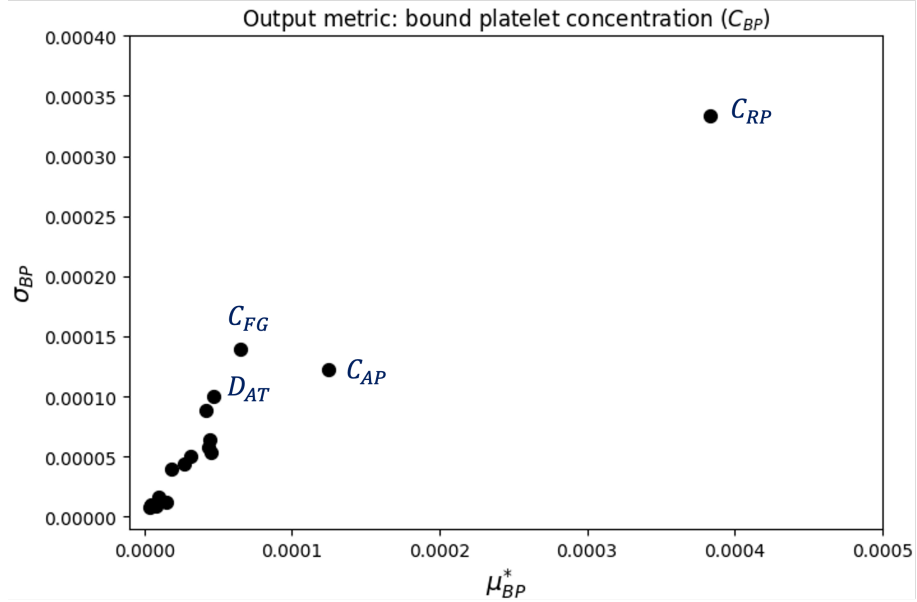


Figure 4.7: The 3D model & Elementary effect (EE) method results using bound platelet concentration as output metric indicate that the resting platelet concentration is the unique most important parameter that affects the final formed thrombus composition.

ran all 95 simulations for 100 cardiac cycles in this SA study using EE method. The output metric is the measure of thrombus composition (FiPi [Sarrami-Foroushani et al., 2019] and the bound platelet concentration). The EE method allows us to classify the inputs into three groups: (1) Small μ_i^* : inputs have negligible effects; (2) Large μ_i^* and small σ_i : inputs having large linear effects without interactions; (3) Large μ_i^* and large σ_i : inputs having large non-linear and/or interaction effects.

As shown in Fig. 4.6 and Fig. 4.7, the SA results show that the concentration of resting platelets has the greatest effect on the final formed thrombus composition (FiPi and bound platelet concentration), while the other 17 parameters have limited or negligible effects on the thrombosis model.

4.3.3 Validation study based on a real patient case with detailed clinical records

Simulation results of the untreated aneurysm

High RT and low SR are widely used in computational models to characterize flow stasis that triggers the thrombus formation process in aneurysms. In our previous in

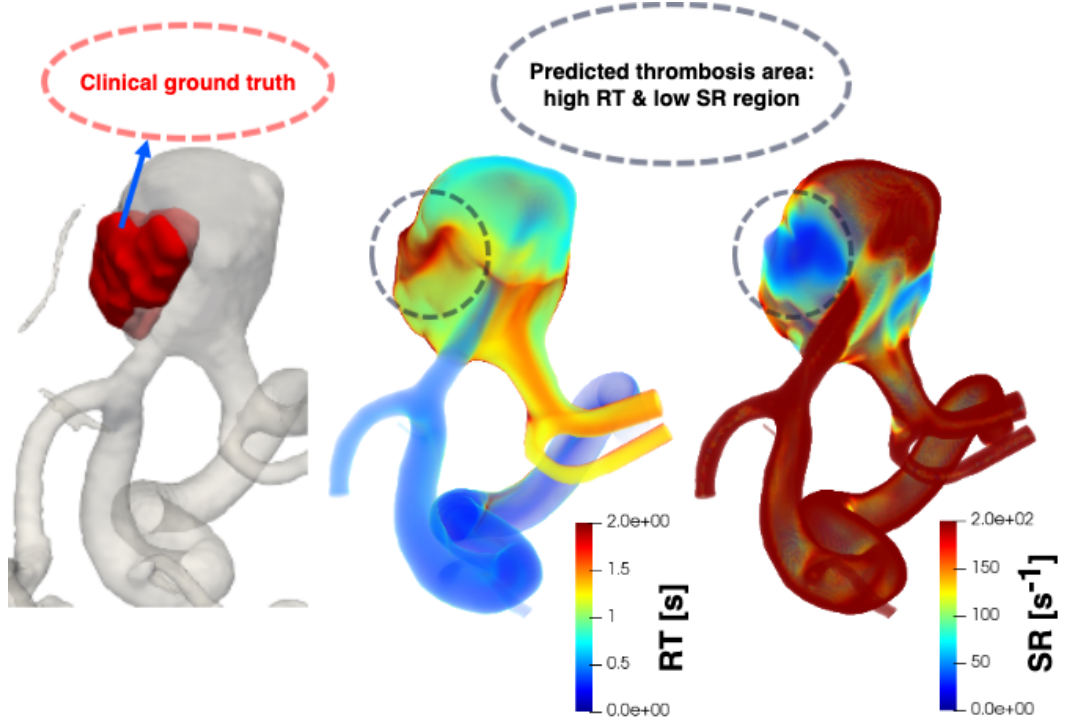


Figure 4.8: We manually labeled the partial spontaneous thrombosis region as pre-treatment clinical ground truth. High residence (RT) and low shear rate (SR) are widely used in computational models to characterize the flow stasis that triggers the thrombosis formation process in the aneurysm sac. Using our previously calibrated trigger thresholds[Liu et al., 2023], RT 1.9 s and SR 11 s^{-1} , our flow simulation model successfully predicted the main thrombosis area before treatment.

in silico observational study[Liu et al., 2023], we calibrated these trigger thresholds as RT 1.9 s and SR 11 s^{-1} . Using these calibrated trigger thresholds, we ran the flow simulation model (about 10 hours per run using 128 cores) to obtain haemodynamics inside the aneurysm sac to predict the possible thrombosis region. The flow simulation with all the reaction terms switched off is an initialization simulation for the following coupled flow and thrombosis simulation. From haemodynamics (Fig. 4.8), this patient-specific aneurysm is shown to be a spontaneous thrombosis case and the main possible thrombosis region is located in the left side of the aneurysm sac, which coincides with the clinical ground truth before treatment.

We then performed the coupled flow and thrombosis model (about 10 days per run using 128 cores) to investigate how the selection of patient-specific and non-patient-specific parameters affects the final formed thrombi (Table 4.5). The settings of non-

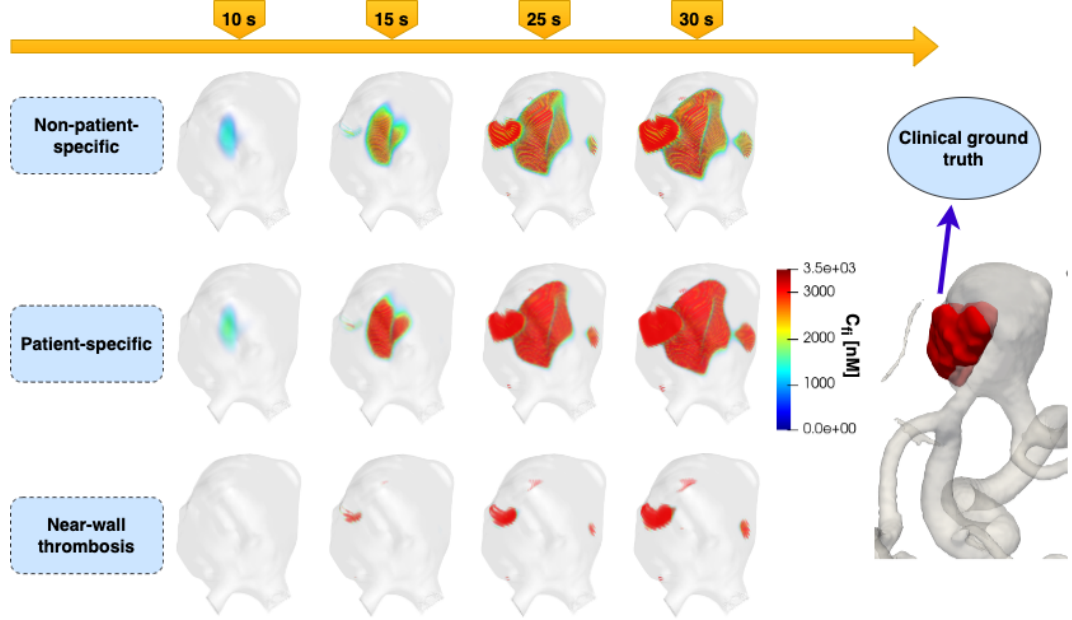


Figure 4.9: Comparison between the patient-specific and non-patient-specific simulation results using the clinical record as ground truth. In the clinical ground truth figure, the red part was the manually labelled partial thrombosis region. In the simulation results, the thrombus were assumed to be formed in regions where the fibrin concentration, C_{fi} , is greater than 600 nM.

Table 4.5: Comparison between patient-specific and non-patient-specific modelling.

	Non-patient-specific	Patient-specific	Near-wall thrombosis	Clinical ground truth
RP concentration (ml^{-1})	2.0×10^{11}	2.07×10^{11}	2.07×10^{11}	2.07×10^{11}
FI concentration (nM)	7000	15000	15000	> 13000
Simulation results				
Thrombus percentage (%)	22.5	24.6	8.7	17.7
Stable thrombus percentage (%)	40.6	44.6	32.2	n/a

The definition of the percentage of thrombus is: thrombus volume / aneurysm volume, and the definition of the percentage of stable thrombus is: volume of stable thrombus / thrombus volume. We used FiPi to classify the formed thrombi into stable and unstable types. Here, we set $\text{FiPi} > 0.15$ [Sarrami-Foroushani et al., 2019] as a threshold for the formation of a fibrin and platelet-rich white (stable) thrombus. Due to current imaging limitations, we were only able to identify areas of thrombus formation in patients who were still alive, but were unable to further analyse the composition or stability of the thrombus. We have used “n/a” to denote that we do not know the exact percentage of stable thrombus for this patient.

patient specific parameters were from [Sarrami-Foroushani et al. \[2019\]](#), while the settings of patient-specific parameters were from the patient’s clinical record. As shown in [Fig. 4.9](#), the red part (located in the lower-left corner of the aneurysm sac) in the clinical ground truth figure is the manually labeled partial thrombosis region. There is no significant difference between the patient-specific simulation results and the non-patient-specific simulation results in terms of the location of the thrombi and the shape of the thrombi. However, a higher percentage of stable thrombi (44.6%) was obtained in the patient-specific model compared to the non-patient-specific model (40.6%). The patient-specific and non-patient-specific models predicted that the thrombosis region was located in the middle and left sides of the aneurysm sac and the thrombus grew mainly from the middle of the lumen to the aneurysm wall, which is unrealistic, as the thrombus is difficult to be suspended in the middle of the sac without any anchors. To address this model limitation, we constrained the thrombosis initiation to occur only near the wall or other thrombosed regions. As shown in the third row of [Fig. 4.9](#), the thrombus grew mainly near the left wall, rather than in the center of the sac, which better matches the clinical ground truth prior to treatment. Although the wall-constrained initiation model successfully predicted the primary thrombosis initiation site before treatment, the extent of thrombosis was significantly underestimated compared to the clinical ground truth. As mentioned earlier, the comparison with clinical observations is complex by the unstable and unconverged state of the thrombus. Nevertheless, successfully predicting the main thrombosis initiation site is considered a significant achievement.

Simulation Results of the Treated Aneurysm

As shown in [Fig. 4.10](#), we virtually deployed patient-specific coils and flow diverter using GIMIAS (version 1.8.r1) [[Larrabide et al., 2009](#)]. We then performed a post-treatment simulation with patient-specific virtual treatments and patient-specific concentrations of resting platelets and fibrinogen for 200 cardiac cycles of simulation time. It took about 2 months to obtain the results of the post-treatment simulation using 128 cores. The volume of the formed thrombi in the aneurysm sac over time is presented in [Fig. 4.11](#). The thrombus grows very slowly and it is noteworthy that the thrombus volume at 175 cardiac cycles reaches 95% of the final volume observed at 325 cycles.

According to the O’Kelly-Marotta [[Joshi et al., 2013](#), [O’kelly et al., 2010](#)] (OKM)



Figure 4.10: Virtual deployment of the stent and coils according to the patient-specific treatment information.

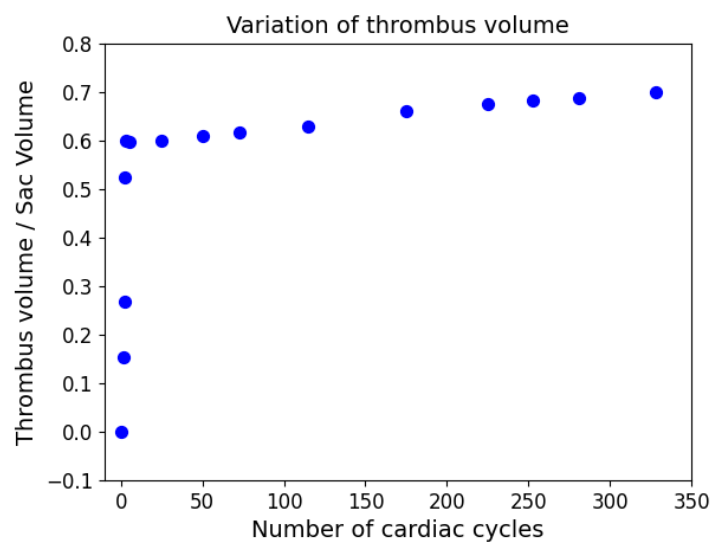


Figure 4.11: Variation of the thrombus volume for the post-treatment simulation. The thrombus grows rapidly at the very beginning (0-5 cycles), and then the growth slows down (5-325 cycles). For this patient-specific case, the thrombus volume at 5 cardiac cycles reaches 86% of the final volume observed at 325 cycles. The thrombus volume at 175 cardiac cycles reaches 95% of the final volume at 325 cycles.

grading scale, aneurysms are assigned grades based on the amount of contrast filling of the aneurysm sac (filling grades, A, B, C, D) and how long contrast persists in the aneurysm sac with respect to angiographic phase (stasis grades, 1, 2, 3). For this patient-specific aneurysm case treated with a flow diverter and ten coils, the aneurysm incompletely filled its lumen with contrast that persists within the lumen into the capillary phase of the angiogram (Fig. 4.12 (a)). It was assigned grade 2B according to the clinical record. As shown in Fig. 4.12, our simulation results show good agreement with the clinical immediate post-treatment angiographic result: minimal residual flow in the neck of the aneurysm after treatment.

4.4 Discussion

Thrombosis is a biological response closely linked to intracranial aneurysms. The thrombus formation process is usually slow and complex as it is associated with blood flow and the net result of a series of biochemical reactions. The multi-scale and multi-physics nature of thrombosis has inspired a wide range of modelling approaches applied to various phenomena that aim to address how a thrombus forms [Gutierrez et al., 2023]. Although different modelling methods can be coupled as informed by the scale and physics, the development of an all-encompassing computational model of thrombosis, combining all relevant underlying phenomena for patient-specific applications remains impractical, and, instead, it is necessary to simplify models and to focus on specific questions [Gutiérrez et al., 2021, Gutierrez et al., 2023]. The main interest of our thrombosis model is to investigate the thrombus composition/stability. Our novel model combines platelet activation and transport with fibrin generation, which is key to characterizing stable and unstable thrombus [Sarrami-Foroushani et al., 2019]. Our model does not consider the fibrinolysis process which involves the breakdown of a fibrin clot [Boluijt et al., 2015]. Therefore, the thrombus would keep growing according to the haemodynamics until reach a constant volume and won't dissolve as the fibrinolysis process is not included in our model. The clot is to be formed in regions where the fibrin concentration is greater than 600 nM [Anand et al., 2003, 2008, Sarrami-Foroushani et al., 2019]. Based on this, we could assume that the fibrinolysis takes place where the concentration drops below this threshold [Ngoepe et al., 2018] if the fibrinolysis process needs to be included in our model in the future.

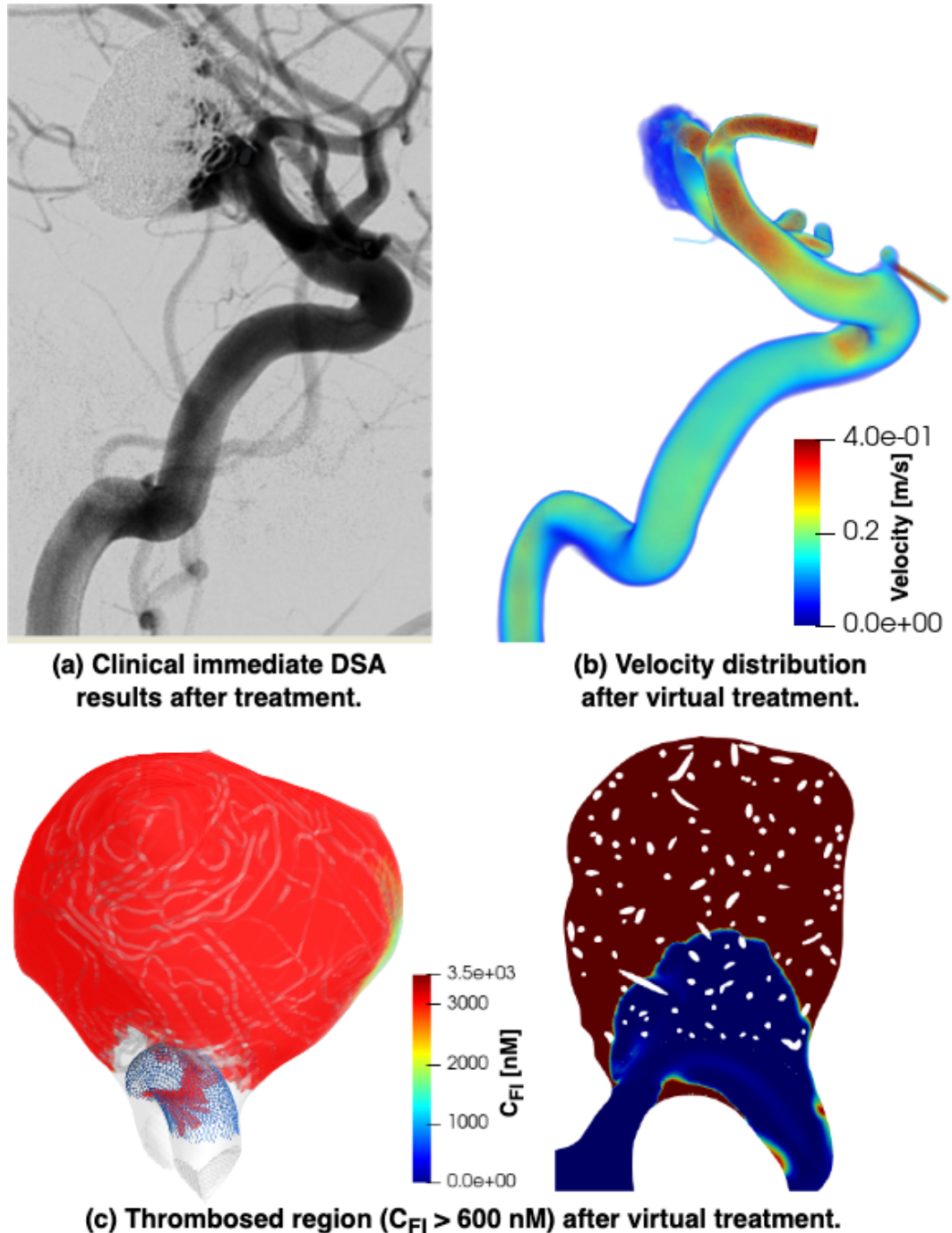


Figure 4.12: Qualitative comparisons between the immediate post-treatment angiographic result and our simulation result. (a) The clinical immediate post-treatment digital subtraction angiography (DSA) result shows minimal residual flow in the neck of the aneurysm; (b) The post-treatment simulation result also shows residual blood flow in the neck region of the aneurysm; (c) The thrombus formation result predicted by our thrombosis model after virtual patient-specific treatment. The thrombi are assumed to be formed in regions where the fibrin concentration, C_{FI} , is greater than 600 nM. The white patches in the slice shown are caused by the visualisation of the virtual coils.

Given the complexity of thrombosis, with at least 80 coupled reactions that regulate thrombus growth [Cito et al., 2013, Taylor et al., 2016], a comprehensive computational thrombosis model considering both the haemodynamics and biochemical reactions is usually very complex and time-consuming with a large number of uncertain model parameters even after simplification. Our thrombosis model was originally developed by Sarrami-Foroushani et al. [2019], where they built computer models of the in vitro phantom experiments and compared computational simulations of the flow diverter-induced thrombosis against in vitro observations reported in Gester et al. [2016]. A good agreement was achieved in that study. There are 31 model parameters in our thrombosis model [Sarrami-Foroushani et al., 2019] with 8 biochemical reactions coupled to the transport of the blood flow. Previously, we calibrated the trigger thresholds (RT and SR thresholds) of thrombosis initiation as there is no consensus on the trigger thresholds, with different values used throughout the literature [Liu et al., 2023, Rayz et al., 2010, Sarrami-Foroushani et al., 2019]. Building on this threshold calibration study [Liu et al., 2023], in the present study we performed a global SA to identify the most influential parameters and further validate our thrombosis model based on a real patient case. The unique most influential model parameter identified by the whole SA workflow is the resting platelet concentration, which means the concentration of resting platelets has the biggest effect on the final formed thrombus composition.

Our flow simulation model successfully predicted the spontaneous thrombosis status before treatment. The flow simulation is efficient (about 10 hours per run for the untreated aneurysm) compared with the time-consuming thrombosis model (about 10 days per run for the untreated aneurysm), but can only provide haemodynamic information. To investigate the details of the formed thrombi, we ran the coupled haemodynamics and thrombosis model. As shown in Fig. 4.9, even using literature average values, our model is robust in predicting the main thrombi formation region. The concentration of patient-specific resting platelets primarily affects the composition/stability of the thrombi (Table 4.5) which is consistent with our SA results. The resting platelet count distribution obtained from more than 400,000 cases from UK Biobank can be found in Fig. 4.13 where 90% of the population was within $1.14 \times 10^8/\text{ml}$ and $4.38 \times 10^8/\text{ml}$ (Table 4.3). Given there is such a large range in the resting platelet concentrations for the general population, it is important to use patient-specific resting platelet concentration information when investigating the composition/stability of

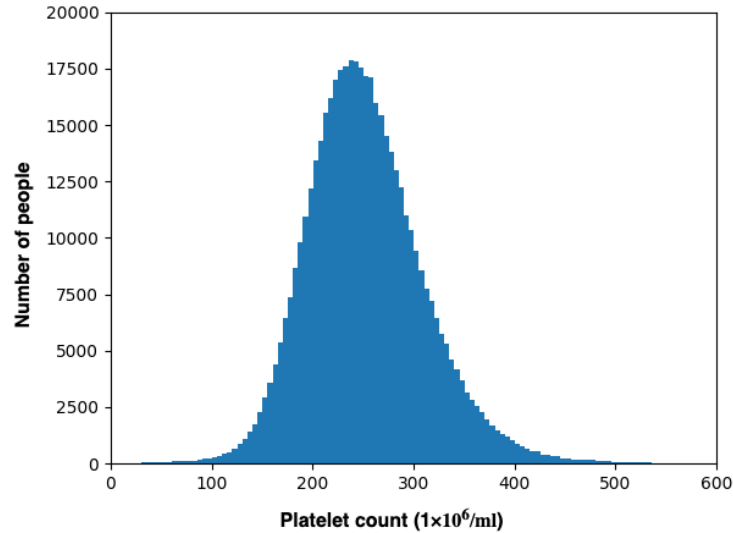


Figure 4.13: Resting platelet count distribution obtained from more than 400,000 cases from UK Biobank.

thrombi for individual cases.

We assumed the thrombus formation was triggered by blood flow stasis, which was characterized by high RT and low SR . Here, we further constrained the thrombosis initiation to only happen in regions near the wall or other thrombosed regions by adding a Hill function into the trigger mechanism for all internal points in the untreated aneurysm sac. This makes the thrombus formation process more realistic as for an untreated aneurysms the thrombus is difficult to be suspended in the lumen on its own without any anchors to the surrounding aneurysm wall. As shown in Fig. 4.8, Fig. 4.9, and Fig. 4.12, the simulation results of our thrombosis model show good agreement with the clinical ground truth both before treatment (spontaneous thrombosis) and immediate post-treatment (residual neck). It has been shown that aneurysmal thrombi form or at least deposit in regions of slow flow and low shear stress [Malaspinas et al., 2016, Ou et al., 2017, Rayz et al., 2008, Sarrami-Foroushani et al., 2017]. As illustrated in Fig. 4.12 (c), there are flow-stasis regions in the vicinity of the device within the main vessel that contribute to thrombus formation. In practice, this patient was treated with dual antiplatelet therapy consisting of aspirin and prasugrel (“75 mg of aspirin indefinitely and 10 mg of prasugrel for 6 months”). Dual antiplatelet therapy helps prevent stent-related thromboembolic events in cardiac patients and is commonly used

during neurointerventional procedures [Akbari et al., 2013]. This may explain why there were no thromboembolic events reported in the clinical records for this patient. The reported incidence of thrombus formation at the interface of the coil and the parent vessel is approximately 7%, based on retrospective analyses [Bruening et al., 2006, Workman et al., 2002].

The post-treatment simulation is very time-consuming, taking months. The suggested future work from this study is to accelerate the thrombosis simulation to investigate the long-term post-treatment thrombus formation after patient-specific virtual endovascular treatments in an efficient way. Despite limitations due to the excessive run time, our results have demonstrated that our calibrated model can accurately predict the formed thrombus regions. The model could therefore be considered as a useful tool in clinical decision-making after further population-level and patient-specific validation studies, particularly when the run times are reduced and it becomes viable to use the model when planning treatments.

4.4.1 Limitations

Limitations: (1) We assumed the thrombus formation in the aneurysm sac was triggered by blood flow stasis, and high RT and low SR were widely used in computational models to characterize the flow stasis. There may be other trigger mechanisms involved that were not included in our analysis. (2) The partially thrombosed regions were manually labeled with ITK-SNAP 3.8.0. There may be unavoidable errors due to subjective factors and the technical limitations of precise labeling of thrombosed areas. Although our model successfully predicted the main thrombosed region located in the left side of the aneurysm sac, the simulation results also showed that there is a small piece of thrombi formed in the right side of the aneurysm. In the raw images, we didn't see apparent thrombi there. (3) As our thrombosis model is very time-consuming, we performed the global SA of our model only using a single geometry. Although our simulation results have demonstrated that our calibrated model can accurately predict the formed thrombus regions for the validation case, this study is limited to only one case. Further population-level validation studies should be investigated to increase the model credibility.

4.4.2 Conclusion

In this comprehensive SA into all thrombosis model parameters and further clinical patient case validation study, we identified the unique most influential factor in aneurysmal thrombosis modelling, the resting platelet concentration. We also demonstrated that our thrombosis model is effective in predicting the thrombus formation both before and after treatment based on a clinical patient case, thereby further validating our model. Further large-scale validation studies across multiple patients are required to build additional trust in the model, but our results suggest there is significant value in using computational models to aid clinical decision-making.

CHAPTER 5

Time Discretisation in the Solution of
Advection-Diffusion-Reaction Equations with
PINNs

Abstract — When modelling the thrombus formation process, the transport of biochemical species involved in thrombosis is typically modelled using advection-diffusion-reaction (ADR) equations. Over the past decades, physics-informed neural networks (PINNs) – neural networks that are trained to solve supervised learning tasks while respecting any given laws of physics described by general nonlinear partial differential equations [Raissi et al., 2019] – have been increasingly used for modelling physical systems. However, the accuracy of the standard continuous-time PINNs model suffers from non-linearities and higher-order derivatives [Mattey and Ghosh, 2022]. In this study, we compared the performance of the standard continuous-time PINNs model with that of a discrete-time PINNs model in solving ADR equations in a 2D channel. The reference solution for the 2D channel problem was obtained using the finite difference method (FDM). For time discretisation, we applied the backward differentiation formulae (BDF). We first tested the BDF-PINNs model on the 2D channel problem and then combined BDF with SIREN, a neural network architecture employing the sine function as a periodic activation function, to investigate the performance of BDF-SIREN in solving ADR equations in a 2D idealised aneurysm. We found that the BDF-PINNs model required less training data and better represented the residence time (RT) solution in the 2D channel, showing much smaller relative errors compared to the standard continuous-time PINNs model. Furthermore, the tanh-based architecture (a neural network architecture using tanh activation functions) struggled to capture the fine details of RT in the 2D aneurysm, whereas the BDF-SIREN architecture was able to represent more detailed features. The reference solution for the 2D idealised aneurysm problem was solved using ANSYS CFX. However, the relative errors of all the PINNs models increased over time; for example, the relative error of the BDF-SIREN architecture could exceed 30% after two cardiac cycles. Therefore, improving the long-term stability of PINNs in solving ADR equations remains an area requiring further investigation.

5.1 Introduction

Mesh-based schemes, such as finite difference methods (FDM), finite element methods, and finite volume methods, are widely used approaches for solving partial differential equations (PDEs) [Calabrò et al., 2023]. These methods require the initial

generation of grid points or elements, which can be challenging when the shape of the computational domain is complex. The PDE solution is then approximated by evaluating it at a set of grid points or elements distributed over the spatiotemporal domain [He and Tartakovsky, 2021]. The discrete solution is obtained by discretising the time and spatial derivatives of the state variables. While mesh-based methods are accurate, they can be computationally expensive for complex problems, such as nonlinear PDEs [Mattey and Ghosh, 2022].

The flow stasis-induced thrombosis model used in our group was originally developed by Sarrami-Foroushani et al. [2019], where the transport of biochemical species involved in the thrombus formation process was modelled using eight advection-diffusion-reaction (ADR) equations, which were coupled with the Navier-Stokes equations. The coupled Navier-Stokes equations and transport equations for eight biochemical species were solved in ANSYS CFX v19.3 (Ansys Inc., Canonsburg, PA, USA) using a finite element method. This complexity makes it very time-consuming to model flow-thrombosis; for example, simulating thrombosis in a flow-diverted aneurysm (with more than ten million mesh elements) can take up to one month on a 96-core computer [Sarrami-Foroushani et al., 2019]. The main reasons why the integrated thrombosis model is so time-consuming are as follows: (1) the vast number of mesh elements (usually more than ten million for modelling the post-treatment aneurysm); (2) the fluid-structure interaction between the blood flow and the formed thrombus at each time step; and (3) the very small time-step size [Sarrami-Foroushani et al., 2019] (between 0.0001s and 0.001s) required to achieve sufficient convergence for such a complicated system. To test a large number of patients for different kinds of medical devices or products, numerous *in silico* trials are needed. However, traditional computational fluid dynamics (CFD) simulations typically require significant computing resources and time or may not be sophisticated enough to capture the salient details of the thrombus formation process [Malaspinas et al., 2016, Ou et al., 2017, Ouared et al., 2016, Rayz et al., 2010, Sarrami-Foroushani et al., 2019]. Consequently, the need for extensive simulations in *in silico* trials calls for accelerated computational models.

Recent advances in solving PDEs using deep learning techniques offer a promising alternative method for simulating thrombus formation. Physics-informed neural networks (PINNs) are neural networks that can be trained to solve supervised learning tasks while respecting any given laws of physics described by general nonlinear PDEs

[Raissi et al., 2019]. Unlike traditional mesh-based methods, PINNs operate in a meshless framework that uses automatic differentiation [Baydin et al., 2018], a family of techniques similar to but more general than backpropagation for efficiently and accurately evaluating derivatives of numeric functions expressed as computer programs, to represent all time and space derivatives, thus eliminating the need for explicit mesh generation [Raissi et al., 2019, Yin et al., 2020]. The PINNs method approximates the solution of PDEs with deep neural networks (DNNs). The PDEs are encoded into the loss function, and the DNNs' coefficients are computed by minimising this loss function, which includes the residuals of the PDEs, the training data, initial conditions, and boundary conditions [He and Tartakovsky, 2021]. A key advantage of PINNs is their ability to be effectively trained using small data sets (e.g., boundary data only or boundary data and a small portion of interior data), a scenario often encountered in the study of physical systems where data acquisition costs may be prohibitive [Raissi et al., 2019]. Additionally, nearly any neural network package can easily leverage GPUs for parallel computing. With the rapid growth in computational resources, PINNs are increasingly being used for modelling and simulating physical systems.

Given the complexity of our thrombosis model (eight ADR equations coupled with the Navier-Stokes equations), it is challenging to immediately replace our existing CFD codes with PINNs. Based on my current knowledge, there is no PINNs-based thrombosis model in the literature yet. The majority of PINNs codes for solving PDEs have been tested primarily on 1D problems [He and Tartakovsky, 2021, Maczuga and Paszyński, 2023, Matthey and Ghosh, 2022, Raissi et al., 2019, Vadyala et al., 2022, Wang et al., 2021, Yang et al., 2021], a few on 2D problems [Cai et al., 2021, He and Tartakovsky, 2021, Matthey and Ghosh, 2022, Raissi et al., 2019, Wang et al., 2021], and very few on 3D problems [Biswas and Anand, 2023, Cai et al., 2021, Moser et al., 2023]. This is mainly because the performance of neural networks can be significantly affected by the complexity and dimensionality of the problem. High-dimensional problems are usually more complex, requiring neural networks to possess higher representational power. This implies that the network needs more parameters (e.g., more layers or wider layers) to capture the intricate patterns, which increases the difficulty of training the model and the risk of overfitting, while gradient descent algorithms struggle to find global optima.

In this study, we investigate how PINNs perform in solving ADR equations used to

describe the transport of biochemical species. We compare the continuous-time PINNs model with the discrete-time PINNs model for a single 2D ADR equation in terms of model accuracy. For the discrete-time methods, we investigate the BDF techniques for ADRs, as BDF methods of orders 2-4 are preferred over the commonly used forward Euler method, which is known for its slow convergence and potential for order reduction or numerical instability [Calabrò et al., 2023]. This study explores the accuracy, efficiency, and stability of PINNs in solving ADR equations, which could provide new insights for simulating the full thrombosis model with PINNs in the future.

5.2 Materials and Methods

5.2.1 Advection-Diffusion-Reaction Equation

The transport of biochemical species can be modelled using ADR equations. Our thrombosis model comprises eight ADR equations, with the primary differences among them pertaining to the source term or reaction term. In this study, we test our PINNs codes with a 2D ADR equation to solve for residence time (RT), as its source term is relatively simple. RT is modelled as a tracer passively transported with the blood flow by solving the following ADR equation:

$$\frac{\partial C_{RT}}{\partial t} + \mathbf{u} \cdot \nabla C_{RT} - D_{RT} \nabla^2 C_{RT} - 1 = 0, \quad x \in \Omega, \quad t \in [0, T], \quad (5.1)$$

where t is time, \mathbf{u} is the velocity vector, $C_{RT}(x, y, t)$ is the local concentration of RT, Ω is a subset of R^d , D_{RT} represents the self-diffusivity of the flow ($D_{RT} = 1.14 \times 10^{-11} \text{ m}^2 \text{ s}^{-1}$) [Harrison et al., 2007, Menichini and Xu, 2016]. The source term considers a unit increase in the concentration of RT for each unit increase in time [Menichini and Xu, 2016]. The initial and inlet concentrations of RT were set as zero. A zero flux boundary condition was adopted on the wall and outlet boundary [Menichini and Xu, 2016].

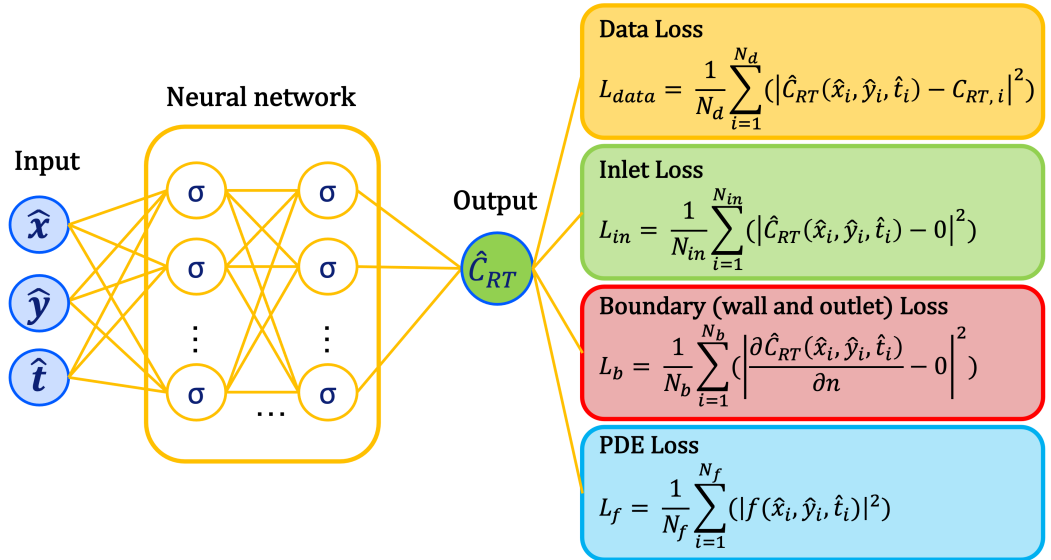


Figure 5.1: Basic overview of the continuous-time physics-informed neural network (PINNs) used in this chapter, displaying network inputs, output, and the four loss components.

5.2.2 The Continuous-time PINNs Model

Considering the continuous-time PINNs model for solving equation (5.1), we define $f(\hat{x}, \hat{y}, \hat{t})$ to be given by the left-hand side of equation (5.1):

$$f := \frac{\partial \hat{C}_{RT}}{\partial \hat{t}} + (\mathbf{u} \cdot \nabla) \hat{C}_{RT} - D_{RT} \nabla^2 \hat{C}_{RT} - 1 \quad (5.2)$$

In the context of PINNs [Raissi et al., 2019], a fully connected forward neural network composed of multiple hidden layers is used to approximate the solution of the PDE $\hat{C}_{RT}(\hat{x}, \hat{y}, \hat{t})$ by taking the space and time coordinates $(\hat{x}, \hat{y}, \hat{t})$ as inputs (Fig. 5.1). The network can be derived by applying the chain rule for differentiating compositions of functions using automatic differentiation [Baydin et al., 2018]. In PINNs, solving equation (5.1) is converted into an optimisation problem by iteratively updating the trainable neural network model parameters with the goal of minimising the mean squared error loss

$$Loss = L_{data} + L_{in} + L_b + L_f, \quad (5.3)$$

where

$$L_{data} = \frac{1}{N_d} \sum_{i=1}^{N_d} (|\hat{C}_{RT}(\hat{x}_i, \hat{y}_i, \hat{t}_i) - C_{RT,i}|^2) \quad (5.4)$$

$$L_{in} = \frac{1}{N_{in}} \sum_{i=1}^{N_{in}} (|\hat{C}_{RT}(\hat{x}_i, \hat{y}_i, \hat{t}_i) - 0|^2) \quad (5.5)$$

$$L_b = \frac{1}{N_b} \sum_{i=1}^{N_b} \left(\left| \frac{\partial \hat{C}_{RT}(\hat{x}_i, \hat{y}_i, \hat{t}_i)}{\partial n} - 0 \right|^2 \right) \quad (5.6)$$

$$L_f = \frac{1}{N_f} \sum_{i=1}^{N_f} (|f(\hat{x}_i, \hat{y}_i, \hat{t}_i)|^2) \quad (5.7)$$

Here, the loss L_{data} corresponds to the interior and boundary training data, N_d points (50% of the total mesh elements); the loss L_{in} corresponds to the inlet conditions, N_{in} points (all inlet points included); while L_f enforces the structure imposed by equation (5.1) at N_f collocation points (75% of the total mesh elements). The loss L_b corresponds to the zero flux boundary condition (wall and outlet), and ∂n indicates the direction of the outward-facing normal, such that $\partial \hat{C}_{RT} / \partial n$ is understood as the flux leaving the computational domain (all boundary points included). The optimisation of the

loss function and updating the learning parameters (weights and biases of the neural network) are performed using the ADAM and LBFGS optimisers [Mattey and Ghosh, 2022].

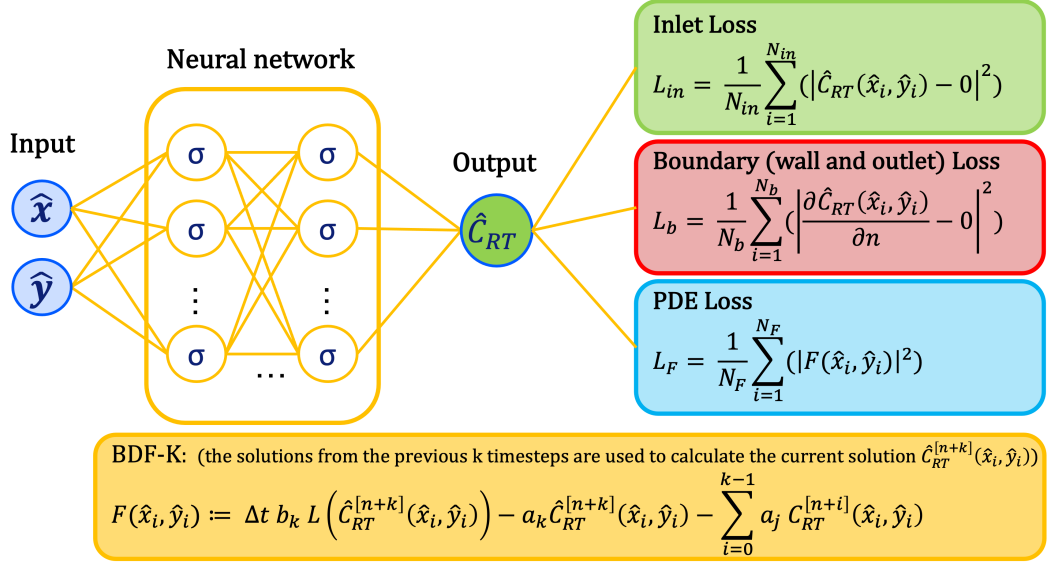


Figure 5.2: Basic overview of the backward differentiation formulae (BDF) physics-informed neural network (PINNs) used in this chapter, displaying network inputs, output, and the three loss components.

5.2.3 The Discrete-time PINNs Model

For the time marching, we consider the BDF methods as they show good accuracy and convergence properties [Calabrò et al., 2023]. Given

$$C_{RT}^{[0]}(x, y), C_{RT}^{[1]}(x, y), \dots, C_{RT}^{[k-1]}(x, y), \quad (5.8)$$

a k -step BDF applied to equation (5.1) can be written as

$$\Delta t b_k L(\hat{C}_{RT}^{[n+k]}(\hat{x}, \hat{y})) - a_k \hat{C}_{RT}^{[n+k]}(x, y) = \sum_{i=0}^{k-1} a_i C_{RT}^{[n+i]}(\hat{x}, \hat{y}), \quad (5.9)$$

$$L(\hat{C}_{RT}) = \frac{\partial \hat{C}_{RT}}{\partial t} = -(\mathbf{u} \cdot \nabla) \hat{C}_{RT} + D_{RT} \nabla^2 \hat{C}_{RT} + 1 \quad (5.10)$$

where L is an operator acting only on the spatial variables, Δt is the time-step size, $n = 0, 1, \dots$ and the coefficients $a_j, j = 0, \dots, k$, and b_k are listed in Table 5.1 for $k \leq 6$. It is worth noting that the 1-step BDF is the backward Euler method, and the BDF methods are not zero-stable for $k > 6$. Definitions and further details of BDF- k can be found in Calabrò et al. [2023], Wanner and Hairer [1996].

Table 5.1: Coefficients of the BDF methods.

k	a_6	a_5	a_4	a_3	a_2	a_1	a_0	b_k
1						1	-1	1
2					1	$-\frac{4}{3}$	$\frac{1}{3}$	$\frac{2}{3}$
3				1	$-\frac{18}{11}$	$\frac{9}{11}$	$-\frac{2}{11}$	$\frac{6}{11}$
4			1	$-\frac{48}{25}$	$\frac{36}{25}$	$-\frac{16}{25}$	$-\frac{3}{25}$	$\frac{12}{25}$
5		1	$-\frac{300}{137}$	$\frac{300}{137}$	$-\frac{200}{137}$	$\frac{75}{137}$	$-\frac{12}{137}$	$\frac{60}{137}$
6	1	$-\frac{360}{147}$	$\frac{450}{147}$	$-\frac{400}{147}$	$\frac{225}{147}$	$-\frac{72}{147}$	$\frac{10}{147}$	$\frac{60}{147}$

In the BDF- k -PINNs model, we use DNNs to approximate the solution of the PDE $\hat{C}_{RT}(\hat{x}, \hat{y})$ at each time-step by taking the spatial coordinates (\hat{x}, \hat{y}) as inputs, and the solutions from the previous k time-steps are also used to calculate the current solution $\hat{C}_{RT}^{[n+k]}(\hat{x}, \hat{y})$ (Fig. 5.2). The discrete-time PINNs model is used to solve a steady-state RT problem at each time-step. We define $F(\hat{x}, \hat{y})$ to be given by the left-hand side minus the right-hand side of equation (5.9):

$$F := \Delta t b_k L(\hat{C}_{RT}^{[n+k]}(\hat{x}, \hat{y})) - a_k \hat{C}_{RT}^{[n+k]}(\hat{x}, \hat{y}) - \sum_{i=0}^{k-1} a_i \hat{C}_{RT}^{[n+i]}(\hat{x}, \hat{y}), \quad (5.11)$$

The inlet concentrations of RT were set to zero. A zero flux boundary condition was adopted on the wall and outlet boundaries [Menichini and Xu, 2016]. The mean square error loss of the BDF- k -PINNs model is

$$Loss_{BDF} = L_{in} + L_b + L_F, \quad (5.12)$$

where

$$L_{in} = \frac{1}{N_{in}} \sum_{i=1}^{N_{in}} (|\hat{C}_{RT}(\hat{x}_i, \hat{y}_i) - 0|^2) \quad (5.13)$$

$$L_b = \frac{1}{N_b} \sum_{i=1}^{N_b} \left(\left| \frac{\partial \hat{C}_{RT}(\hat{x}_i, \hat{y}_i)}{\partial n} - 0 \right|^2 \right) \quad (5.14)$$

$$L_F = \frac{1}{N_F} \sum_{i=1}^{N_F} (|F(\hat{x}_i, \hat{y}_i)|^2) \quad (5.15)$$

Here, the loss L_{in} corresponds to the inlet condition (all inlet points included). The loss L_b corresponds to the zero flux boundary condition (all boundary points included) and the loss L_F represents the residual of the PDE equation (5.1) (75% of the mesh elements).

5.2.4 Activation Functions

In the literature, various activation functions, such as rectified linear units (ReLU) and tanh, are available. The choice of activation function often depends on the specific problem at hand [Chai et al., 2024]. ReLU-based multilayer perceptrons are commonly used in many PINNs architectures [Sitzmann et al., 2020]. However, ReLU networks may struggle with representing fine details in the underlying signals because ReLUs can not model higher-order derivatives; their second derivative is zero. As an alternative activation, tanh is capable of representing higher-order derivatives [Sitzmann et al., 2020]. However, Sitzmann et al. [2020] found that tanh’s derivatives are often not well-behaved and demonstrated that the periodic sine functions are well-suited for capturing complex signals. In this study, we tested both the hyperbolic tangent activation functions and the periodic sine activation functions.

Hyperbolic tangent has an output range of $[-1, 1]$ and is defined as follows [Zamanlooy and Mirhassani, 2013]:

$$\tanh(x) = \frac{e^x - e^{-x}}{e^x + e^{-x}} \quad (5.16)$$

The SIREN activation also has an output range of $[-1, 1]$ and is formulated as [Sitzmann et al., 2020]:

$$\phi(z) = \sin(w_0 \cdot z) \quad (5.17)$$

where $z = \mathbf{W}x + \mathbf{b}$ is the the linear transformation of the layer (weight matrix \mathbf{W} and bias \mathbf{b}), and w_0 is a hyperparameter controlling the frequency of the sine wave (commently set to values like 30 to enhance high-frequency signal modelling).

5.2.5 2D Channel Problem

The vascular segments at common sites for IAs (such as bifurcations of the Circle of Willis [Feng et al., 2023]) typically have length and diameter parameters in the millimetre range. For example, the mean length of the internal carotid artery (ICA) from the proximal cavernous segment to the ICA terminus was 33.1 ± 6.1 mm. The mean diameter at the cavernous ICA was 5 ± 0.6 mm [Rai et al., 2013]. Therefore, it is reasonable to set the length and width of the 2D channel as 20 mm and 10 mm, respectively.

In this experiment, we investigated the effect of flow on RT in a 2D rectangular domain by solving equation (5.1). The dimensionless computational domain for this 2D channel problem was defined as $\Omega = \{(x, y) | 0 \leq x \leq 2, 0 \leq y \leq 1\}$, with the left and right boundaries serving as the inlet and outlet, respectively, and the top and down boundaries acting as walls. The parabolic velocity field for the entire domain was computed using the Lattice Boltzmann method and then used as known variables in solving equation (5.1).

Equation (5.1) for the 2D channel was initially solved numerically using the backward-time-centered-space (BTCS) finite difference method (FDM) in MATLAB, providing a high-resolution RT dataset that was used both for training and as a reference for the PINNs code (Fig. 5.3). The numerical scheme employed in the computational domain Ω is as follows:

$$\frac{RT_{i,j}^{n+1} - RT_{i,j}^n}{\Delta t} + u_{i,j} \frac{RT_{i+1,j}^{n+1} - RT_{i-1,j}^{n+1}}{2\Delta x} + v_{i,j} \frac{RT_{i,j+1}^{n+1} - RT_{i,j-1}^{n+1}}{2\Delta y} = \quad (5.18)$$

$$D_{RT} \left(\frac{RT_{i+1,j}^{n+1} - 2RT_{i,j}^{n+1} + RT_{i-1,j}^{n+1}}{\Delta x^2} + \frac{RT_{i,j+1}^{n+1} - 2RT_{i,j}^{n+1} + RT_{i,j-1}^{n+1}}{\Delta y^2} \right) + 1 \quad (5.19)$$

where $\Delta t = 0.0001$ s, $\Delta x = \Delta y = 0.0001$ m, with 20,000 mesh elements in total.

For both the continuous-time PINNs and discrete-time PINNs models applied to the 2D channel problem, the chosen neural network architecture comprises 8 hidden layers, each with 20 neurons, and uses the tanh activation function. The ADAM [Kingma and

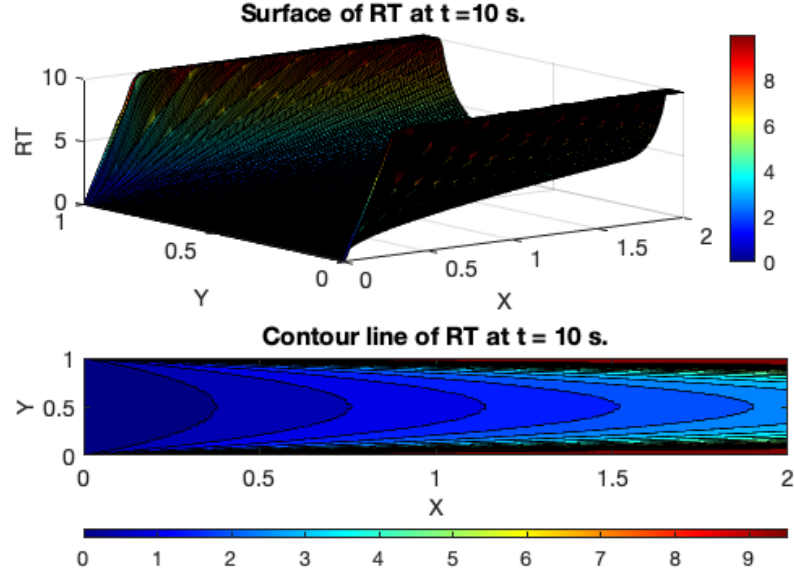


Figure 5.3: The reference of RT in 2D channel problem solved using the finite difference method (FDM).

[Ba, 2014] optimiser is employed with an initial learning rate of 1×10^{-4} , selected to be the highest possible value without causing divergence. The maximum number of epochs is set to 2000.

5.2.6 2D Idealised Aneurysm Problem

It has been shown that aneurysmal thrombus forms, or at least deposits, in regions of slow flow and low shear [Malaspinas et al., 2016, Ou et al., 2017, Rayz et al., 2008, Sarrami-Foroushani et al., 2017]. Consequently, CFD models often use blood flow stasis as a surrogate for thrombosis initiation mechanisms, with RT and SR being the most commonly used parameters in flow stasis-induced thrombosis models. Since the 2D channel geometry does not adequately represent a flow stasis environment, we further tested the discrete-time PINNs model with a 2D idealised aneurysm geometry (Fig. 5.4). In this setup, the left side serves as the inlet with a uniform velocity entrance of 0.1 m/s, while the right side acts as the outlet. We assumed a rigid wall with a no-slip boundary condition and prescribed a zero-pressure condition at the outlet. Both the

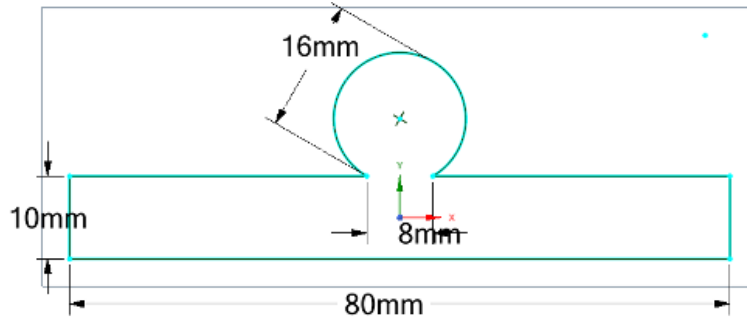


Figure 5.4: The 2D idealised aneurysm.

Navier-Stokes equations and the ADR equation (5.1) for RT were solved using ANSYS CFX. To discretise the computational domain, tetrahedral elements with a maximum edge size of 0.2 mm and five layers of prismatic elements with a maximum edge size of 0.1 mm were used (32,000 mesh elements in total).

Given our interest in assessing how PINNs perform in solving ADR equations, we turned off the fluid solver in ANSYS CFX after 8 cardiac cycles. ANSYS CFX includes an override parameter named ‘solve fluids’, which allows continuation with solving other equation groups, such as the ADR equations, once fluid convergence has been achieved. The fixed velocity field was then incorporated into the PINNs code as known variables, with the solution of equation (5.1) obtained from ANSYS CFX in the 2D idealised aneurysm serving as both initialisation data and a reference for the BDF-k-PINNs model.

5.3 Results

5.3.1 PINNs for RT in 2D Channel

In the continuous-time PINNs model, we utilised interior and boundary data from the FDM solution at $t = 1, 2, 3, \dots, 10$ s for training while also constraining the model with the PDE equation (5.1). As illustrated in Fig. 5.5, the results of the continuous-time PINNs model appear seemingly good for $t \leq 10$ s (within the training data range) but diverge rapidly when extended beyond this range ($t > 10$). The performance of the continuous-time PINNs model is highly dependent on the training data range, and it diverges significantly over time if no training data is provided beyond the initial

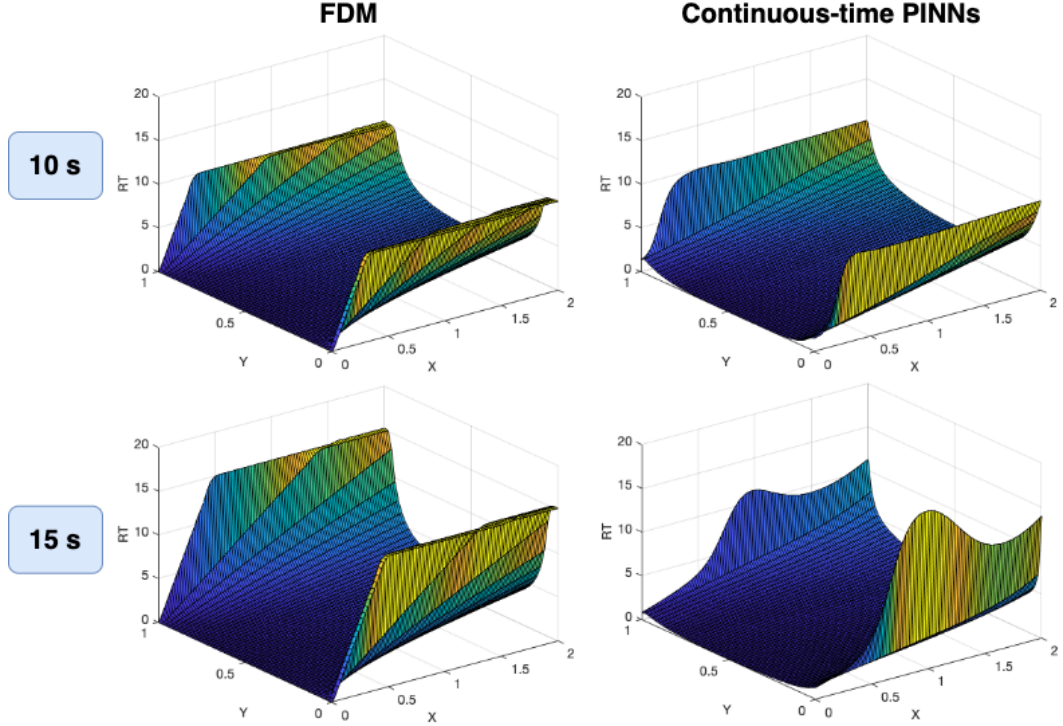


Figure 5.5: The continuous-time PINNs model for solving RT in 2D channel performed well with training data (≤ 10 s) but failed to predict the correct solution beyond the training data set (>10 s).

training data range. Given that our objective is to solve long-term solutions of the ADR equations, the continuous-time PINNs model (space-time method) is less appealing compared to the discrete-time PINNs model (time-stepping method).

We then applied the discrete-time PINNs model, specifically the BDF-1-PINNs model, to solve the RT in the 2D channel problem. The time-step size was set to 0.01 s, and the maximum number of epochs was set to 1000. For the BDF-1-PINNs model, the PINNs model was initialised solely with the FDM solution at $t = 5$ s. As shown in Fig. 5.6, the BDF-1-PINNs model performed effectively in solving the RT in the 2D channel, using only the FDM solution data from $t = 5$ s for initialisation. The BDF-1-PINNs model not only required less training data but also demonstrated better long-term stability compared to the continuous-time PINNs model (see Fig. 5.7).

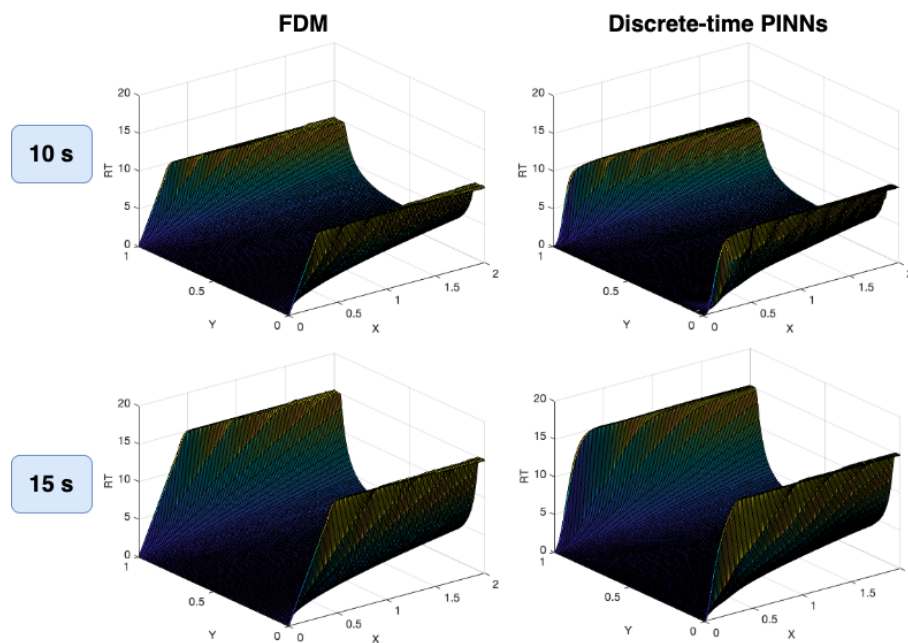


Figure 5.6: The BDF-1-PINNs model for solving RT in 2D channel showed good long-term stability. It successfully predicted the RT solution at $t = 15$ s while only initialised with the reference data at $t = 5$ s.

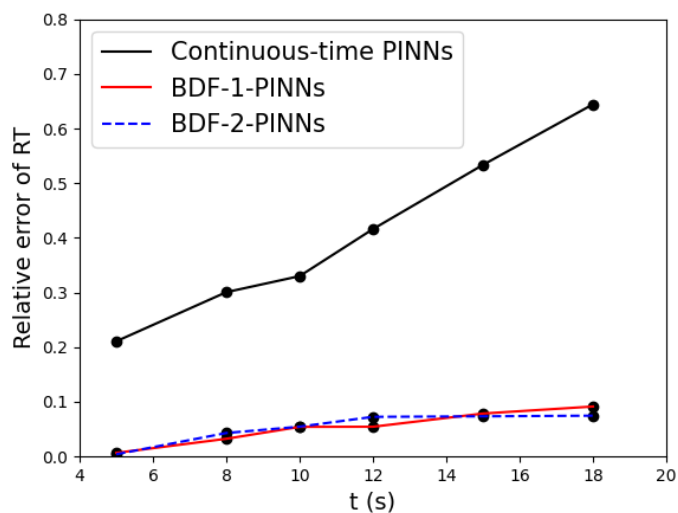


Figure 5.7: The relative errors of the PINNs model for solving RT in 2D channel. The RT reference solution was generated from the finite difference method (FDM).

5.3.2 PINNs for RT in 2D Idealised Aneurysm

For the BDF-k-PINNs model solving equation (5.1) in the 2D idealised aneurysm, the neural network architecture chosen comprises 6 hidden layers with 256 neurons in each layer. The time-step size was set to 0.01 s. The ADAM [Kingma and Ba, 2014] optimiser is employed with an initial learning rate of 1×10^{-4} , and with a maximum of 1000 epochs and early stopping after 100 epochs. Initially, the tanh activation function was used. Although tanh can represent higher-order derivatives, it often struggles with poorly behaved derivatives and fails to capture fine details [Sitzmann et al., 2020]. As illustrated in Fig. 5.8, while the BDF-1-PINNs model with tanh activation function successfully predicted the general distribution of RT, it did not capture finer details, particularly near the aneurysm wall.

To address this issue, we combined BDF-1 with SIREN [Sitzmann et al., 2020], a neural network architecture designed for implicit neural representations that employs sine as a periodic activation function. Unlike conventional nonlinearities such as the hyperbolic tangent or ReLU, the sine function is periodic and non-local. This periodic sine activation significantly enhances the representation of RT details in the 2D idealised aneurysm (Fig. 5.8) and reduces the relative errors (Fig. 5.9).

However, despite using BDF-1-SIREN or BDF-2-SIREN, the relative errors of the PINNs models still increase linearly with time, reaching more than 30% after 2 cardiac cycles. Fig. 5.10 shows how the errors accumulate over time, with ANSYS CFX results used as the reference.

5.4 Discussion

PINNs are a class of machine learning models where the governing PDE is incorporated into the neural network’s loss function [Raissi et al., 2019]. The standard PINNs approach trains the model to predict the solution at any point across the entire spatial-temporal domain, which corresponds to the continuous-time PINNs model used in this study [Mattey and Ghosh, 2022]. In contrast, the discrete-time PINNs models—particularly those incorporating the BDF technique—are less commonly explored [Calabrò et al., 2023]. However, the discrete-time PINNs models, employing a time-stepping method, are more attractive than the continuous-time PINNs models for

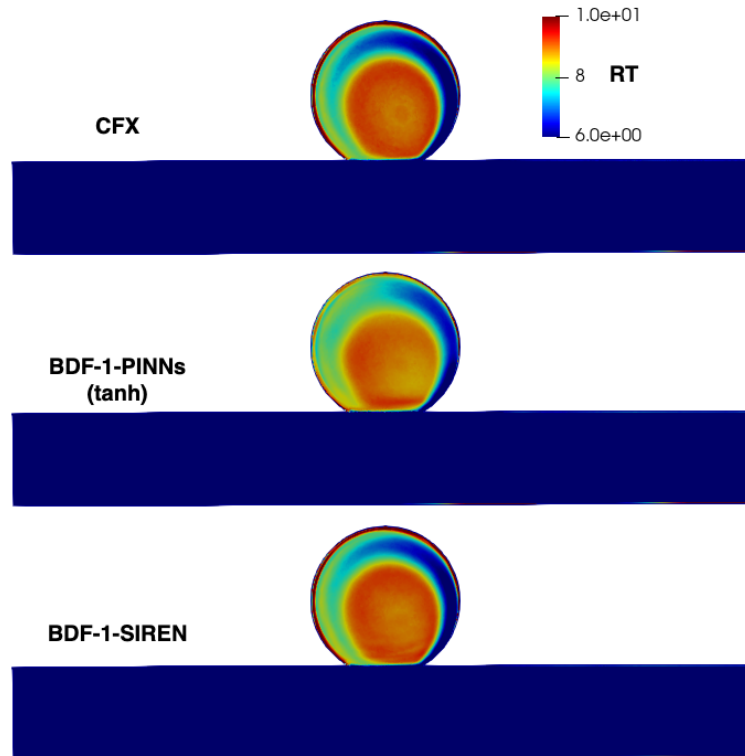


Figure 5.8: Comparison between the PINNs results with different activation functions and the ground truth calculated using ANSYS CFX at $t = 8$ s.

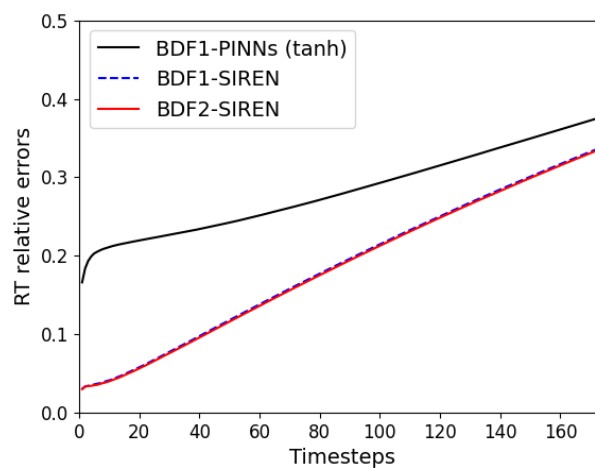


Figure 5.9: The relative errors of PINNs by using the CFX results as references in 2 cardiac cycles. The time-step size is 0.01s.

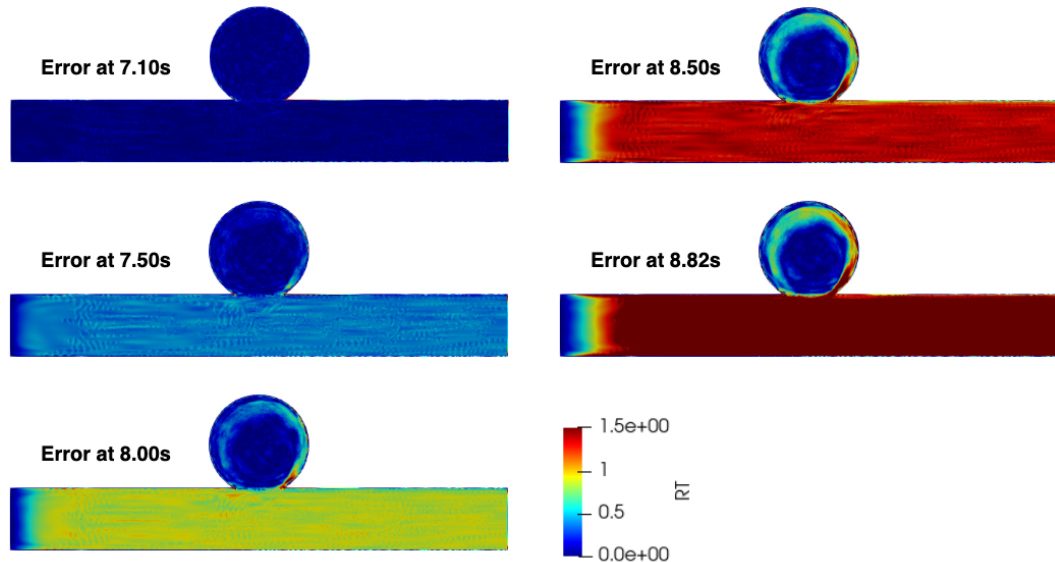


Figure 5.10: The absolute errors of BDF-1-SIREN by using the CFX results as references in 2 cardiac cycles.

solving long-term solutions of PDEs, as they do not require training data generation over time. In this study, we demonstrated that the BDF-PINNs models performed significantly better in solving ADR equations compared to standard continuous-time PINNs models. Specifically, in the 2D channel problem, the BDF-1-PINNs model exhibited superior accuracy and long-term stability compared to the continuous-time PINNs model (Fig. 5.7).

In this PINNs for solving ADR equations study, we focused on solving the ADR equations themselves rather than the flow field. The fixed velocity field was used as known variables when solving the ADR equations. Therefore, the approaches (e.g., finite difference method, Lattice Boltzmann method, ANSYS CFX, or any other effective numerical methods) we used for solving the velocity field would not affect how we solve the ADR equations. It's worth noting that the LBM codes used in the 2D channel problem were from my previously published work (which was not part of this research) [Liu et al., 2020] where I already demonstrated its effectiveness. The effectiveness of the ANSYS CFX method were also demonstrated in Chapter 3 and Chapter 4.

In our study, we observed that while tanh-based architectures performed adequately for solving RT in a 2D channel, they struggled to represent fine details in ADR equations within a 2D aneurysm model. In the 2D channel problem, the simplicity of both the

geometry and velocity distribution allowed even a basic BDF-PINNs architecture (with 8 layers and 20 neurons per layer) using the tanh activation function to capture the RT solution effectively. However, in the more complex 2D aneurysm scenario, the tanh activation function was insufficient for capturing the fine details of the RT solution. We then applied the BDF-SIREN architecture to the 2D idealised aneurysm problem and found that it performed significantly better than the BDF-PINNs (tanh) model in capturing fine details. However, even with the seemingly superior BDF-SIREN architecture, the relative errors of PINNs increased over time and could exceed 30% after two cardiac cycles (Fig. 5.9).

According to the expert's guide to training PINNs [Wang et al., 2023], we have appropriately set the PINNs architecture and demonstrated its capability in solving the RT in a 2D channel (Fig. 5.6 and Fig. 5.7). In addition to the PINNs architecture and optimisation strategies, the most common sources of the error accumulation in PINNs when solving RT in 2D aneurysms are the numerical discretisation of the ADR equation (both time and spatial discretisation) and the implementation of boundary conditions. The identical relative errors observed in the BDF-1-PINNs and BDF-2-PINNs models for both the 2D channel and 2D idealised aneurysm problems suggest that the BDF-1 scheme is capable enough for these relatively simple 2D problems. The increase in error over time can then likely be attributed to the spatial discretisation or boundary conditions. To discretise the computational domain, tetrahedral elements with a maximum edge size of 0.2 mm and five layers of prismatic elements with a maximum edge size of 0.1 mm were used. Mesh independence was confirmed for these element sizes in our previous studies [Liu et al., 2023, Sarrami-Foroushani et al., 2019]. Therefore, the error accumulation over time is most likely related to boundary conditions in the PINNs model (Fig. 5.10). The discrete-time PINNs model was initialised with the ANSYS CFX solutions at the 8th cardiac cycle (7.06 s). As shown in Fig. 5.10, the error was tiny at 7.10 s but then accumulated from the inlet and wall boundaries. The zero RT concentration condition at the inlet only weakly constrained the inlet areas, and then the errors spread from the wall to the internal points of the vessel. The highest errors were observed around the neck of the 2D aneurysm, where the nearby wall geometry is sharp. This suggests that boundary conditions may be a significant factor in the error accumulation over time.

This issue may be common for PINNs models dealing with nonlinear and higher-

order time-varying PDEs [Mattey and Ghosh, 2022]. Mattey and Ghosh [2022] proposed backward-compatible PINNs (bc-PINNs) to address such issues. The key idea of bc-PINNs is to re-train the same neural network for solving PDEs over successive time segments while satisfying the already obtained solutions for previous time segments. The bc-PINNs model was tested on 1D or 2D (square geometry) Allen-Cahn and Cahn-Hilliard equations [Mattey and Ghosh, 2022]. However, it remains to be investigated whether this approach can be applied to our BDF-SIREN architecture for solving ADR equations and how to improve the long-term stability of PINNs. Our BDF-SIREN model performed well in the 2D channel problem but diverged more rapidly in the 2D aneurysm problem, which features a more complex geometry compared with the 2D channel. Further exploration is needed to address these challenges.

As mentioned before, the transport of biochemical species involved in the thrombus formation process is described using ADR equations; therefore, the long-term stability of the BDF-SIREN architecture in solving ADR equations is of great importance. The next step, based on this study, is to improve the accuracy and long-term stability of the BDF-SIREN architecture in solving ADR equations. Once the long-term stability issue is addressed, we can further investigate how to build a PINNs-based full thrombosis model to accelerate the thrombus formation simulation workflow, leveraging the following advantages of the BDF-SIREN architecture: (1) The PINNs architecture is mesh-less. As a result, although we still need to define a set of collocation points in the domain where the PDEs and boundary conditions are enforced, these points can be distributed more flexibly than in traditional mesh-based methods. For example, the collocation points can be concentrated in regions with high gradients or near boundaries to improve accuracy. (2) The BDF time-marching scheme is more stable than other classic methods, such as the forward Euler method. Therefore, we can use a larger time-step size in the BDF-SIREN architecture. and (3) We can treat the flow field as a constant flow in each cardiac cycle (updating the Darcy term for modelling the fluid-structure interaction between the flow and the formed thrombus every cardiac cycle rather than every small time-step) and focus on the biochemical reactions at each time-step. Currently, the coupling between the Navier-Stokes equations and the other eight ADR equations is modelled at every time step [Sarrami-Foroushani et al., 2019].

In this way, we might be able to accelerate the thrombus formation modelling workflow by utilising the power of PINNs and GPUs.

5.4.1 Conclusion

In this simplified PINNs-based analogue to the full thrombosis model, we demonstrated that the discrete-time PINNs model (the BDF-1-PINNs) outperformed the standard continuous-time PINNs model in solving ADR equations. Although the tanh activation function is often considered a good alternative to the classic ReLU function for representing higher-order derivatives, we found that the tanh-based architecture was unable to capture the fine details of RT in the 2D aneurysm model. The BDF-SIREN architecture, which uses the sine function as the activation function, was able to capture finer details than the tanh-based architecture in solving ADR equations. However, errors grew over time for all the above PINNs models, which may be due to the implementation of boundary conditions in PINNs. Reducing PINNs errors and improving the long-term stability of PINNs in solving ADR equations require further investigation.

CHAPTER 6

Conclusions and Outlook

6.1 Conclusions

The motivation behind this thesis is to enhance both the credibility and efficiency of patient-specific computational thrombosis modelling by addressing its critical tasks, including workflow automation and acceleration, calibration and sensitivity analysis, and validation. The main contributions of the thesis are outlined as follows:

- Fully automated the volume meshing and post-processing components, improved virtual coiling for wide-neck aneurysms and narrowed the thrombosis initiation to near-wall regions for untreated IAs.
- Conducted a systematic review of ST reported in clinical studies, calibrated the haemodynamic thresholds of thrombosis initiation and explored the influence of hypertension in ST.
- Assessed the impact of various model parameters on the final formed thrombus composition and further validated the thrombosis model using clinical data from real patients.
- Investigated the acceleration of the thrombus formation modelling workflow by utilising the power of PINNs and GPUs.

6.2 Outlook

In this thesis, I contributed to the creation of a fully automatic haemodynamics and thrombosis modelling workflow, calibrated the key haemodynamic thresholds for thrombosis initiation, identified the most significant factors in aneurysmal thrombosis modelling, validated our thrombosis model based on a real patient case, and investigated physics-informed deep learning models of thrombus formation. While I have made noteworthy strides and achieved promising outcomes in these areas, certain challenges and promising future directions remain that require further attention to advance haemodynamics and thrombosis modelling in IAs.

Enhance the thrombosis trigger mechanism to enable more accurate thrombosis modelling. One of the most challenging aspects of aneurysmal thrombosis modelling is accurately describing the trigger mechanism. In this thesis, we as-

sumed that thrombus formation in the aneurysm sac was primarily triggered by blood flow stasis, using high RT and low SR to characterise this stasis. However, the literature indicates that cerebral aneurysm thrombosis is also associated with factors such as endothelial damage in the aneurysm sac, wall inflammation, blood-borne tissue factors, and contact with artificial surfaces following treatment. Incorporating these additional trigger mechanisms, such as device-induced thrombosis initiation, could potentially lead to more accurate predictions of thrombus formation in aneurysms.

Conduct large-scale validation studies across multiple patients to enhance model credibility. In Chapter 4, I demonstrated that our thrombosis model can effectively predict thrombus formation both before and after treatment based on a single clinical patient case. However, this validation was limited to just one patient. To ensure that the computational thrombosis model is robust and reliable for potential clinical use in the future, extensive validation studies across multiple patients are necessary to build greater confidence in the model.

Accelerate thrombosis modelling to reduce the computational cost of post-treatment simulations. Our thrombosis model is currently very time-consuming; for instance, simulating thrombosis in a post-treatment aneurysm (as discussed in Chapter 4, a clinical case treated with a flow diverter and 10 coils) can take up to 2 months on a 128-core computer. As mentioned in Chapter 5, the primary reasons for this high computational cost are: (1) the large mesh size; (2) the fluid-structure interaction between blood flow and the formed thrombus at each time step; and (3) the very small time-step size.

Firstly, the significant difference in length scales between the flow-diverter wires ($\approx 30 \mu\text{m}$) and the arterial diameters ($\approx 5 \text{mm}$) necessitates a high mesh resolution to produce a grid with sufficient quality around the wires when modelling the virtual device explicitly. Further investigation into simplifying the virtual device modelling using alternative methods (e.g., the porous media method or the immersed boundary method) may accelerate post-treatment thrombosis modelling. However, the effectiveness of these methods in medical device modelling needs to be demonstrated first.

Secondly, as discussed in Chapter 5, the BDF-SIREN architecture has unique advantages compared to ANSYS CFX. The next steps based on the current BDF-SIREN results are: (1) determine exactly why the BDF-SIREN error accumulates over time;

(2) explore whether the key idea of bc-PINNs can be applied to ADR equations to reduce errors; (3) investigate other literature methods to improve the long-term stability of PINNs in solving ADR equations; and (4) subsequently, develop a full thrombosis modelling workflow based on PINNs.

Investigate clinically relevant questions using our workflow. For example, we aim to explore why some aneurysms rupture after seemingly successful flow-diverter treatment. Although flow diverter is a safe and effective modality, some patients can experience delayed aneurysmal rupture [Brinjikji et al., 2013]. The reported incidence of rupture varies significantly between different centres, such as 11.4%(5/44) [Roy et al., 2017] or 0.6%(5/793) [Kallmes et al., 2015] after flow-diverter treatment. Even in cases of complete occlusion, delayed rupture occurs in nearly 2% of cases [Brinjikji et al., 2013]. However, the mechanism behind this delayed rupture remains unknown.

Past studies have identified several possible risk factors [Hou et al., 2020]: (1) increased intra-aneurysmal pressure after flow-diverter treatment; (2) partial formation of intra-aneurysmal thrombi (97.3%(36/37)); though it is still a mystery why thrombus may lead to permanent cure in some patients but trigger future delayed rupture in others; (3) large and giant aneurysms (88.7%); (4) symptomatic aneurysms (97.8%); (5) saccular aneurysms with high aspect ratio (> 1.6); (6) delayed flow-diverter migration into the aneurysm sac; and (7) mechanical injury by flow-diverter.

As shown in Fig. 6.1, we designed a study titled ‘An in silico investigation into the mechanism of delayed rupture after flow-diverter treatment’ to examine why some aneurysms rupture after flow-diverter treatment. This study compares aneurysm morphology (size and aspect ratio), haemodynamics (pressure change and flow reduction), and thrombus formation (thrombosed region and thrombus composition) between the delayed rupture and complete occlusion groups. Out of 145 cases collected from Leeds General Infirmary, we found 61 complete occlusion cases but only 3 delayed rupture cases. Our research team is now collaborating with more clinical centres across the UK to collect additional clinical cases. This study will be finalised once we have gathered a sufficient number of delayed rupture cases.

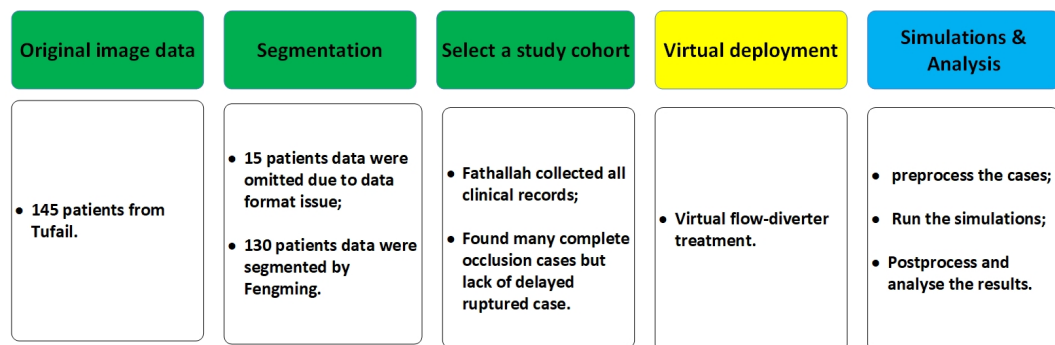


Figure 6.1: Workflow for investigating the mechanism of delayed rupture. Green labels indicate that they have been completed, yellow labels indicate that they are in progress, and blue labels indicate that they will be completed in the future. My main contributions to this delayed rupture study were as follows: (1) background research and study design; (2) collection of clinical image data and verification of segmentation results; (3) selection of the study cohort and virtual deployment of FD.

APPENDIX A

List of Publications

A.1 Journal paper

1. **Liu Q**, Sarrami-Foroushani A, Wang Y, MacRaid M, Kelly C, Lin F, Xia Y, Song S, Ravikumar N, Patankar T, Taylor ZA. Hemodynamics of thrombus formation in intracranial aneurysms: An in silico observational study. *APL bioengineering*. 2023 Sep 1;7(3). (Editor's pick).

2. **Liu Q**, Lassila T, Lin F, MacRaid M, Patankar T, Islim F, Song S, Xu H, Chen X, Taylor ZA, Sarrami-Foroushani A, Frangi AF. Key influencers in an aneurysmal thrombosis model: A sensitivity analysis and validation study. *APL bioengineering*. 2025. (Editor's pick).

3. MacRaid M, Sarrami-Foroushani A, Song S, **Liu Q**, Kelly C, Ravikumar N, Patankar T, Lassila T, Taylor ZA, Frangi AF. Off-label in-silico flow diverter performance assessment in posterior communicating artery aneurysms. *Journal of NeuroInterventional Surgery*. 2024.

4. **Liu Q**, Lassila T, Nie L, Shone F, MacRaid M, Taylor ZA, Sarrami-Foroushani A, Frangi AF. Time discretisation in the solution of advection-diffusion-reaction equations with PINNs. *Bioengineering & Translational Medicine*. 2025. (Under review).

A.2 Conference paper

1. Lin F, Xia Y, Ravikumar N, **Liu Q**, MacRaid M, Frangi AF. Adaptive semi-supervised segmentation of brain vessels with ambiguous labels. *International Conference on Medical Image Computing and Computer-Assisted Intervention 2023 Oct 8* (pp. 106-116). Cham: Springer Nature Switzerland.

2. Lin, F., Xia, Y., MacRaid, M., Deo, Y., Dou, H., **Liu, Q.**, ... & Frangi, A. F.. Unsupervised Domain Adaptation for Brain Vessel Segmentation through Transwarp Contrastive Learning. *IEEE International Symposium on Biomedical Imaging (ISBI 2024)*.

3. Lin, F., Xia, Y., MacRaid, M., Deo, Y., Dou, H., **Liu, Q.**, ... & Frangi, A. F.. Gs-ema: Integrating Gradient Surgery Exponential Moving Average with Boundary-Aware Contrastive Learning for Enhanced Domain Generalization in Aneurysm Segmentation. *IEEE International Symposium on Biomedical Imaging (ISBI 2024)*.

A.3 Conference abstract

1. **Liu Q**, Sarrami-Foroushani A, Wang Y, MacRaid M, Kelly C, Lin F, Xia Y, Song S, Ravikumar N, Patankar T, Taylor ZA. In-silico calibration of thrombosis models using clinical incidence rates of spontaneous thrombosis in intracranial aneurysms. Virtual Physiological Human (VPH) conference, Porto, Portugal, 2022.

2. **Liu Q**, Lassila T, Lin F, MacRaid M, Patankar T, Islim F, Song S, Xu H, Chen X, Taylor ZA, Sarrami-Foroushani A, Frangi AF. Hemodynamics of thrombus formation in intracranial aneurysms: an in silico observational study. 10th International Biofluid & Mechanobiology Symposium (IBMS 10), ISRAEL, 2024.

3. **Liu Q**, Sarrami-Foroushani A, Wang Y, MacRaid M, Kelly C, Lin F, Xia Y, Song S, Ravikumar N, Patankar T, Taylor ZA. How common is spontaneous thrombus formation in intracranial aneurysms? An in-silico observational study calibrated against clinical prevalence data. 24th Virtual Imaging Trials In Medicine (VITM 24), Durham, the United States, 2024.

APPENDIX B

Biosketch



Qiongyao Liu was born in Hunan province, China, in 1992. He received his B.Sc. degree in Material Forming and Control Engineering from Nanchang University in 2015 and his M.Sc. degree in Biomedical Engineering from Beijing Institute of Technology in 2018. During his master's degree, Qiongyao accelerated the immersed boundary and Lattice Boltzmann method (IB-LBM) more than 30 times using GPU-CUDA. Building on this, he constructed a simulation system for cell movement based on GPU-CUDA and IB-LBM.

In October 2020, he joined the Centre for Computational Imaging and Simulation Technologies in Biomedicine (CISTIB) at the School of Computing, University of Leeds, as a PhD student, under the supervision of Professor Alejandro F. Frangi, Dr Ali Sarrami-Foroushani, Dr Toni Lassila, Dr Zeike A. Taylor, Dr Yongxing Wang, and Dr Nishant Ravikumar. He was awarded a School of Computing Full-Time Fees and Maintenance PhD Scholarship to support his research in CISTIB.

The main aim of his PhD project has been to improve both the reliability and efficiency of patient-specific computational thrombosis modelling. He has contributed to creating a fully automatic haemodynamics and thrombosis modelling workflow, calibrating the key haemodynamic thresholds of thrombosis initiation, identifying the most significant factors in aneurysmal thrombosis modelling, validating the thrombosis model using real patient data, and exploring physics-informed deep learning models of thrombus formation. A complete list of his publications is available at Google Scholar

(<https://scholar.google.com/citations?user=qnYpQQEAAAAJ&hl=en&oi=ao>).

Research interests: His main research interests include computational fluid dynamics, haemodynamics and thrombosis modelling, in silico trials, physics-informed deep learning models, and immersed boundary and Lattice Boltzmann method (IB-LBM).

REFERENCES

- S Hassan Akbari, Matthew R Reynolds, Yasha Kadkhodayan, DeWitte T Cross, and Christopher J Moran. Hemorrhagic complications after prasugrel (effient) therapy for vascular neurointerventional procedures. *Journal of neurointerventional surgery*, 5(4):337–343, 2013.
- Fawaz Al-Mufti, Eric R Cohen, Krishna Amuluru, Vikas Patel, Mohammad El-Ghanem, Rolla Nuoman, Neil Majmundar, Neha S Dangayach, and Philip M Meyers. Bailout strategies and complications associated with the use of flow-diverting stents for treating intracranial aneurysms. *Interventional Neurology*, 8(1):38–54, 2020.
- Ronald A Alberico, Mahendra Patel, Sean Casey, Betsy Jacobs, William Maguire, and Robert Decker. Evaluation of the circle of willis with three-dimensional ct angiography in patients with suspected intracranial aneurysms. *American journal of neuroradiology*, 16(8):1571–1578, 1995.
- Vandenbulcke Alberto, Messerer Mahmoud, Starnoni Daniele, Puccinelli Francesco, Daniel Roy Thomas, and Cossu Giulia. Complete spontaneous thrombosis in unruptured non-giant intracranial aneurysms: a case report and systematic review. *Clinical Neurology and Neurosurgery*, page 106319, 2020.
- M Anand, K Rajagopal, and KR Rajagopal. A model incorporating some of the mechanical and biochemical factors underlying clot formation and dissolution in flowing blood. *Journal of Theoretical Medicine*, 5(3-4):183–218, 2003.
- M Anand, K Rajagopal, and KR Rajagopal. A model for the formation and lysis of blood clots. *Pathophysiology of haemostasis and thrombosis*, 34(2-3):109–120, 2006.
- M Anand, K Rajagopal, and KR Rajagopal. A model for the formation, growth, and

- lysis of clots in quiescent plasma. a comparison between the effects of antithrombin iii deficiency and protein c deficiency. *Journal of theoretical biology*, 253(4):725–738, 2008.
- Saltelli Andrea, Ratto Marco, Andres Terry, Campolongo Francesca, Cariboni Jessica, Gatelli Debora, Saisana Michaela, and T Stefano. Global sensitivity analysis: the primer. *Ist ed., John Wiley & Sons, The Atrium, Southern Gate, Chichester, England*, 2008.
- Sunil Appanaboyina, Fernando Mut, Rainald Löhner, Christopher Putman, and Juan Cebal. Simulation of intracranial aneurysm stenting: techniques and challenges. *Computer Methods in Applied Mechanics and Engineering*, 198(45-46):3567–3582, 2009.
- H Artmann, D Vonofakos, H Müller, and H Grau. Neuroradiologic and neuropathologic findings with growing giant intracranial aneurysm. review of the literature. *Surgical neurology*, 21(4):391–401, 1984.
- M Haithem Babiker, Brian Chong, L Fernando Gonzalez, Sachmanik Cheema, and David H Frakes. Finite element modeling of embolic coil deployment: multifactor characterization of treatment effects on cerebral aneurysm hemodynamics. *Journal of biomechanics*, 46(16):2809–2816, 2013.
- Ralf W Baumgartner, Heinrich P Mattle, Karl Kothbauer, and Gerhard Schroth. Transcranial color-coded duplex sonography in cerebral aneurysms. *Stroke*, 25(12):2429–2434, 1994.
- Atilim Gunes Baydin, Barak A Pearlmutter, Alexey Andreyevich Radul, and Jeffrey Mark Siskind. Automatic differentiation in machine learning: a survey. *Journal of machine learning research*, 18(153):1–43, 2018.
- Tibor Becske, David F Kallmes, Isil Saatci, Cameron G McDougall, István Szikora, Giuseppe Lanzino, Christopher J Moran, Henry H Woo, Demetrius K Lopes, Aaron L Berez, et al. Pipeline for uncoilable or failed aneurysms: results from a multicenter clinical trial. *Radiology*, 267(3):858–868, 2013.
- AS Bedekar, K Pant, Yiannis Ventikos, and S Sundaram. A computational model combining vascular biology and haemodynamics for thrombosis prediction in anatomic-

-
- ally accurate cerebral aneurysms. *Food and bioproducts processing*, 83(2):118–126, 2005.
- Philipp Berg, Samuel Voß, Sylvia Saalfeld, Gábor Janiga, Aslak W Bergersen, Kristian Valen-Sendstad, Jan Bruening, Leonid Goubergrits, Andreas Spuler, Nicole M Cancelliere, et al. Multiple aneurysms anatomy challenge 2018 (match): phase i: segmentation. *Cardiovascular engineering and technology*, 9:565–581, 2018.
- Marco Bianchetti, Sergei Kucherenko, and Stefano Scoleri. Pricing and hedging multi-asset options with high-dimensional quasi monte carlo: Fd vs aad greeks. *New Frontiers in Practical Risk Management*, 3(10):7–28, 2016.
- Saykat Kumar Biswas and NK Anand. Three-dimensional laminar flow using physics informed deep neural networks. *Physics of Fluids*, 35(12), 2023.
- Jacoline Boluijt, Joost CM Meijers, Gabriel JE Rinkel, and Mervyn DI Vergouwen. Hemostasis and fibrinolysis in delayed cerebral ischemia after aneurysmal subarachnoid hemorrhage: a systematic review. *Journal of Cerebral Blood Flow & Metabolism*, 35(5):724–733, 2015.
- TJ Bowker, PN Watton, PE Summers, JV Byrne, and Y Ventikos. Rest versus exercise hemodynamics for middle cerebral artery aneurysms: a computational study. *American journal of neuroradiology*, 31(2):317–323, 2010.
- Francesco Briganti, Giuseppe Leone, Mariano Marseglia, Giuseppe Mariniello, Ferdinando Caranci, Arturo Brunetti, and Francesco Maiuri. Endovascular treatment of cerebral aneurysms using flow-diverter devices: a systematic review. *The neuroradiology journal*, 28(4):365–375, 2015.
- W Brinjikji, G Lanzino, HJ Cloft, AH Siddiqui, E Boccardi, S Cekirge, D Fiorella, R Hanel, P Jabbour, E Levy, et al. Risk factors for ischemic complications following pipeline embolization device treatment of intracranial aneurysms: results from the intreped study. *American Journal of Neuroradiology*, 37(9):1673–1678, 2016.
- Waleed Brinjikji, Mohammad H Murad, Giuseppe Lanzino, Harry J Cloft, and David F Kallmes. Endovascular treatment of intracranial aneurysms with flow diverters: a meta-analysis. *Stroke*, 44(2):442–447, 2013.

-
- Richard D Brownlee, Bruce I Tranmer, Robert J Sevick, Grigory Karmy, and Bernadette J Curry. Spontaneous thrombosis of an unruptured anterior communicating artery aneurysm: an unusual cause of ischemic stroke. *Stroke*, 26(10):1945–1949, 1995.
- R Bruening, S Mueller-Schunk, D Morhard, KC Seelos, H Brueckmann, R Schmid-Elsaesser, A Straube, and TE Mayer. Intraprocedural thrombus formation during coil placement in ruptured intracranial aneurysms: treatment with systemic application of the glycoprotein iib/iiia antagonist tirofiban. *American Journal of Neuroradiology*, 27(6):1326–1331, 2006.
- Joseph D Burns and Robert D Brown. Treatment of unruptured intracranial aneurysms: surgery, coiling, or nothing? *Current neurology and neuroscience reports*, 9(1):6–12, 2009.
- James V Byrne and István Szikora. Flow diverters in the management of intracranial aneurysms: a review. *EJMINT Original Article*, 1225000057:29, 2012.
- Shengze Cai, Zhiping Mao, Zhicheng Wang, Minglang Yin, and George Em Karniadakis. Physics-informed neural networks (pinns) for fluid mechanics: A review. *Acta Mechanica Sinica*, 37(12):1727–1738, 2021.
- Francesco Calabrò, Salvatore Cuomo, Daniela di Serafino, Giuseppe Izzo, and Eleonora Messina. Time discretization in the solution of parabolic pdes with anns. *Applied Mathematics and Computation*, 458:128230, 2023.
- Juan R Cebral, Fernando Mut, Marcelo Raschi, Simona Hodis, Y-H Ding, Bradley J Erickson, Ramanathan Kadirvel, and David F Kallmes. Analysis of hemodynamics and aneurysm occlusion after flow-diverting treatment in rabbit models. *American Journal of Neuroradiology*, 35(8):1567–1573, 2014.
- Xintao Chai, Zhiyuan Gu, Hang Long, Shaoyong Liu, Taihui Yang, Lei Wang, Fenglin Zhan, Xiaodong Sun, and Wenjun Cao. Modeling multisource multifrequency acoustic wavefields by a multiscale fourier feature physics-informed neural network with adaptive activation functions. *Geophysics*, 89(3):T79–T94, 2024.
- E Thomas Chappell, Federico Castro Moure, and Matthew C Good. Comparison of

- computed tomographic angiography with digital subtraction angiography in the diagnosis of cerebral aneurysms: a meta-analysis. *Neurosurgery*, 52(3):624–631, 2003.
- Manash S Chatterjee, Jeremy E Purvis, Lawrence F Brass, and Scott L Diamond. Pairwise agonist scanning of human platelets reveals the high-dimensional calcium response to combinatorial mediators of thrombosis. *Nature biotechnology*, 28(7):727, 2010.
- Salvatore Cito, Marco Domenico Mazzeo, and Lina Badimon. A review of macroscopic thrombus modeling methods. *Thrombosis research*, 131(2):116–124, 2013.
- José E Cohen, Gustavo Rajz, Felix Umansky, and Sergey Spektor. Thrombosis and recanalization of symptomatic nongiant saccular aneurysm. *Neurological research*, 25(8):857–859, 2003.
- José E Cohen, Eyal Yitshayek, John Moshe Gomori, Savvas Grigoriadis, Guy Raphaeli, Sergei Spektor, and Gustavo Rajz. Spontaneous thrombosis of cerebral aneurysms presenting with ischemic stroke. *Journal of the neurological sciences*, 254(1-2):95–98, 2007.
- Robert W Colman. Are hemostasis and thrombosis two sides of the same coin? *The Journal of experimental medicine*, 203(3):493–495, 2006.
- Daniel Ribeiro de Sousa, Carolina Vallecilla, Kamil Chodzynski, Ricardo Corredor Jerez, Orestis Malaspinas, Omer Faruk Eker, Rafik Ouared, Luc Vanhamme, Alexandre Legrand, Bastien Chopard, et al. Determination of a shear rate threshold for thrombus formation in intracranial aneurysms. *Journal of neurointerventional surgery*, 8(8):853–858, 2016.
- Orlando Diaz and Leonardo Rangel-Castilla. Endovascular treatment of intracranial aneurysms. *Handbook of clinical neurology*, 136:1303–1309, 2016.
- Lu Feng, He-Jiao Mao, Ding-Ding Zhang, Yi-Cheng Zhu, and Fei Han. Anatomical variations in the circle of willis and the formation and rupture of intracranial aneurysms: A systematic review and meta-analysis. *Frontiers in Neurology*, 13:1098950, 2023.
- Sandra P Ferns, Marieke ES Sprengers, Willem Jan van Rooij, Gabriel JE Rinkel, Jeroen C van Rijn, Shandra Bipat, Menno Sluzewski, and Charles BLM Majoie. Coil-

- ing of intracranial aneurysms: a systematic review on initial occlusion and reopening and retreatment rates. *Stroke*, 40(8):e523–e529, 2009.
- N Filipovic, Milos Kojic, and A Tsuda. Modelling thrombosis using dissipative particle dynamics method. *Philosophical Transactions of the Royal Society A: Mathematical, Physical and Engineering Sciences*, 366(1879):3265–3279, 2008.
- Sebastian Fischer, Zsolt Vajda, Marta Aguilar Perez, Elisabeth Schmid, Nikolai Hopf, Hansjörg Bätzner, and Hans Henkes. Pipeline embolization device (ped) for neurovascular reconstruction: initial experience in the treatment of 101 intracranial aneurysms and dissections. *Neuroradiology*, 54(4):369–382, 2012.
- Matthew H Flamm, Thomas V Colace, Manash S Chatterjee, Huiyan Jing, Songtao Zhou, Daniel Jaeger, Lawrence F Brass, Talid Sinno, and Scott L Diamond. Multiscale prediction of patient-specific platelet function under flow. *Blood, The Journal of the American Society of Hematology*, 120(1):190–198, 2012.
- Food, Drug Administration, et al. Assessing the credibility of computational modeling and simulation in medical device submissions. *Draft Guidance for Industry and Food and Drug Administration Staff. Silver Spring, MD, USA: Food and Drug Administration*, 2021.
- Matthew D Ford, Noam Alperin, Sung Hoon Lee, David W Holdsworth, and David A Steinman. Characterization of volumetric flow rate waveforms in the normal internal carotid and vertebral arteries. *Physiological measurement*, 26(4):477, 2005.
- Soichiro Fujimura, Hiroyuki Takao, Takashi Suzuki, Chihebeddine Dahmani, Toshihiro Ishibashi, Hiroya Mamori, Makoto Yamamoto, and Yuichi Murayama. Hemodynamics and coil distribution with changing coil stiffness and length in intracranial aneurysms. *Journal of neurointerventional surgery*, 10(8):797–801, 2018.
- AJ Geers, Ignacio Larrabide, Alessandro Guido Radaelli, Hrvoje Bogunovic, Minsuok Kim, HAF Gratama Van Andel, CB Majoie, E VanBavel, and AF Frangi. Patient-specific computational hemodynamics of intracranial aneurysms from 3d rotational angiography and ct angiography: an in vivo reproducibility study. *American Journal of Neuroradiology*, 32(3):581–586, 2011.

-
- AJ Geers, I Larrabide, HG Morales, and AF Frangi. Approximating hemodynamics of cerebral aneurysms with steady flow simulations. *Journal of biomechanics*, 47(1):178–185, 2014.
- K Gester, I Lüchtefeld, M Büsen, SJ Sonntag, T Linde, U Steinseifer, and G Cattaneo. In vitro evaluation of intra-aneurysmal, flow-diverter-induced thrombus formation: a feasibility study. *American Journal of Neuroradiology*, 37(3):490–496, 2016.
- Federico Ghirelli and Bo Leckner. Transport equation for the local residence time of a fluid. *Chemical engineering science*, 59(3):513–523, 2004.
- Peter LA Giesen, Ursula Rauch, Bernd Bohrmann, Dorothee Kling, Merce Roqué, John T Fallon, Juan J Badimon, Jacques Himber, Markus A Riederer, and Yale Nemerson. Blood-borne tissue factor: another view of thrombosis. *Proceedings of the National Academy of Sciences*, 96(5):2311–2315, 1999.
- Marco Goeijenbier, M Van Wissen, C Van De Weg, Eefje Jong, VEA Gerdes, JCM Meijers, DPM Brandjes, and ECM van Gorp. Viral infections and mechanisms of thrombosis and bleeding. *Journal of medical virology*, 84(10):1680–1696, 2012.
- N Gorring, L Kark, A Simmons, and T Barber. Determining possible thrombus sites in an extracorporeal device, using computational fluid dynamics-derived relative residence time. *Computer methods in biomechanics and biomedical engineering*, 18(6):628–634, 2015.
- Guido Guglielmi, Fernando Viñuela, Ivan Sepetka, and Velio Macellari. Electrothrombosis of saccular aneurysms via endovascular approach: part 1: electrochemical basis, technique, and experimental results. *Journal of neurosurgery*, 75(1):1–7, 1991.
- Noelia Grande Gutiérrez, Kaushik N Shankar, Talid Sinno, and Scott L Diamond. Thrombosis and hemodynamics: external and intrathrombus gradients. *Current opinion in biomedical engineering*, 19:100316, 2021.
- Noelia Grande Gutierrez, Debanjan Mukherjee, and David Bark Jr. Decoding thrombosis through code: a review of computational models. *Journal of Thrombosis and Haemostasis*, 2023.
- Tarek Haddad, Adam Himes, Laura Thompson, Telba Irony, Rajesh Nair, MDIC Computer Modeling, and Simulation Working Group Participants. Incorporation of

-
- stochastic engineering models as prior information in bayesian medical device trials. *Journal of biopharmaceutical statistics*, 27(6):1089–1103, 2017.
- SE Harrison, SM Smith, J Bernsdorf, DR Hose, and PV Lawford. Application and validation of the lattice boltzmann method for modelling flow-related clotting. *Journal of biomechanics*, 40(13):3023–3028, 2007.
- James J Hathcock. Flow effects on coagulation and thrombosis. *Arteriosclerosis, thrombosis, and vascular biology*, 26(8):1729–1737, 2006.
- QiZhi He and Alexandre M Tartakovsky. Physics-informed neural network method for forward and backward advection-dispersion equations. *Water Resources Research*, 57(7):e2020WR029479, 2021.
- Coenraad H Hemker, Peter LA Giesen, Manoj Ramjee, Rob Wagenvoord, and Suzette Béguin. The thrombogram: monitoring thrombin generation in platelet rich plasma. *Thrombosis and haemostasis*, 83(04):589–591, 2000.
- H Coenraad Hemker and R Kremers. Data management in thrombin generation. *Thrombosis research*, 131(1):3–11, 2013.
- HC Hemker, P Giesen, R AlDieri, V Regnault, E De Smed, R Wagenvoord, T Lecompte, and S Béguin. The calibrated automated thrombogram (cat): a universal routine test for hyper-and hypocoagulability. *Pathophysiology of haemostasis and thrombosis*, 32(5-6):249–253, 2002.
- Matthew F Hockin, Kenneth C Jones, Stephen J Everse, and Kenneth G Mann. A model for the stoichiometric regulation of blood coagulation. *Journal of Biological Chemistry*, 277(21):18322–18333, 2002.
- Jeannette W Hop, Gabriël JE Rinkel, Ale Algra, and Jan van Gijn. Case-fatality rates and functional outcome after subarachnoid hemorrhage: a systematic review. *Stroke*, 28(3):660–664, 1997.
- Kun Hou, Guichen Li, Xianli Lv, Baofeng Xu, Kan Xu, and Jinlu Yu. Delayed rupture of intracranial aneurysms after placement of intra-luminal flow diverter. *The Neuroradiology Journal*, 33(6):451–464, 2020.

REFERENCES

- Johnson Huang and James M Van Gelder. The probability of sudden death from rupture of intracranial aneurysms: a meta-analysis. *Neurosurgery*, 51(5):1101–1107, 2002.
- JD Humphrey and CA Taylor. Intracranial and abdominal aortic aneurysms: similarities, differences, and need for a new class of computational models. *Annual review of biomedical engineering*, 10:221, 2008.
- Jimison Iavindrasana, Luigi Lo Iacono, Henning Müller, Ivan Periz, Paul Summers, Jessica Wright, Christoph M Friedrich, Holger Dach, Tobias Gattermayer, Gerhard Engelbrecht, et al. The@ neurist project. *Studies in health technology and informatics*, 138:161–164, 2008.
- Daniel M Jacobson and Jonathan D Trobe. The emerging role of magnetic resonance angiography in the management of patients with third cranial nerve palsy. *American journal of ophthalmology*, 128(1):94–96, 1999.
- Mahesh V Jayaraman, William W Mayo-Smith, Glenn A Tung, Richard A Haas, Jeffrey M Rogg, Neerav R Mehta, and Curtis E Doberstein. Detection of intracranial aneurysms: multi-detector row ct angiography compared with dsa. *Radiology*, 230(2):510–518, 2004.
- MD Joshi, CJ O’Kelly, T Krings, D Fiorella, and TR Marotta. Observer variability of an angiographic grading scale used for the assessment of intracranial aneurysms treated with flow-diverting stents. *American Journal of Neuroradiology*, 34(8):1589–1592, 2013.
- David F Kallmes, R Hanel, D Lopes, E Boccardi, Alain Bonafé, S Cekirge, D Fiorella, P Jabbour, E Levy, C McDougall, et al. International retrospective study of the pipeline embolization device: a multicenter aneurysm treatment study. *American Journal of Neuroradiology*, 36(1):108–115, 2015.
- Alexander Keedy. An overview of intracranial aneurysms. *McGill Journal of Medicine: MJM*, 9(2):141, 2006.
- Diederik P Kingma and Jimmy Ba. Adam: A method for stochastic optimization. *arXiv preprint arXiv:1412.6980*, 2014.

- Rachel Kleinloog, Nikki De Mul, Bon H Verweij, Jan Andries Post, Gabriel JE Rinkel, and Ynte M Ruigrok. Risk factors for intracranial aneurysm rupture: a systematic review. *Neurosurgery*, 82(4):431–440, 2018.
- Miikka Korja, Riku Kivisaari, Behnam Rezaei Jahromi, and Hanna Lehto. Size and location of ruptured intracranial aneurysms: consecutive series of 1993 hospital-admitted patients. *Journal of neurosurgery*, 127(4):748–753, 2016.
- Yukunori Korogi, Mutsumasa Takahashi, Kazuhiro Katada, Yuko Ogura, Kanehiro Hasuo, Makoto Ochi, Hidetsuna Utsunomiya, Toshi Abe, and Satoshi Imakita. Intracranial aneurysms: detection with three-dimensional ct angiography with volume rendering—comparison with conventional angiographic and surgical findings. *Radiology*, 211(2):497–506, 1999.
- Satu Kotikoski, Jukka Huttunen, Terhi J Huttunen, Katariina Helin, Juhana Frösen, Timo Koivisto, Mitja I Kurki, Mikael von und zu Fraunberg, Ilkka Kunnamo, Juha E Jääskeläinen, et al. Secondary hypertension in patients with saccular intracranial aneurysm disease: a population based study. *PLoS One*, 13(10):e0206432, 2018.
- Andrew L Kuharsky and Aaron L Fogelson. Surface-mediated control of blood coagulation: the role of binding site densities and platelet deposition. *Biophysical journal*, 80(3):1050–1074, 2001.
- Zsolt Kulcsár and István Szikora. The esmint retrospective analysis of delayed aneurysm ruptures after flow diversion (radar) study. *EJMINT*, 2012:1244000088, 2012.
- Ignacio Larrabide, Pedro Omedas, Yves Martelli, Xavier Planes, Maarten Nieber, Juan A Moya, Constantine Butakoff, Rafael Sebastián, Oscar Camara, Mathieu De Craene, et al. Gimias: an open source framework for efficient development of research tools and clinical prototypes. In *Functional Imaging and Modeling of the Heart: 5th International Conference, FIMH 2009, Nice, France, June 3-5, 2009. Proceedings 5*, pages 417–426. Springer, 2009.
- Ignacio Larrabide, Minsuok Kim, Luca Augsburger, Maria Cruz Villa-Uriol, Daniel Rüfenacht, and Alejandro F Frangi. Fast virtual deployment of self-expandable stents: method and in vitro evaluation for intracranial aneurysmal stenting. *Medical image analysis*, 16(3):721–730, 2012.

-
- Pierre Lasjaunias, Siddharta Wuppalapati, Hortensia Alvarez, Georges Rodesch, and Augustin Ozanne. Intracranial aneurysms in children aged under 15 years: review of 59 consecutive children with 75 aneurysms. *Child's Nervous System*, 21(6):437–450, 2005.
- Toni Lassila, Ali Sarrami-Foroushani, SeyedMostafa Hejazi, and Alejandro F Frangi. Population-specific modelling of between/within-subject flow variability in the carotid arteries of the elderly. *International journal for numerical methods in biomedical engineering*, 36(1):e3271, 2020.
- Michael T Lawton, Alfredo Quiñones-Hinojosa, Edward F Chang, and Timothy Yu. Thrombotic intracranial aneurysms: classification scheme and management strategies in 68 patients. *Neurosurgery*, 56(3):441–454, 2005.
- EL Leemans, BMW Cornelissen, G Rosalini, D Verbaan, JJ Schneiders, R van den Berg, WP Vandertop, ET van Bavel, CH Slump, CBLM Majoie, et al. Impact of intracranial aneurysm morphology and rupture status on the particle residence time. *Journal of Neuroimaging*, 29(4):487–492, 2019.
- Karin Leiderman and Aaron L Fogelson. Grow with the flow: a spatial–temporal model of platelet deposition and blood coagulation under flow. *Mathematical medicine and biology: a journal of the IMA*, 28(1):47–84, 2011.
- Karin M Leiderman, Laura A Miller, and Aaron L Fogelson. The effects of spatial inhomogeneities on flow through the endothelial surface layer. *Journal of theoretical biology*, 252(2):313–325, 2008.
- Octave Levenspiel. *Chemical reaction engineering*. John wiley & sons, 1998.
- Jiantao Liang, Yuhai Bao, Hongqi Zhang, Karsten Henning Wrede, Xinglong Zhi, Meng Li, and Feng Ling. The clinical features and treatment of pediatric intracranial aneurysm. *Child's Nervous System*, 25(3):317–324, 2009.
- Fengming Lin, Yan Xia, Shuang Song, Nishant Ravikumar, and Alejandro F Frangi. High-throughput 3dra segmentation of brain vasculature and aneurysms using deep learning. *Computer Methods and Programs in Biomedicine*, 230:107355, 2023.

- Vyacheslav A Lipatov, Aleksey A Kryukov, Dmitry A Severinov, and Araik R Saakyan. Ethical and legal aspects of in vivo experimental biomedical research. *IP Pavlov Russian Medical Biological Herald*, 27(1):80–92, 2019.
- Qiong-Yao Liu, Xiao-Ying Tang, Duan-Duan Chen, Yuan-Qing Xu, and Fang-Bao Tian. Hydrodynamic study of sperm swimming near a wall based on the immersed boundary-lattice boltzmann method. *Engineering Applications of Computational Fluid Mechanics*, 14(1):853–870, 2020.
- Qiongyao Liu, Ali Sarrami-Foroushani, Yongxing Wang, Michael MacRaid, Christopher Kelly, Fengming Lin, Yan Xia, Shuang Song, Nishant Ravikumar, Tufail Patankar, et al. Hemodynamics of thrombus formation in intracranial aneurysms: an in-silico observational study. *APL Bioengineering*, 2023.
- Paweł Maczuga and Maciej Paszyński. Influence of activation functions on the convergence of physics-informed neural networks for 1d wave equation. In *International Conference on Computational Science*, pages 74–88. Springer, 2023.
- Greg Mader, Mette Olufsen, and Adam Mahdi. Modeling cerebral blood flow velocity during orthostatic stress. *Annals of biomedical engineering*, 43(8):1748–1758, 2015.
- Orestis Malaspinas, Alexis Turjman, D Ribeiro de Sousa, Guillermo Garcia-Cardena, Martine Raes, P-TT Nguyen, Yue Zhang, Guy Courbebaisse, Christophe Lelubre, K Zouaoui Boudjeltia, et al. A spatio-temporal model for spontaneous thrombus formation in cerebral aneurysms. *Journal of theoretical biology*, 394:68–76, 2016.
- Kenneth Mann, Stephen Everse, Matthew Hockin, and Kenneth Jones. Blood clotting predictor, January 19 2006. US Patent App. 10/507,661.
- Laurel MM Marsh, Michael C Barbour, Venkat Keshav Chivukula, Fanette Chassagne, Cory M Kelly, Samuel H Levy, Louis J Kim, Michael R Levitt, and Alberto Aliseda. Platelet dynamics and hemodynamics of cerebral aneurysms treated with flow-diverting stents. *Annals of biomedical engineering*, 48:490–501, 2020.
- Justin R Mascitelli, Henry Moyle, Eric K Oermann, Maritsa F Polykarpou, Aanand A Patel, Amish H Doshi, Yakov Gologorsky, Joshua B Bederson, and Aman B Patel. An update to the raymond–roy occlusion classification of intracranial aneurysms treated with coil embolization. *Journal of neurointerventional surgery*, 7(7):496–502, 2015.

-
- Revanth Matthey and Susanta Ghosh. A novel sequential method to train physics informed neural networks for allen cahn and cahn hilliard equations. *Computer Methods in Applied Mechanics and Engineering*, 390:114474, 2022.
- H Meng, VM Tutino, J Xiang, and A Siddiqui. High wss or low wss? complex interactions of hemodynamics with intracranial aneurysm initiation, growth, and rupture: toward a unifying hypothesis. *American Journal of Neuroradiology*, 35(7):1254–1262, 2014.
- Claudia Menichini and Xiao Yun Xu. Mathematical modeling of thrombus formation in idealized models of aortic dissection: initial findings and potential applications. *Journal of mathematical biology*, 73(5):1205–1226, 2016.
- Nipa A Mody and Michael R King. Platelet adhesive dynamics. part i: characterization of platelet hydrodynamic collisions and wall effects. *Biophysical journal*, 95(5):2539–2555, 2008.
- Andrew Molyneux, Richard Kerr, International Subarachnoid Aneurysm Trial (ISAT) Collaborative Group, et al. International subarachnoid aneurysm trial (isat) of neurosurgical clipping versus endovascular coiling in 2143 patients with ruptured intracranial aneurysms: a randomized trial. *Journal of stroke and cerebrovascular diseases*, 11(6):304–314, 2002.
- Hernán G Morales, Minsuok Kim, María-Cruz Villa-Uriol, Elio V Diaz, and Alejandro F Frangi. Influence of coil packing rate and configuration on intracranial aneurysm hemodynamics. In *World Congress on Medical Physics and Biomedical Engineering, September 7-12, 2009, Munich, Germany: Vol. 25/4 Image Processing, Biosignal Processing, Modelling and Simulation, Biomechanics*, pages 2291–2294. Springer, 2010.
- Hernán G Morales, Minsuok Kim, EE Vivas, M-C Villa-Uriol, Ignacio Larrabide, T Sola, Leopoldo Guimaraens, and AF Frangi. How do coil configuration and packing density influence intra-aneurysmal hemodynamics? *American Journal of Neuroradiology*, 32(10):1935–1941, 2011a.
- Hernán G Morales, Ignacio Larrabide, Maria-Cruz Villa-Uriol, Adrianus J Geers, and Alejandro F Frangi. Towards the validation of a virtual coiling technique using a real

- versus a simulated bolus injection. In *Proceedings of the 2nd International Conference on Mathematical and Computational Biomedical Engineering (CMBEâ€™11)*, pages 512–515, 2011b.
- Hernán G Morales, Ignacio Larrabide, Arjan J Geers, Martha L Aguilar, and Alejandro F Frangi. Newtonian and non-newtonian blood flow in coiled cerebral aneurysms. *Journal of biomechanics*, 46(13):2158–2164, 2013.
- Max D Morris. Factorial sampling plans for preliminary computational experiments. *Technometrics*, 33(2):161–174, 1991.
- Philipp Moser, Wolfgang Fenz, Stefan Thumfart, Isabell Ganitzer, and Michael Giretzlehner. Modeling of 3d blood flows with physics-informed neural networks: comparison of network architectures. *Fluids*, 8(2):46, 2023.
- Katharina Neubauer and Barbara Zieger. Endothelial cells and coagulation. *Cell and tissue research*, 387(3):391–398, 2022.
- Malebogo N Ngoepe, Alejandro F Frangi, James V Byrne, and Yiannis Ventikos. Thrombosis in cerebral aneurysms and the computational modeling thereof: a review. *Frontiers in physiology*, 9:306, 2018.
- MN Ngoepe and Y Ventikos. Computational modelling of clot development in patient-specific cerebral aneurysm cases. *Journal of Thrombosis and Haemostasis*, 14(2):262–272, 2016.
- Ville Nurminen, Martin Lehecka, Amit Chakrabarty, Riku Kivisaari, Hanna Lehto, Mika Niemelä, and Juha Hernesniemi. Anatomy and morphology of giant aneurysmsâ€™”angiographic study of 125 consecutive cases. *Acta neurochirurgica*, 156(1):1–10, 2014.
- E Nyilas, WA Morton, DM Lederman, TH Chiu, and RD Cumming. Interdependence of hemodynamic and surface parameters in thrombosis. *ASAIO Journal*, 21(1):55–70, 1975.
- Shigehiko Ogoh, Paul J Fadel, Rong Zhang, Christian Selmer, Øivind Jans, Niels H Secher, and Peter B Raven. Middle cerebral artery flow velocity and pulse pressure during dynamic exercise in humans. *American Journal of Physiology-Heart and Circulatory Physiology*, 288(4):H1526–H1531, 2005.

-
- H Ohta, N Sakai, I Nagata, H Sakai, A Shindo, and H Kikuchi. Spontaneous total thrombosis of distal superior cerebellar artery aneurysm. *Acta neurochirurgica*, 143(8):837–843, 2001.
- CJ O’kelly, T Krings, D Fiorella, and TR Marotta. A novel grading scale for the angiographic assessment of intracranial aneurysms treated using flow diverting stents. *Interventional Neuroradiology*, 16(2):133–137, 2010.
- Chubin Ou, Wei Huang, and Matthew Ming-Fai Yuen. A computational model based on fibrin accumulation for the prediction of stasis thrombosis following flow-diverting treatment in cerebral aneurysms. *Medical & biological engineering & computing*, 55(1):89–99, 2017.
- Rafik Ouared, Bastien Chopard, Bernd Stahl, Daniel A Rüfenacht, Hasan Yilmaz, and Guy Courbebaisse. Thrombosis modeling in intracranial aneurysms: a lattice boltzmann numerical algorithm. *Computer Physics Communications*, 179(1-3):128–131, 2008.
- Rafik Ouared, Ignacio Larrabide, Olivier Brina, Pierre Bouillot, Gorislav Erceg, Hasan Yilmaz, Karl-Olof Lovblad, and Vitor Mendes Pereira. Computational fluid dynamics analysis of flow reduction induced by flow-diverting stents in intracranial aneurysms: a patient-unspecific hemodynamics change perspective. *Journal of neurointerventional surgery*, 8(12):1288–1293, 2016.
- Francesco Pappalardo, Giulia Russo, Flora Musuamba Tshinanu, and Marco Viceconti. In silico clinical trials: concepts and early adoptions. *Briefings in bioinformatics*, 20(5):1699–1708, 2019.
- T Phillips, P Mitchell, R Dowling, B Yan, et al. Endovascular treatment of intracranial aneurysms with new generation flow diverting stents. early experience in an australian centre. European Congress of Radiology-RANZCR ASM 2010, 2010.
- Marina Piccinelli, David A Steinman, Yiemeng Hoi, Frank Tong, Alessandro Veneziani, and Luca Antiga. Automatic neck plane detection and 3d geometric characterization of aneurysmal sacs. *Annals of biomedical engineering*, 40:2188–2211, 2012.
- L Pierot, T Liebig, V Sychra, K Kadziolka, F Dorn, C Strasilla, C Kabbasch, and J Klisch. Intrasaccular flow-disruption treatment of intracranial aneurysms: prelim-

-
- inary results of a multicenter clinical study. *American journal of neuroradiology*, 33(7):1232–1238, 2012.
- Laurent Pierot and Alessandra Biondi. Endovascular techniques for the management of wide-neck intracranial bifurcation aneurysms: a critical review of the literature. *Journal of Neuroradiology*, 43(3):167–175, 2016.
- Laurent Pierot and Ajay K Wakhloo. Endovascular treatment of intracranial aneurysms: current status. *Stroke*, 44(7):2046–2054, 2013.
- Jeremy E Purvis, Manash S Chatterjee, Lawrence F Brass, and Scott L Diamond. A molecular signaling model of platelet phosphoinositide and calcium regulation during homeostasis and p2y1 activation. *Blood, The Journal of the American Society of Hematology*, 112(10):4069–4079, 2008.
- Qin M Qi and Eric SG Shaqfeh. Time-dependent particle migration and margination in the pressure-driven channel flow of blood. *Physical Review Fluids*, 3(3):034302, 2018.
- Ansaar T Rai, Jeffery P Hogg, Brendan Cline, and Gerald Hobbs. Cerebrovascular geometry in the anterior circulation: an analysis of diameter, length and the vessel taper. *Journal of neurointerventional surgery*, 5(4):371–375, 2013.
- Maziar Raissi, Paris Perdikaris, and George E Karniadakis. Physics-informed neural networks: A deep learning framework for solving forward and inverse problems involving nonlinear partial differential equations. *Journal of Computational Physics*, 378:686–707, 2019.
- JV Ramana Reddy and D Srikanth. Impact of blood vessel wall flexibility on the temperature and concentration dispersion. *Journal of Applied and Computational Mechanics*, 6(3):564–581, 2020.
- KKD Ramesh, G Kiran Kumar, K Swapna, Debabrata Datta, and S Suman Rajest. A review of medical image segmentation algorithms. *EAI Endorsed Transactions on Pervasive Health and Technology*, 7(27):e6–e6, 2021.
- Vitaliy L Rayz and Aaron A Cohen-Gadol. Hemodynamics of cerebral aneurysms: connecting medical imaging and biomechanical analysis. *Annual review of biomedical engineering*, 22:231–256, 2020.

-
- VL Rayz, L Boussel, MT Lawton, G Acevedo-Bolton, L Ge, WL Young, RT Higashida, and D Saloner. Numerical modeling of the flow in intracranial aneurysms: prediction of regions prone to thrombus formation. *Annals of biomedical engineering*, 36(11):1793, 2008.
- VL Rayz, L Boussel, L Ge, JR Leach, AJ Martin, MT Lawton, C McCulloch, and D Saloner. Flow residence time and regions of intraluminal thrombus deposition in intracranial aneurysms. *Annals of biomedical engineering*, 38(10):3058–3069, 2010.
- Yuan Ren, Guo-Zhong Chen, Zhen Liu, Yan Cai, Guang-Ming Lu, and Zhi-Yong Li. Reproducibility of image-based computational models of intracranial aneurysm: a comparison between 3d rotational angiography, ct angiography and mr angiography. *Biomedical engineering online*, 15:1–14, 2016.
- Marissa Renardy, Louis R Joslyn, Jess A Millar, and Denise E Kirschner. To sobol or not to sobol? the effects of sampling schemes in systems biology applications. *Mathematical biosciences*, 337:108593, 2021.
- Mirza Md Symon Reza and Amirhossein Arzani. A critical comparison of different residence time measures in aneurysms. *Journal of biomechanics*, 88:122–129, 2019.
- Gabriel JE Rinkel, Mamuka Djibuti, Ale Algra, and J Van Gijn. Prevalence and risk of rupture of intracranial aneurysms: a systematic review. *Stroke*, 29(1):251–256, 1998.
- Rebecca A Risman, Nicholas C Kirby, Brittany E Bannish, Nathan E Hudson, and Valerie Tutwiler. Fibrinolysis: an illustrated review. *Research and practice in thrombosis and haemostasis*, 7(2):100081, 2023.
- Anil K Roy, Jonathan A Grossberg, Joshua W Osbun, Susana L Skukalek, Brian M Howard, Faiz U Ahmad, Frank Tong, Jacques E Dion, and Charles M Cawley. Carotid cavernous fistula after pipeline placement: a single-center experience and review of the literature. *Journal of NeuroInterventional Surgery*, 9(2):152–158, 2017.
- Daniel Roy, Geneviève Milot, and Jean Raymond. Endovascular treatment of unruptured aneurysms. *Stroke*, 32(9):1998–2004, 2001.
- Isil Saatci, H Saruhan Cekirge, Elisa FM Ciceri, Michel E Mawad, A Gulsun Pamuk, and Aytekin Besim. Ct and mr imaging findings and their implications in the follow-

- up of patients with intracranial aneurysms treated with endosaccular occlusion with onyx. *American journal of neuroradiology*, 24(4):567–578, 2003.
- Anna MH Sailer, Bart AJM Wagemans, Patricia J Nelemans, Rick de Graaf, and Willem H van Zwam. Diagnosing intracranial aneurysms with mr angiography: systematic review and meta-analysis. *Stroke*, 45(1):119–126, 2014.
- A Saltelli. *Global Sensitivity Analysis: the Primer*. John Wiley & Sons, 2008.
- Andrea Saltelli, Marco Ratto, Stefano Tarantola, and Francesca Campolongo. Sensitivity analysis for chemical models. *Chemical reviews*, 105(7):2811–2828, 2005.
- Ali Sarrami-Foroushani, Toni Lassila, Ali Gooya, Arjan J Geers, and Alejandro F Frangi. Uncertainty quantification of wall shear stress in intracranial aneurysms using a data-driven statistical model of systemic blood flow variability. *Journal of biomechanics*, 49(16):3815–3823, 2016.
- Ali Sarrami-Foroushani, Toni Lassila, and Alejandro F Frangi. Virtual endovascular treatment of intracranial aneurysms: models and uncertainty. *Wiley Interdisciplinary Reviews: Systems Biology and Medicine*, 9(4):e1385, 2017.
- Ali Sarrami-Foroushani, Toni Lassila, Seyed Mostafa Hejazi, Sanjoy Nagaraja, Andrew Bacon, and Alejandro F Frangi. A computational model for prediction of clot platelet content in flow-diverted intracranial aneurysms. *Journal of biomechanics*, 91:7–13, 2019.
- Ali Sarrami-Foroushani, Toni Lassila, Michael MacRaid, Joshua Asquith, Kit CB Roes, James V Byrne, and Alejandro F Frangi. In-silico trial of intracranial flow diverters replicates and expands insights from conventional clinical trials. *Nature Communications*, 12(1):1–12, 2021.
- Alba Scerrati, Giovanni Sabatino, Giuseppe Maria Della Pepa, Alessio Albanese, Enrico Marchese, Alfredo Puca, Alessandro Olivi, and Carmelo Lucio Sturiale. Treatment and outcome of thrombosed aneurysms of the middle cerebral artery: institutional experience and a systematic review. *Neurosurgical review*, 42(3):649–661, 2019.
- O Schubiger, A Valavanis, and J Hayek. Computed tomography in cerebral aneurysms with special emphasis on giant intracranial aneurysms. *Journal of computer assisted tomography*, 4(1):24–32, 1980.

-
- Yuka Sen, Yi Qian, Alberto Avolio, and Michael Morgan. Image segmentation methods for intracranial aneurysm haemodynamic research. *Journal of Biomechanics*, 47(5): 1014–1019, 2014.
- Larissa Shamseer, David Moher, Mike Clarke, Davina Ghera, and Alessandro Liberati. Research methods & reporting. *BMJ*, pages 1–25, 2015.
- Vincent Sitzmann, Julien Martel, Alexander Bergman, David Lindell, and Gordon Wetstein. Implicit neural representations with periodic activation functions. *Advances in neural information processing systems*, 33:7462–7473, 2020.
- Tyler Skorczewski, Lindsay Crowl Erickson, and Aaron L Fogelson. Platelet motion near a vessel wall or thrombus surface in two-dimensional whole blood simulations. *Biophysical journal*, 104(8):1764–1772, 2013.
- Stephanie A Smith, Richard J Travers, and James H Morrissey. How it all starts: Initiation of the clotting cascade. *Critical reviews in biochemistry and molecular biology*, 50(4):326–336, 2015.
- Erik N Sorensen, Greg W Burgreen, William R Wagner, and James F Antaki. Computational simulation of platelet deposition and activation: I. model development and properties. *Annals of biomedical engineering*, 27:436–448, 1999.
- David A Steinman. Image-based computational fluid dynamics modeling in realistic arterial geometries. *Annals of biomedical engineering*, 30:483–497, 2002.
- David A Steinman and Vitor M Pereira. How patient specific are patient-specific computational models of cerebral aneurysms? an overview of sources of error and variability. *Neurosurgical focus*, 47(1):E14, 2019.
- Francesca Storti and FN Van De Vosse. A continuum model for platelet plug formation, growth and deformation. *International journal for numerical methods in biomedical engineering*, 30(12):1541–1557, 2014.
- Charles M Strother, Petter Eldevik, Yoichi Kikuchi, Virgil Graves, Curtis Partington, and Anthony Merlis. Thrombus formation and structure and the evolution of mass effect in intracranial aneurysms treated by balloon embolization: emphasis on mr findings. *American journal of neuroradiology*, 10(4):787–796, 1989.

-
- Charles A Taylor and CA Figueroa. Patient-specific modeling of cardiovascular mechanics. *Annual review of biomedical engineering*, 11:109–134, 2009.
- Joshua O Taylor, Richard S Meyer, Steven Deutsch, and Keefe B Manning. Development of a computational model for macroscopic predictions of device-induced thrombosis. *Biomechanics and modeling in mechanobiology*, 15:1713–1731, 2016.
- B Gregory Thompson, Robert D Brown Jr, Sepideh Amin-Hanjani, Joseph P Broderick, Kevin M Cockcroft, E Sander Connolly Jr, Gary R Duckwiler, Catherine C Harris, Virginia J Howard, S Claiborne Johnston, et al. Guidelines for the management of patients with unruptured intracranial aneurysms: a guideline for healthcare professionals from the american heart association/american stroke association. *Stroke*, 46(8):2368–2400, 2015.
- Bernd Turowski, Stephan Macht, Zolt Kulcsár, Daniel Hänggi, and Walter Stummer. Early fatal hemorrhage after endovascular cerebral aneurysm treatment with a flow diverter (silk-stent). *Neuroradiology*, 53(1):37–41, 2011.
- Shashank Reddy Vadyala, Sai Nethra Betgeri, and Naga Parameshwari Betgeri. Physics-informed neural network method for solving one-dimensional advection equation using pytorch. *Array*, 13:100110, 2022.
- Koohyar Vahidkhah, Scott L Diamond, and Prosenjit Bagchi. Platelet dynamics in three-dimensional simulation of whole blood. *Biophysical journal*, 106(11):2529–2540, 2014.
- Kristian Valen-Sendstad, Aslak W Bergersen, Yuji Shimogonya, Leonid Goubergrits, Jan Bruening, Jordi Pallares, Salvatore Cito, Senol Piskin, Kerem Pekkan, Arjan J Geers, et al. Real-world variability in the prediction of intracranial aneurysm wall shear stress: the 2015 international aneurysm cfd challenge. *Cardiovascular engineering and technology*, 9:544–564, 2018.
- JaGJR van Gijn and GJE Rinkel. Subarachnoid haemorrhage: diagnosis, causes and management. *Brain*, 124(2):249–278, 2001.
- Willem Jan van Rooij, ME Sprengers, Anjob N de Gast, JPP Peluso, and Menno Sluzewski. 3d rotational angiography: the new gold standard in the detection of

- additional intracranial aneurysms. *American Journal of Neuroradiology*, 29(5):976–979, 2008.
- Marco Viceconti, Adriano Henney, and Edwin Morley-Fletcher. In silico clinical trials: how computer simulation will transform the biomedical industry. *International Journal of Clinical Trials*, 3(2):37–46, 2016.
- Marco Viceconti, Miguel A Juárez, Cristina Curreli, Marzio Pennisi, Giulia Russo, and Francesco Pappalardo. Credibility of in silico trial technologies—a theoretical framing. *IEEE journal of biomedical and health informatics*, 24(1):4–13, 2019.
- Marco Viceconti, Francesco Pappalardo, Blanca Rodriguez, Marc Horner, Jeff Bischoff, and Flora Musuamba Tshinanu. In silico trials: Verification, validation and uncertainty quantification of predictive models used in the regulatory evaluation of biomedical products. *Methods*, 185:120–127, 2021.
- MC Villa-Uriol, G Berti, DR Hose, A Marzo, A Chiarini, J Penrose, J Pozo, JG Schmidt, P Singh, R Lycett, et al. @neurist complex information processing toolchain for the integrated management of cerebral aneurysms. *Interface Focus*, 1(3):308–319, 2011.
- Monique HM Vlak, Gabriel JE Rinkel, Paut Greebe, and Ale Algra. Independent risk factors for intracranial aneurysms and their joint effect: a case-control study. *Stroke*, 44(4):984–987, 2013.
- R Wagenvoord, PW Hemker, and HC Hemker. The limits of simulation of the clotting system. *Journal of thrombosis and haemostasis*, 4(6):1331–1338, 2006.
- Sifan Wang, Hanwen Wang, and Paris Perdikaris. On the eigenvector bias of fourier feature networks: From regression to solving multi-scale pdes with physics-informed neural networks. *Computer Methods in Applied Mechanics and Engineering*, 384:113938, 2021.
- Sifan Wang, Shyam Sankaran, Hanwen Wang, and Paris Perdikaris. An expert’s guide to training physics-informed neural networks. *arXiv preprint arXiv:2308.08468*, 2023.
- Gerhard Wanner and Ernst Hairer. *Solving ordinary differential equations II*, volume 375. Springer Berlin Heidelberg New York, 1996.

REFERENCES

- Jeffrey I Weitz and JC Fredenburgh. Overview of hemostasis and thrombosis. *R. Hoffman [et al.] Hematology, Basic Principles and Practice*, pages 1774–1783, 2013.
- IR Whittle, NICHOLAS W Dorsch, and MICHAEL Besser. Spontaneous thrombosis in giant intracranial aneurysms. *Journal of Neurology, Neurosurgery & Psychiatry*, 45(11):1040–1047, 1982.
- Kathleen Withers, Grace Carolan-Rees, and Megan Dale. Pipeline embolization device for the treatment of complex intracranial aneurysms. *Applied health economics and health policy*, 11(1):5–13, 2013.
- Michael J Workman, Harry J Cloft, Frank C Tong, Jacques E Dion, Mary E Jensen, William F Marx, and David F Kallmes. Thrombus formation at the neck of cerebral aneurysms during treatment with Guglielmi detachable coils. *American Journal of Neuroradiology*, 23(9):1568–1576, 2002.
- Adam R Wufsus, NE Macera, and KB Neeves. The hydraulic permeability of blood clots as a function of fibrin and platelet density. *Biophysical journal*, 104(8):1812–1823, 2013.
- J Xiang, AH Siddiqui, and H Meng. The effect of inlet waveforms on computational hemodynamics of patient-specific intracranial aneurysms. *Journal of biomechanics*, 47(16):3882–3890, 2014.
- Jianping Xiang, Markus Tremmel, John Kolega, Elad I Levy, Sabareesh K Natarajan, and Hui Meng. Newtonian viscosity model could overestimate wall shear stress in intracranial aneurysm domes and underestimate rupture risk. *Journal of neurointerventional surgery*, 4(5):351–357, 2012.
- Zhiliang Xu, Nan Chen, Malgorzata M Kamocka, Elliot D Rosen, and Mark Alber. A multiscale model of thrombus development. *Journal of the Royal Society Interface*, 5(24):705–722, 2008.
- Clyde W Yancy, Mariell Jessup, Biykem Bozkurt, Javed Butler, Donald E Casey Jr, Monica M Colvin, Mark H Drazner, Gerasimos S Filippatos, Gregg C Fonarow, Michael M Givertz, et al. 2017 acc/aha/hfsa focused update of the 2013 accf/aha guideline for the management of heart failure: a report of the American College of Cardiology/American Heart Association Task Force on Clinical Practice Guidelines and

- the heart failure society of america. *Journal of the American College of Cardiology*, 70(6):776–803, 2017.
- Liu Yang, Xuhui Meng, and George Em Karniadakis. B-pinns: Bayesian physics-informed neural networks for forward and inverse pde problems with noisy data. *Journal of Computational Physics*, 425:109913, 2021.
- Sumith Yesudasan and Rodney D Averett. Recent advances in computational modeling of fibrin clot formation: A review. *Computational biology and chemistry*, 83:107148, 2019.
- Minglang Yin, Xiaoning Zheng, Jay D Humphrey, and George Em Karniadakis. Non-invasive inference of thrombus material properties with physics-informed neural networks. *arXiv preprint arXiv:2005.11380*, 2020.
- Babak Zamanlooy and Mitra Mirhassani. Efficient vlsi implementation of neural networks with hyperbolic tangent activation function. *IEEE Transactions on Very Large Scale Integration (VLSI) Systems*, 22(1):39–48, 2013.